

THE NUCLEAR SHELL MODEL AS A TESTING GROUND FOR MANY-BODY QUANTUM CHAOS

Vladimir ZELEVINSKY^{a,b,c}, B. Alex BROWN^{a,b}, Njema FRAZIER^{a,b}, Mihai HOROI^{a,d,e}

^a *National Superconducting Cyclotron Laboratory, Michigan State University, East Lansing,
MI 48824-1321, USA*

^b *Department of Physics and Astronomy, Michigan State University, East Lansing, MI 48824-1116, USA*

^c *Budker Institute of Nuclear Physics, Novosibirsk 630090, Russia*

^d *Physics Department, Central Michigan University, Mount Pleasant, MI 48859, USA*

^e *Institute of Atomic Physics, Bucharest, Romania*



ELSEVIER

AMSTERDAM – LAUSANNE – NEW YORK – OXFORD – SHANNON – TOKYO



ELSEVIER

Physics Reports 276 (1996) 85–176

PHYSICS REPORTS

The nuclear shell model as a testing ground for many-body quantum chaos

Vladimir Zelevinsky^{a,b,c}, B. Alex Brown^{a,b}, Njema Frazier^{a,b}, Mihai Horoi^{a,d,e}

^a National Superconducting Cyclotron Laboratory, Michigan State University, East Lansing, MI 48824-1321, USA

^b Department of Physics and Astronomy, Michigan State University, East Lansing, MI 48824-1116, USA

^c Budker Institute of Nuclear Physics, Novosibirsk 630090, Russia

^d Physics Department, Central Michigan University, Mount Pleasant, MI 48859, USA

^e Institute of Atomic Physics, Bucharest, Romania

Received December 1995; editor: G.E. Brown

Contents

1. Introduction	88	4.5. Correlations of eigenvector components	139
2. Shell-model calculations	93	4.6. Do we really measure complexity?	141
2.1. General formulation	93	5. Fragmentation and spreading	142
2.2. Angular momentum and isospin projection	94	5.1. “Standard model” of the spreading width	143
2.3. The model	95	5.2. Spreading width in the stochastic regime	144
2.4. Strength functions and fragmentation widths	96	5.3. Strength functions of basis states	147
2.5. Banded properties of the hamiltonian matrix	103	5.4. Two-step diagonalization and the spreading width	152
2.6. Distribution of matrix elements	106	6. Chaoticity versus thermalization	154
3. Level statistics	108	6.1. Thermal equilibrium in a small closed system?	155
3.1. Level density	109	6.2. Statistical equilibrium and stochastic dynamics	156
3.2. Level spacing distribution	116	6.3. Single-particle occupation numbers	158
3.3. Level repulsion at small spacings	119	6.4. Complexity and thermalization	161
3.4. Spectral rigidity	121	6.5. Discussion	163
3.5. Level dynamics	125	7. Pairing correlations and stochastization	164
4. Complexity of wave functions	128	8. Conclusions	169
4.1. Distribution of components	128	Appendix	171
4.2. Information entropy	129	References	173
4.3. Representation dependence	136	Note added in proof	176
4.4. Other measures of complexity	137		

Abstract

Atomic nuclei analyzed in the framework of the shell model provide a good example of a many-body quantum system with strong interactions between its constituents. As excitation energy and level density increase, the system evolves in the direction of very complicated (“stochastic”) dynamics. Energy levels and stationary wave functions obtained in realistic shell-model calculations are studied from the viewpoint of signatures of quantum chaos and complexity. The standard characteristics of local level statistics, such as nearest level spacing distribution or spectral rigidity, manifest chaoticity which agrees with the GOE predictions. Going beyond that, we analyze the structure of the eigenfunctions and the distribution function of the eigenvector components using basis-dependent quantitative criteria such as information entropy. The degree of complexity is shown to be a smooth function of excitation energy. The representation dependence provides additional physical information on the interrelation between the eigenbasis and the representation basis. The exceptional role of the mean field basis is discussed. The spreading width and the shape of the strength function of the original simple states are also studied. The generic wave functions in the chaotic region have similar observable properties which can be characterized by the average single-particle occupation numbers. Agreement with the Fermi–Dirac distribution manifests the correspondence between chaotic dynamics and thermalization. The information entropy in the mean field basis gives an equivalent temperature scale which confirms this correspondence. Pairing correlations display a phase transition to the normal state with a long tail of fluctuational enhancement above the level expected for a heated Fermi gas.

PACS: 21.10.Ma; 21.10.Pc; 24.60.Lz; 21.60.Cs

Keywords: Quantum chaos; Nuclear shell model; Spreading width; Level statistics; Entropy; Pairing

1. Introduction

Chaotic dynamics is one of the most rapidly developing subjects in physics. Classical deterministic chaos, which originates from the extreme sensitivity of a system to subtle variations of initial conditions or parameters, is well understood [1, 2], especially for a small number of degrees of freedom. In contrast, a rigorous mathematical definition of quantum chaos does not exist. The direct extension of classical results seems to be impossible because of the uncertainty relation, the linearity of the Schrödinger equation and the noncommutativeness of limiting transitions $\hbar \rightarrow 0$ and $t \rightarrow \infty$. Therefore many physicists prefer to discuss quantum signatures [3, 4] or quantum suppression [5] of classical chaos.

The transition to the classical limit is straightforward in problems of the one-body type. Quantum billiards are the best known examples. Classically, regular or chaotic features of motion are determined by the shape of boundaries. Quantum level statistics [6–8] display specific local correlations and fluctuations of Poisson or Wigner type, respectively. This “one-body chaos” was thoroughly studied in experiments with microwave cavities [9, 10]. Recently similar studies were carried out [11] for acoustical chaos in three-dimensional geometry.

In many-body quantum systems a clear semiclassical picture arises, as a rule, only in the mean field approximation. In this case a system is modeled by a gas of quasiparticles in the self-consistent field of a certain shape. Symmetry (or absence of symmetry) of the mean field determines regularity (or chaoticity) of single-particle motion. The diversity of the mean field configurations in atomic nuclei allows one to use nuclei as a good example of regular and chaotic single-particle dynamics. The transition between those extreme cases has been studied for nucleons in a deformed field as a function of perturbations violating the symmetry, see for example [12–14]. Observable consequences of chaotic single-electron spectra were discussed long ago [15] in application to small metallic particles. Mesoscopic objects of solid state physics give another example where the essential features of underlying chaotic dynamics can be understood, mostly from the single-electron point of view [16].

Low-lying states of nuclei also manifest collective excitations. Truncating the nuclear Hilbert space to a small number of collective modes, as in the interacting boson model, one can consider corresponding quasiparticles (phonons) and their interaction in analogy to classical coupled oscillators. Here again chaotic or regular properties can be related to those of the semiclassical limit [17]. The natural generalization leads to chaotic dynamics of the interacting boson–fermion model [18] which can be viewed as one-body chaos for a billiard with vibrating boundaries. To model collective rotational motion, a rotating billiard was studied in [19]. All such models, being quite instructive, are not sufficient for understanding chaotic dynamics in actual many-body systems where the approximation of isolated single-particle or collective degrees of freedom becomes invalid very quickly as the excitation energy increases.

Until now the manifestations of quantum chaos are associated mainly with the specific features of correlations and fluctuations of energy level positions on a microscopic scale. In nuclear spectra, the empirical analysis of level statistics started more than half a century ago [20]. The conjecture [8] of correspondence between the level spacing distribution and other local features of the sequences of levels, on one hand, and chaotic dynamics, on the other hand, is supported [6, 7, 21] by the empirical statistics of neutron and proton resonances. In the semiclassical limit this conjecture was in fact proven [22]. The nearest level spacing distribution $P(s)$ is expected to

manifest a transition from regular (Poisson) to chaotic (Wigner) dynamics, the latter being in agreement with the random matrix predictions [6, 7, 21] of the Gaussian Orthogonal Ensemble (GOE) which is used for systems invariant under time reversal. Without this symmetry, the generic random matrix ensemble would be the Gaussian Unitary Ensemble (GUE) with stronger (quadratic) level repulsion at small spacings. The analysis [23] of data based on this difference allowed French and collaborators to put the upper limit of 0.1% on the admixture of time-reversal noninvariant forces.

The statistics of the low-lying nuclear levels in the cases where complete spectroscopic information is available [24, 25] show that the transition to the Wigner distribution occurs at excitation energy as low as about 4 MeV. Model microscopic calculations [26] demonstrate that in the mixing of simple one particle–one hole (1p–1h) configurations it is sufficient to take into account the nearest exciton class (2p–2h) to obtain the chaotic function $P(s)$. Similar conclusions follow from data on high spin levels above the yrast-line [27]. Unfortunately, in all practical cases, the experimental data are too scarce to make a quantitative analysis of the transition between regular and chaotic dynamics feasible.

The new features which distinguish the complicated dynamics in many-body systems from the billiard-type problems are associated with the residual interactions of quasiparticles. As the excitation energy and level density increase, the residual interactions become more and more important. The number of excited quasiparticles is also growing and the mean field “billiard” is getting overcrowded. Incoherent collision-like processes as well as anharmonicity of collective modes make the lifetime of elementary excitations short. The actual stationary states become exceedingly complicated superpositions of original “simple” configurations. We will call this process “stochastization”.

As a result of the increasing level density and the stochastization of the stationary wave functions, even small components of the residual interaction can lead to observable consequences. The most spectacular example can be found in the so-called “dynamic” (more precisely, statistical) enhancement of weak interactions [28, 29]. At the same time the local level statistics display typical features of chaos. This pattern of chaotic signatures mixed with the apparent failure of the independent quasiparticle model can be called “many-body chaos” [30]. In many respects this is nothing but Niels Bohr’s compound nucleus [31]. However at this stage we are interested in internal properties of a quantal system with a discrete spectrum rather than in reaction cross-sections. The influence of the continuum on the intrinsic states is assumed to be negligible. Chaotic dynamics in an open system is a very interesting and almost unexplored field [32, 30].

The transition from elementary modes to quantum chaos is of course not specific for nuclei. In spin–fermion systems modeling high-temperature superconductivity, the transitional region seems to be abnormally narrow [33]. As known for a long time, atomic spectra manifest [34] the same universal level statistics. Recently the detailed analysis of compound states in a heavy atom was performed in [35] essentially along the same lines as we pursue in this paper.

While local correlations and fluctuations of levels are considered to be understood, much less is known on structure and correlations of stationary wave functions and matrix elements in the intermediate and chaotic domains. Following the arguments by Percival [36], it is usually accepted that generic chaotic wave functions all “look the same” covering the entire available configuration space. For a many-body case, the multidimensional configuration space, as a rule, is not convenient

for realistic calculations, especially in the stochastic regime. Instead, one has to work usually with the stationary states in restricted Hilbert space. The empirical information available on the structure of complicated wave functions in realistic systems is rather poor.

In systems with a small number of degrees of freedom, the remnants of regular behavior, “scars”, exist [37, 38]. The analog of scarring in the many-body case supposedly can be found in simple modes of motion which up to a certain extent keep their identity in the stochastic environment. It was shown [39] that giant collective excitations associated with the shape vibrations of the mean field may coexist with chaotic single-particle dynamics. Turning on the residual interaction, one can see the progressive damping of collective modes due to their mixing with incoherent complicated states. Similar to the scars in the coordinate space, the remainder of the collective mode will be the concentration of the collective strength in a certain energy range of Hilbert space.

To perform an analysis of the structure of the eigenvectors which can contain a large amount of significant simple components, one needs a quantifying tool. At this stage one has to select a certain basis in Hilbert space. There is no invariant measure for degree of complexity of wave functions (in the eigenbasis of the hamiltonian the stationary eigenvectors have no complexity at all). Therefore the problem of natural, or preferential, representation arises.

One can argue [40] that such a basis is to be related to the mean field of the many-body system. The mean field naturally emerges [41, 40] from averaging out random collision-like processes. It means that the mean field accumulates the most smooth components of many-body dynamics, providing the best framework for separating global (secular behavior) and local (correlations and fluctuations of individual eigenstates and eigenvalues) properties. The mean field representation allows one to trace in detail the transition from independent quasiparticle motion to complicated compound states. On the other hand, a reasonable measure of complexity is expected to be insensitive to the particular choice of details of the mean field basis provided it is stable with respect to collective modes. In any case, complexity of an eigenfunction in a given representation displays a mutual relationship between the eigenbasis of the hamiltonian and the representation basis, and therefore can provide additional physical information.

In the mean field representation, the stochastization process manifests itself in developing delocalization of the eigenstates in Hilbert space. The number N of significant components of a typical wave function, or its localization length l in the given basis, can be used for qualitative, and sometimes quantitative, evaluation of degree of complexity. In the strong mixing regime (“stochastic limit” [42]), the N -scaling of matrix elements of simple (one- or two-body) operators for transitions related to compound states [28, 29] gives an important guideline to physical estimates. Apart from the above-mentioned statistical enhancement of weak interactions, it was used for the general classification of nuclear reactions proceeding via the compound nucleus [43].

Looking at the complexity of stationary wave functions, one can imagine two opposite situations. In the first case, the degree of complexity of eigenstates at approximately the same excitation energy strongly fluctuates from one state to another revealing the possibility that neighboring states in the region of high level density could have completely unrelated structure. In the second case, neighboring states are of similar degree of complexity which would display smooth energy behavior. In accordance with Percival’s arguments [36], we expect the second option to occur in the region of chaotic dynamics where only exact integrals of motion are kept intact and the wave functions are completely mixed to “look the same”. If this is the case, expectation values of macroscopic observables should not depend on a choice of a specific superposition of generic states

in the narrow energy window. However, this is nothing but the main property of statistical equilibrium. The question of correspondence between the signatures of quantum chaos in a many-body system and thermal equilibrium is of deep physical importance.

As we already pointed out, the regime of stochastic dynamics is not expected to be structureless. The presence of single-particle and collective motion (shape vibrations, rotation and giant resonances in nuclei) associated with simple excitation modes displays the regular mean field component of dynamics persisting in the stochastic region. Of course, those states are highly fragmented and the concept of the localization length of an eigenstate can be translated into the conventional notion of the spreading width [21] of a basis state. Simple arguments related to the idea of stochastic limit show [30, 42, 44] that, in this limit, spreading widths cease to grow as a function of nuclear temperature, being determined by the original residual interaction rather than by the increasing level density. Apparently this is observed experimentally [45] as the saturation of the spreading width of giant dipole resonances excited in hot nuclei. A similar way of reasoning was successfully applied to isobaric analog resonances [46, 47] where surprisingly small variations of the spreading width throughout the periodic table are well known [48].

We mentioned several areas where the idea of stochastic dynamics turned out to be quite productive. However, until now it lacks the essential “empirical” justification based on the analysis of statistically reliable data for wave functions and transition amplitudes in actual many-body systems. Apart from the nearest level spacing distribution, the only direct confirmation comes from the Porter–Thomas distribution of amplitudes connecting compound states to simple channels [6, 7, 21]. In the statistical analysis of complicated states generated by realistic calculations for heavy atoms [35], the authors have found important regularities of the spreading widths and single-particle occupation numbers, although the statistics (about 200 levels) are not very good.

Nuclear shell-model calculations appear to be one of the most promising candidates for theoretically probing the structure of complicated wave functions in quantum many-body systems with strong interactions. Encouraging studies have already been carried out using realistic models [51, 52] and simplified schemes such as the Lipkin model [49, 50].

Our goal in the present paper is to study various aspects of quantum chaos, its interplay with regular features and thermalization, using the realistic shell model as a testing ground. We start (Section 2) with a brief description of the model. The realistic semi-empirical hamiltonian and construction of basis states with exact quantum numbers of angular momentum and isospin are important elements of the approach. The distribution of off-diagonal many-body matrix elements is close to exponential which seems to be a generic, although not well understood, feature for realistic systems [35].

Having at our disposal the exact solution of the many-body Schrödinger equation, although in limited Hilbert space, we proceed to analyze the global level density and local correlations and fluctuations of energy levels (Section 3). The system turns out to reveal the standard GOE signatures of quantum chaos in the level statistics [nearest level spacing distribution $P(s)$ and spectral rigidity $\Delta(L)$]. Our hamiltonian does not contain any random elements. The chaoticity arises as a result of strong mixing of the “simple” basis states by residual interactions. We will explore the dependence of chaoticity on the relative strength of the interaction with respect to the mean field level spacing and the dynamics of the level crossings under the variation of the hamiltonian (the distribution of level curvatures).

In Section 4 we begin to study the structure of stationary wave functions which is more sensitive to deviations from the GOE limit. The evolution of complexity of eigenfunctions along the spectrum continues long after the level statistics signal onset of chaos. We use information entropy and the moments of the distribution function of the eigenvector components to quantify the degree of complexity of the eigenfunctions. These measures of complexity are representation dependent. They behave in a regular smooth way as a function of excitation energy provided they are expressed in terms of the “natural” mean field basis. The basis dependence is studied in detail, and the exceptional role of the mean field basis is confirmed by the results.

Detailed behavior of the distribution function of the eigenvector components in the original basis as well as the spreading of the basis states are discussed in Section 5. We compare our results with the predictions of statistical spectroscopy by French and others [53–56] and with the “standard” (golden-rule) model of the strength function [21]. We discuss the behavior of the spreading width as a function of excitation energy which is closely related to the problem of the saturation of the giant resonance width with increasing temperature [42, 44]. Another unresolved problem (see for example [35]) is the shape of the wings of the distribution function of the components. The routinely used Breit–Wigner distribution overestimates the weight of the remote admixtures, which influences weak interaction effects [57], and the spreading of the multiple-phonon excitations [58, 59]. We investigate this problem for our shell-model states and find evidence for the exponentially decaying tails of a generic strength function. The standard golden-rule model for the spreading width and the Breit–Wigner shape can be restored by an artificial reduction of the interaction strength, in accordance to the theoretical arguments presented in [59, 44].

Section 6 is devoted to the discussion of the interplay between chaos and thermalization. We show that the eigenfunctions of the states close in energy in the chaotic region really “look the same”. This is the prerequisite which allows one to introduce the corresponding thermal equilibrium ensemble. The nucleon occupation numbers turn out to be a smooth function of excitation energy which agrees well with the equilibrium Fermi–Dirac distribution. This resolves the apparent contradiction between the Fermi-liquid theory and quantum chaos. In a suitable representation related to the quasiparticle energies in the mean field, the response of a many-body system even in the stochastic regime can be expressed in terms of heated quasiparticles. Another conclusion is that, in the same natural basis, information entropy of individual states increases in parallel to standard microcanonical entropy and to entropy of the heated quasiparticle gas. Therefore the degree of complexity can be used as an alternative temperature scale. We believe that further studies in this direction can shed new light on the problem of the foundation of statistical mechanics.

In Section 7 we illustrate the process of stochastization of collective degrees of freedom by the evolution of pairing with the excitation energy. The lowest states reveal strong pairing correlations rapidly decreasing with temperature similar to the phase transition in superconductors. However one sees a long tail at higher temperatures and the constant level of pairing fluctuations in the “normal” phase which is in agreement with estimates by statistical spectroscopy and with the Fermi gas expectations.

We conclude with the (certainly incomplete) list of open problems in the field of chaotic quantum dynamics in realistic many-body systems.

2. Shell-model calculations

We base our analysis on the results of the exact diagonalization of the effective hamiltonian H in a large $N \times N$ Hilbert space spanned by a truncated set of shell-model nuclear configurations. Each configuration is characterized by the distribution of independent fermions over available spherical single-particle orbitals. Within a configuration, various ways to occupy the magnetic substates of the j -levels give rise to the “ m -scheme” Slater determinants.

Our hamiltonian H keeps rotational and isospin invariance. For a given configuration, there still exists a freedom of choice for the coupling of angular momenta (isospins) of individual particles into the total angular momentum (isospin). We construct our basis states designated below as $|k\rangle$ combining the m -scheme determinants in such a way that they have good quantum numbers of the total angular momentum J , its projection M , parity π , isospin T and its projection T_3 . Therefore the states $|k\rangle$ are far from being simple Slater determinants.

The projection required by the exact symmetry of the system plays an important role in generating complexity. The necessity of using the appropriate $J^\pi T$ states instead of the simple m -scheme determinants was demonstrated already in the first studies of quantum chaos in the nuclear shell model [51]. This “premixing” is absent in the attempts to analyze the complexity of high spin rotational bands (“rotational damping” [60]) in the framework of the cranking model [61]. The cranking model does not preserve the angular momentum. It operates with quasiparticle configurations similar to those of the m -scheme of the spherical shell model but taken for a deformed uniformly rotating field. Absence of correct premixing (or angular momentum projection) implies artificial mixing by the residual interaction since angular momentum selection rules are lifted. It is uncertain as to what extent the net result of this interplay distorts the final picture.

We note parenthetically that the mixing of m -states due to the angular momentum coupling poses an interesting problem which apparently has not been addressed in the literature. Even in the restricted space of a single major shell, a specific choice of one of the large number of possible coupling schemes leads to a specific “geometrical chaoticity”. High- j ($6j$, $9j$ etc.) symbols related to the recoupling transformation between different schemes have almost random signs and behave similar to the elements of a very complicated matrix. Physically this justifies using the idea of random angular momentum coupling in the discussion of many-body level densities [62]. The degree of geometrical chaoticity was utilized as a specific parameter for discriminating the Feynman diagrams in the problem of strong coupling of a nucleon [63] or a giant resonance [64] with low-frequency quadrupole phonons. The angular momenta of virtual phonons are coupled randomly except for the coherent rainbow diagrams where the phonons are sequentially absorbed opposite to the order of their radiation [63]. This is the same class of diagrams (“pairwise contractions”) which survives [7] in the calculation of the average Green function and the level density in the large dimension limit of the random matrix theory. The question of geometrical chaoticity deserves to be developed more in detail.

2.1. General formulation

The effective shell-model hamiltonian H consists of the independent particle (one-body) part H_0 and the residual interaction H' of the two-body type:

$$H = H_0 + H' . \quad (1)$$

The unperturbed hamiltonian $H_0 = \sum_{\lambda} e_{\lambda} a_{\lambda}^{\dagger} a_{\lambda}$ describes noninteracting fermions in the mean field of the appropriate spherical core. The single-particle orbitals $|\lambda\rangle$ have quantum numbers $\lambda = (ljm\tau)$ of orbital (l) and total (j) angular momentum, projection $j_z = m$ and isospin projection τ . The eigenvalues ε_k of H_0 ,

$$H_0 |k\rangle = \varepsilon_k |k\rangle, \quad (2)$$

are highly degenerate. They are the sums

$$\varepsilon_k = \sum_{\tau} e_{\lambda} n_{\lambda}(k) \quad (3)$$

of energies e_{λ} of all orbits $|\lambda\rangle$ occupied in a many-body configuration $|k\rangle$ with occupation numbers $n_{\lambda}(k)$, equal to 1 or 0. The spherical orbital energies $e_{\lambda} \equiv e_{lj}$ do not depend on m and τ . The energies ε_k are the same for all angular momentum coupling schemes allowed by a given configuration $\{n_{\lambda}\}$.

In the basis $|k\rangle$, the residual interaction H' has both diagonal, \bar{H} , and off-diagonal, \tilde{H} , matrix elements, $H' = \bar{H} + \tilde{H}$. The diagonal part \bar{H} already lifts some degeneracy of ε_k . Full diagonalization in each sector with given exact quantum numbers leads to the stationary states $|\alpha\rangle$,

$$H |\alpha\rangle = E_{\alpha} |\alpha\rangle, \quad (4)$$

which can be represented by superpositions of unperturbed states $|k\rangle$,

$$|\alpha\rangle = \sum_k C_k^{\alpha} |k\rangle. \quad (5)$$

The amplitudes C_k^{α} can be taken as real in the case of the interaction invariant under time reversal. Since the transformation from the unperturbed basis $|k\rangle$ to the eigenbasis $|\alpha\rangle$ is unitary, the same coefficients (5) describe the spreading of the basis states $|k\rangle$ over the eigenstates $|\alpha\rangle$. The amplitudes satisfy the orthonormalization conditions

$$\sum_k C_k^{\alpha} C_k^{\alpha'} = \delta^{\alpha\alpha'}, \quad \sum_{\alpha} C_k^{\alpha} C_{k'}^{\alpha} = \delta_{kk'}. \quad (6)$$

A completely delocalized function would have a number of components, which contribute effectively to the normalization (6), close to the value of the dimension N . In this limit the typical magnitude of each component is $1/\sqrt{N}$. In general, a number N_{α} of principal components $|k\rangle$ characterizes the delocalization of a state $|\alpha\rangle$ in the given basis (2). The corresponding amplitudes have an order of magnitude $1/\sqrt{N_{\alpha}}$.

2.2. Angular momentum and isospin projection

Throughout the paper, our model hamiltonian almost exclusively describes a many-body system of valence particles in one major shell. Examples are the sd shell (24 states including $0d_{5/2}$, $0d_{3/2}$ and $1s_{1/2}$ single-particle orbits) and the fp shell (40 states including $0f_{7/2}$, $0f_{5/2}$, $1p_{3/2}$ and $1p_{1/2}$ single-particle orbits). The one-body part (2) of the total hamiltonian (1) is due to an existing core (^{16}O for the sd shell and ^{40}Ca for the fp shell). In addition we have an antisymmetrized two-body interaction of the valence particles,

$$H' = \frac{1}{4} \sum V_{\lambda\mu, \nu\rho} a_{\lambda}^{\dagger} a_{\mu}^{\dagger} a_{\nu} a_{\rho}. \quad (7)$$

To construct the many-body wave functions with good spin J and isospin T quantum numbers, we start with the m -scheme determinants which have, for given J and T , the maximum spin and isospin projection,

$$|M = J, T_3 = T; m\rangle, \quad (8)$$

where m span the m -scheme subspace of states with $M = J$ and $T_3 = T$. One can introduce also configurations (partitions) \mathcal{P} which are defined by the occupancies $n_\lambda(k)$ of single-particle orbitals. All states $|k\rangle$ belonging to a partition \mathcal{P} have the same set of $n_\lambda(k)$. For all partitions, $\sum_\lambda n_\lambda(k) = A_v$, the total number of valence particles.

The organization of the model space in partitions present two useful features. A subspace of the m -scheme states (8) defined by a given configuration \mathcal{P} is invariant with respect to the projection onto good total angular momentum J and total isospin T ,

$$|JT; k \subset \mathcal{P}\rangle = \hat{P}_{JT} |MT_3; m_k \subset \mathcal{P}\rangle = \sum_{m \subset \mathcal{P}} X_m^{JTk} |MT_3; m\rangle. \quad (9)$$

This can be easily seen using the explicit expression for the projection operator:

$$\hat{P}_{J_0 T_0} = \prod_{J \neq J_0}^{J_{\max}} \frac{\hat{J}_- \hat{J}_+ + \hat{J}_3^2 + \hat{J}_3 - J(J+1)}{J_0(J_0+1) - J(J+1)} \prod_{T \neq T_0}^{T_{\max}} \frac{\hat{T}_- \hat{T}_+ + \hat{T}_3^2 + \hat{T}_3 - T(T+1)}{T_0(T_0+1) - T(T+1)}. \quad (10)$$

Secondly, the m -scheme states (8) and, as a consequence of the invariance of the projection, the projected states (9) also, are degenerate with respect to the one-body part of the hamiltonian (2).

The projected states are used to build the matrix of the many-body hamiltonian:

$$H_{kk'}^{JT} = \langle JT; k | H | JT; k' \rangle. \quad (11)$$

Here different partitions as well as the basis states within a partition are mixed by the residual interactions. The matrix (11) is eventually diagonalized to obtain the eigenvalues E_α and the eigenvectors (5)

$$|JT; \alpha\rangle = \sum_k C_k^\alpha |JT; k\rangle. \quad (12)$$

They represent the object of our investigation of chaotic properties of the quantum many-body system.

Similar studies can be performed using the “proton–neutron” (p–n) formalism with no explicit isospin. Below we show some examples of such calculations. Since the space dimensions increase as compared to the calculations with the isospin projection, for such cases we take a smaller particle number (^{24}Mg system of 4 protons and 4 neutrons). We use this opportunity also to check the stability of the results against slight variations of residual interactions.

2.3. The model

We have chosen as the main object of our analysis a system of $A_v = 12$ particles in the sd shell which mimics (for $T_3 = 0$) a subset of states in the ^{28}Si nucleus. In some cases (as noted) we also show results of similar calculations for systems with a smaller number of valence particles. We use

the Wildenthal hamiltonian [65] which defines the single-particle energies e_λ and the interaction between the valence particles by fitting more than 400 binding energies and excitation energies for the sd-shell nuclei. In computations with the proton–neutron scheme, we used, along with the same Wildenthal interaction rewritten for the p–n scheme (WPN), the interaction (WPNC) which explicitly violates isospin on the experimentally allowed level by including the Coulomb interaction and isospin-nonconserving isovector and isotensor nuclear forces [67]. All calculations were carried out with the computer program OXBASH [66], which uses the m -scheme basis states together with the angular momentum projection operators to construct and diagonalize matrices with good J and T in the isospin formalism and good J in the proton–neutron formalism.

Taking into account total angular momentum and isospin conservation, there are 63 non-vanishing two-body matrix elements $\langle (j_1 j_2)_{JT} | H' | (j_3 j_4)_{JT} \rangle$ in sd-shell space. They are listed in Table 1 classified according to the quantum numbers of the initial (j_3, j_4) and final (j_1, j_2) states of the nucleon pair and by the values of J and T conserved in the interaction.

Being in general of the order of an MeV, the two-body matrix elements show significant attraction in the $T = 1$ states with even angular momenta. All the matrix elements for $T = 1$ and $J = 0, 2$ and 4 (the only quantum numbers allowed for identical nucleons on the same j -level) are negative which is a clear signature of pair correlations. Another noticeable feature of the residual interaction is very strong diagonal attraction for isoscalar pairs ($T = 0$). All the matrix elements for the expectation values of H' in the pair states with $T = 0$ are negative, being especially large for high angular momenta. This shows the tendency of the valence particles to create oblate deformation. In contrast to that, the $T = 0$ nondiagonal (scattering) matrix elements are mainly of repulsive character. In Table 2 we give the dimensions $N(J^{\pi} T)$ for all total angular momenta J and isospins $T = 0$ and $T = 1$ allowed for 12 valence particles in the sd shell. In our calculations, we mostly use the 2^+0 and 0^+0 classes of states, although high angular momenta such as 9^+0 will be used for comparison as well.

2.4. Strength functions and fragmentation widths

Prior to the actual diagonalization, we can study important characteristics of the system by analyzing the properties of the hamiltonian matrix. Long ago such analyses were carried out by statistical spectroscopy [53].

2.4.1. Strength function and centroids of the basis states

Diagonal matrix elements are dominated by the one-body part H_0 . The two-body diagonal contributions \bar{H} split the degenerate levels within the partitions so that each partition covers a small region on the “unperturbed” energy axis (with the energy $H_{kk} = \varepsilon_k + \bar{H}_{kk}$ of each individual basis state $|k\rangle$) which partly overlaps with the regions of other partitions. In our $A = 28$ example, the diagonal part of the hamiltonian is spread from -120 MeV to -60 MeV.

The basis states $|k\rangle$ will be mixed by the off-diagonal part \hat{H} . Two-body matrix elements between the many-body basis states are typically of the order of hundreds keV. The fragmentation of the basis states over the eigenstates $|\alpha\rangle$ is determined by the matrix C_k^α of Eq. (5), namely by the weights of the components

$$W_k^\alpha \equiv (C_k^\alpha)^2 . \quad (13)$$

Table 1

Two-body reduced matrix elements (in MeV) of the residual interaction within the sd shell-model space

$T = 1 \ J = 0$	$s_{1/2}^2$		$d_{3/2}^2$		$d_{5/2}^2$
$s_{1/2}^2$	- 2.125		- 1.084		- 1.325
$d_{3/2}^2$			- 2.185		- 3.186
$d_{5/2}^2$					- 2.820
$T = 1 \ J = 2$	$d_{3/2}^2$	$d_{5/2}^2$	$s_{1/2}d_{3/2}$	$s_{1/2}d_{5/2}$	$d_{5/2}d_{3/2}$
$d_{3/2}^2$	- 0.067	- 1.622	- 0.515	- 0.404	- 0.615
$d_{5/2}^2$		- 1.002	- 0.620	- 0.862	- 0.283
$s_{1/2}d_{3/2}$			- 0.406	- 1.941	- 0.525
$s_{1/2}d_{5/2}$				- 0.818	- 0.477
$d_{5/2}d_{3/2}$					- 0.325
$T = 1 \ J = 4$		$d_{5/2}^2$		$d_{5/2}d_{3/2}$	
$d_{5/2}^2$		- 0.164		- 1.236	
$d_{5/2}d_{3/2}$				- 1.450	
$T = 1 \ J = 1$		$s_{1/2}d_{3/2}$		$d_{5/2}d_{3/2}$	
$s_{1/2}d_{3/2}$		+ 0.607		+ 0.187	
$d_{5/2}d_{3/2}$				+ 1.033	
$T = 1 \ J = 3$		$s_{1/2}d_{5/2}$		$d_{5/2}d_{3/2}$	
$s_{1/2}d_{5/2}$		+ 0.762		+ 0.674	
$d_{5/2}d_{3/2}$				+ 0.589	
$T = 0 \ J = 1$	$s_{1/2}^2$	$d_{3/2}^2$	$d_{5/2}^2$	$s_{1/2}d_{3/2}$	$d_{5/2}d_{3/2}$
$s_{1/2}^2$	- 3.263	+ 0.028	- 1.176	+ 1.250	+ 2.104
$d_{3/2}^2$		- 1.415	+ 0.722	+ 0.398	+ 0.565
$d_{5/2}^2$			- 1.632	- 1.103	+ 2.543
$s_{1/2}d_{3/2}$				- 4.293	- 1.710
$d_{5/2}d_{3/2}$					- 6.506
$T = 0 \ J = 3$	$d_{3/2}^2$	$d_{5/2}^2$	$s_{1/2}d_{5/2}$	$d_{5/2}d_{3/2}$	
$d_{3/2}^2$	- 2.884	+ 1.895	+ 0.189	+ 2.034	
$d_{5/2}^2$		- 1.501	- 1.242	+ 2.222	
$s_{1/2}d_{5/2}$			- 3.860	+ 1.203	
$d_{5/2}d_{3/2}$				- 0.538	

Table 1 Continued.

$T = 0 \quad J = 5$		$d_{5/2}^2$	
$d_{5/2}^2$		– 4.226	
$T = 0 \quad J = 2$	$s_{1/2}d_{3/2}$	$s_{1/2}d_{5/2}$	$d_{5/2}d_{3/2}$
$s_{1/2}d_{3/2}$	– 1.819	+ 2.066	+ 0.283
$s_{1/2}d_{5/2}$		– 1.447	+ 0.097
$d_{5/2}d_{3/2}$			– 3.825
$T = 0 \quad J = 4$		$d_{5/2}d_{3/2}$	
$d_{5/2}d_{3/2}$		– 4.506	

Table 2
Dimensions of subspaces $J^{\pi}T$ for 12 particles in the sd shell

T	J														
	0	1	2	3	4	5	6	7	8	9	10	11	12	13	14
0	839	2135	3276	3711	3793	3278	2667	1848	1205	657	334	126	48	8	1
1	1372	3985	5768	6706	6562	5755	4434	3097	1882	1023	462	178	48	9	0
2	874	2319	3434	3804	3700	3059	2285	1462	844	393	160	44	9	0	0

We characterize the fragmentation of the simple state $|k\rangle$ over the energy spectrum by the strength function

$$F_k(E) = \langle k | \delta(E - H) | k \rangle = \sum_{\alpha} W_k^{\alpha} \delta(E - E_{\alpha}) . \quad (14)$$

As follows from $\sum_{\alpha} W_k^{\alpha} = 1$, the strength functions are normalized by

$$\int dE F_k(E) = 1 . \quad (15)$$

Without the full knowledge of the strength function, one can describe the fragmentation of simple states by the lowest moments [53] which do not require the actual diagonalization. The centroid \bar{E}_k of the energy distribution of the original basis state $|k\rangle$ coincides with the unperturbed

energy H_{kk} ,

$$\begin{aligned}\bar{E}_k &\equiv \int dE E F_k(E) = \sum_{\alpha} E_{\alpha} W_k^{\alpha} \\ &= \sum_{\alpha\alpha'} \langle k|\alpha\rangle \langle \alpha|H|\alpha'\rangle \langle \alpha'|k\rangle = H_{kk} = \varepsilon_k + \bar{H}_{kk}\end{aligned}\quad (16)$$

where the completeness arguments were used. The spread of the unperturbed energies due to the diagonal elements of the interaction (no mixing at this stage) can be characterized by the rms deviation Δ_E of the centroids \bar{E}_k from the energy center \bar{E} ,

$$\bar{E} = \frac{1}{N} \sum_k \bar{E}_k, \quad \Delta_E^2 = \frac{1}{N} \sum_k (\bar{E}_k - \bar{E})^2. \quad (17)$$

For the 2^+0 states $\Delta_E \approx 8$ MeV.

2.4.2. Energy dispersion of basis states

We define the higher (central) moments of the strength function as

$$\sigma_k^{(n)} = \int dE (E - \bar{E}_k)^n F_k(E) = \sum_{\alpha} (E_{\alpha} - \bar{E}_k)^n W_k^{\alpha}. \quad (18)$$

Using again completeness arguments, these quantities can be expressed in terms of the matrix elements H_{kl} of the original hamiltonian (1). For example,

$$\sigma_k^{(2)} \equiv \sum_{\alpha} (E_{\alpha} - \bar{E}_k)^2 W_k^{\alpha} = \sum_{\alpha} E_{\alpha}^2 W_k^{\alpha} - \bar{E}_k^2 = \sum_{l(\neq k)} (H_{lk})^2 = (\tilde{H}^2)_{kk}, \quad (19)$$

i.e. the energy dispersion $\sigma_k \equiv (\sigma_k^{(2)})^{1/2}$ is equal to the square root of the sum of the squared off-diagonal matrix elements for a given unperturbed initial state. We will use the notation

$$\bar{\sigma}^2 = \frac{1}{N} \sum_k \sigma_k^2 = \frac{1}{N} \left(\sum_{\alpha} E_{\alpha}^2 - \sum_k \bar{E}_k^2 \right) \quad (20)$$

for the average dispersion of the states $|k\rangle$. The centroids and dispersions can also be obtained for a subclass of the states $|k\rangle$, for example, for each partition \mathcal{P} separately.

Fig. 1(a) shows the distribution of partitions for 3276 states $|k\rangle$ with $J^{\pi}T = 2^+0$ ordered with the increasing unperturbed energy \bar{E}_k . The regular pattern of overlapped partitions spread out typically over 5–10 MeV is clearly seen. In Fig. 1(b) the partitions are substituted by their centroids according to French and Ratcliff [53].

The energy dispersion (19) of individual 2^+0 basis states turns out (Fig. 2) to be remarkably uniform, $\sigma_k \approx \bar{\sigma} \approx 10$ MeV over the entire space. The remnants of the partition structure are visible as tails of a slightly diminished dispersion at the low lying edge of the partition. This might be caused by a random choice of the initial simple states (8) in the beginning of the projection procedure. The dispersion σ_k is closely related to the spreading width defined more precisely in Sections 5. The uniformity of the dispersion supports the idea of saturation of the spreading width [42, 44] which has important consequences for understanding the damping of giant resonances. For 0^+0 states the partition pattern is essentially the same (Fig. 3) with the same value of the average energy dispersion $\bar{\sigma}$ (Fig. 4), although the fluctuations are more significant.

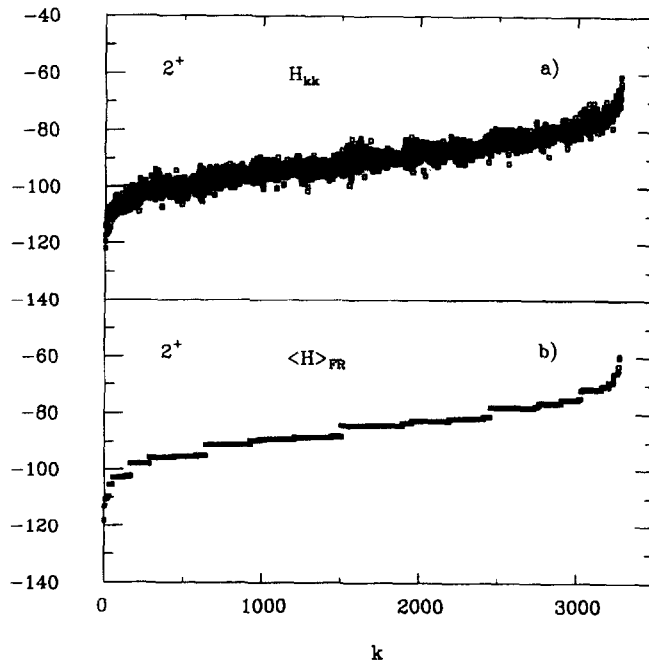


Fig. 1. Diagonal matrix elements H_{kk} for 2^+0 states of 12 particles in the sd shell (the states $|k\rangle$ are numbered in the order of increasing H_{kk}), (a) values for individual states, (b) energy centroids of partitions found according French and Ratcliff [53].

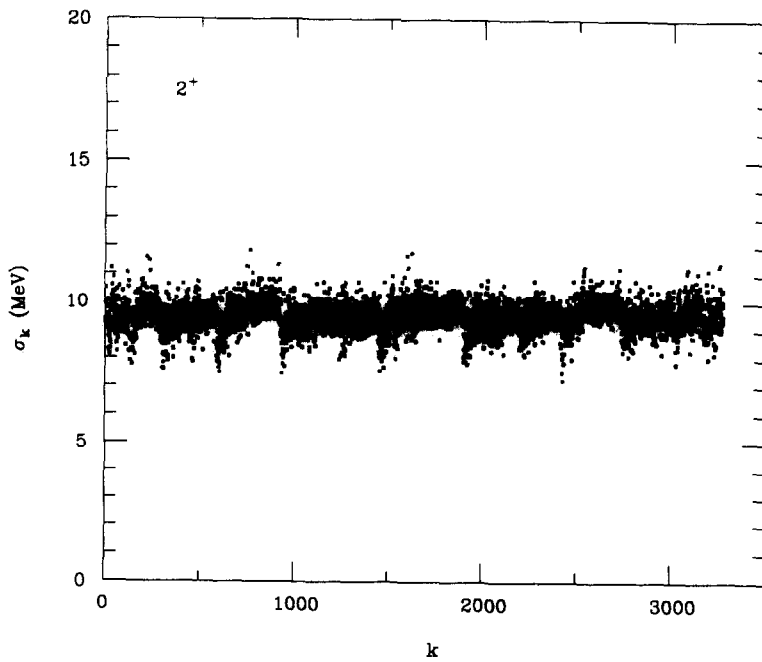


Fig. 2. Energy dispersions σ_k of basis 2^+0 states.

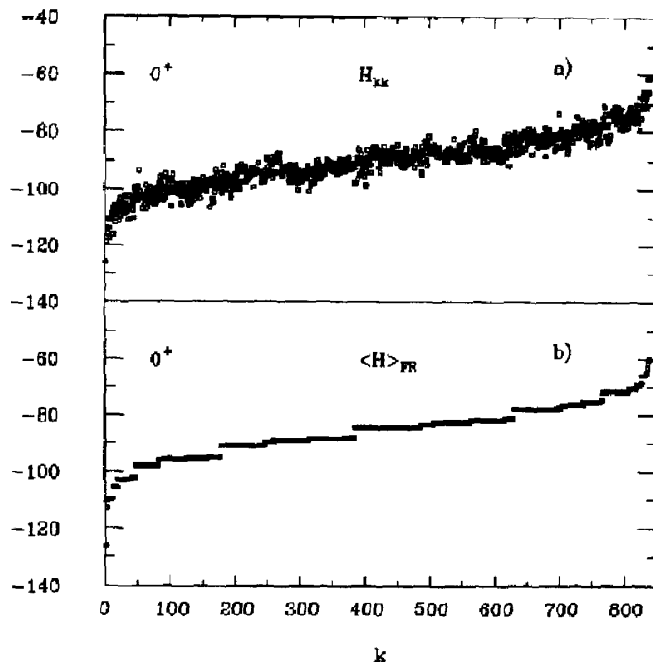


Fig. 3. The same as Fig. 1 for the 0^+0 states.

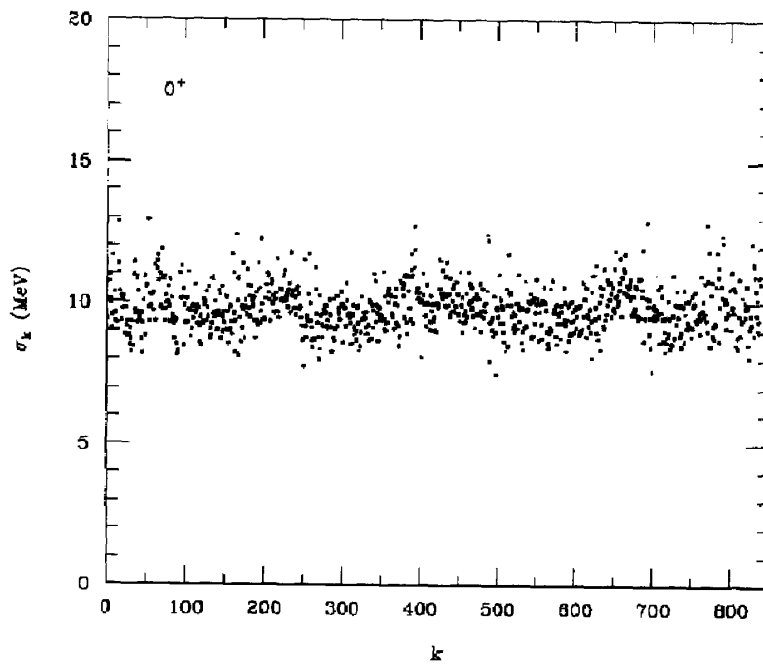


Fig. 4. The same as Fig. 2 for the 0^+0 states.

Since variations of the effective spreading (19) of the basis states around the mean value $\bar{\sigma}$ are small, one can work out [69] a simple truncation method to reduce a huge shell-model hamiltonian matrix to a manageable size. The method was tested for the sd and fp shells and was proven to be very efficient. In the middle of the fp shell (JT dimensions of the order of a few million) the size of the matrix is effectively reduced to a few thousand.

In a similar way one can compute the higher energy moments of the component distribution as

$$\sigma_k^{(3)} = \sum_{\alpha} (E_{\alpha} - \bar{E}_k)^3 W_k^{\alpha} = (\tilde{H}^3)_{kk} - \bar{E}_k \sigma_k^2, \quad (21)$$

$$\sigma_k^{(4)} = \sum_{\alpha} (E_{\alpha} - \bar{E}_k)^4 W_k^{\alpha} = (\tilde{H}^4)_{kk} + \sigma_k^2 (\bar{E}_k^2 + \sigma_k^2) + 2\bar{E}_k (\tilde{H}(\bar{H} - \tilde{H})\tilde{H})_{kk}. \quad (22)$$

Physics of the spreading and related questions will be discussed more in detail in Section 5.

2.4.3. Moments of the level density

Valuable information concerning the spectrum of the exact stationary states $|\alpha\rangle$ also can be obtained prior to the actual diagonalization. The primary characteristic of the spectrum is the level density

$$\rho(E) = \sum_{\alpha} \delta(E - E_{\alpha}). \quad (23)$$

Following Wigner [68], the strength function $F_k(E)$ of Eq. (14) is sometimes called “local density of states”. It defines the contribution to the level density at energy E of a given basis state $|k\rangle$. The total level density of the eigenstates (23) $|\alpha\rangle$ is given by the sum of the strength functions over all $|k\rangle$,

$$\rho(E) = \sum_{\alpha} \delta(E - E_{\alpha}) = \text{Tr} \delta(E - H) = \sum_k F_k(E). \quad (24)$$

It is normalized to the total number of states,

$$\int dE \rho(E) = N. \quad (25)$$

In a finite space one can define, similar to (17) and (18), the moments of the total level density (24). The average energy

$$\frac{1}{N} \int dE E \rho(E) = \bar{E} \quad (26)$$

coincides with the energy center introduced by Eq. (17). The total dispersion of energy

$$\sigma_E^2 \equiv \frac{1}{N} \int dE (E - \bar{E})^2 \rho(E) = \bar{\sigma}^2 + \Delta_E^2 \quad (27)$$

consists of (added in quadratures) the spread (17) of centroids defined by the diagonal part of the hamiltonian and the fragmentation width (20) due to the off-diagonal part. With the above-mentioned values of $\bar{\sigma}$ and Δ_E for the 2^+0 states we get $\sigma_E = 13$ MeV.

2.5. Banded properties of the hamiltonian matrix

During the last few years much progress has been made in generalizing random matrix theory to banded (“bordered” by Wigner’s terminology) random matrices (BRM) [71, 72]. In contrast to the canonical (orthogonal, unitary or symplectic) Gaussian ensembles with the distribution functions invariant under transformations preserving the corresponding symmetry, the BRM are given in a special basis. In this basis the basis states are ordered in such a way that a hamiltonian matrix has a band of nonzero matrix elements H_{kl} interconnecting the states within the band $|k - l| \leq b$ around the main diagonal. The number b is called the width of the band. For the Gaussian distribution of the nonzero matrix elements, the properties of the ensemble are predicted [72] to be determined by the scaling parameter b^2/N .

The partition structure of our Hilbert space, which is revealed in the shell-model basis but can be lost after a transition to an arbitrary representation, gives rise to distinct band-like features. As a rule, the interaction between the unperturbed projected configuration states $|k\rangle$, which are widely separated in centroid energy \bar{E}_k , is weaker than between the close configurations. This interaction energy range for the individual states can be measured using the definition [70]

$$\omega_k^2 = \frac{1}{\sigma_k^2} \sum_l (\bar{E}_k - \bar{E}_l)^2 |\tilde{H}_{kl}|^2. \quad (28)$$

The smooth behavior, Fig. 5, of this quantity enables one to compare the shell-model hamiltonian matrix with the banded matrices. According to Fig. 5, the effective width of the band is $\omega \approx 7.5$ MeV both for the 0^+0 states and for the 2^+0 states. This corresponds to approximately 200 to 250 unperturbed states within the band. In Fig. 6 the banded properties of the hamiltonian matrix are depicted in a different way (here for the 0^+0 states). The dependence on the distance from the main diagonal displays the banded character with the width $b \approx 250$.

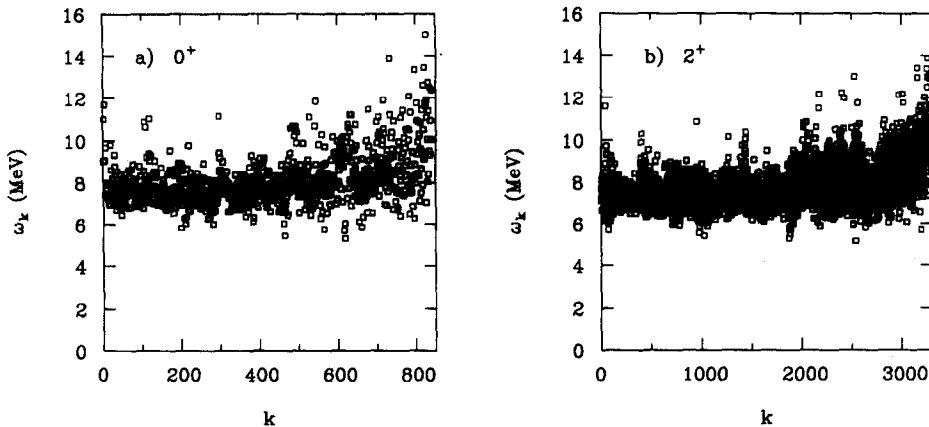


Fig. 5. The energy range of interaction between the unperturbed projected configurations, Eq. (28), for the 0^+0 (a) and 2^+0 (b) states.

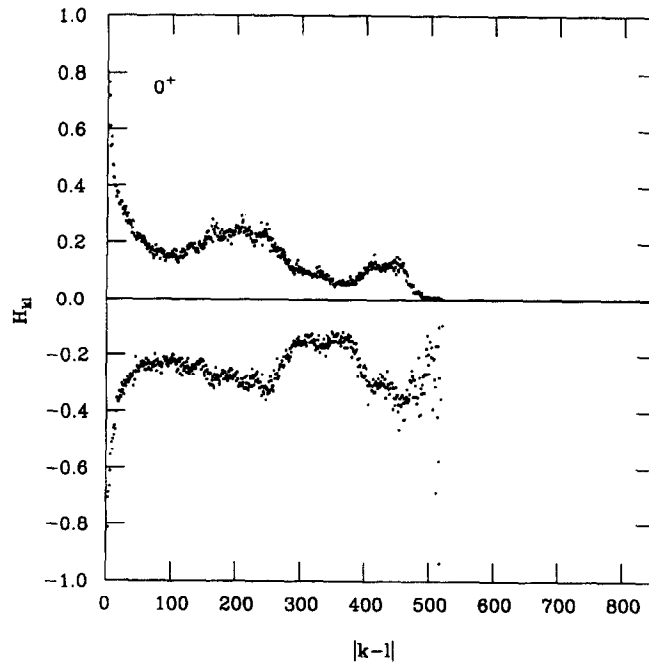


Fig. 6. Matrix elements H_{kl} (in MeV) between the basis states as a function of the distance $|k-l|$ for the 0^+0 states numbered according to the increasing energy. For each value of $|k-l|$ the average values of all positive and all negative matrix elements are shown.

The typical number $2b$ of states coupled to a given state $|k\rangle$ in the middle part of the spectrum can also be directly estimated from (19). For the 2^+0 states, $2b \approx \bar{\sigma}^2/\bar{H}^2 \approx 400$ where we use $\bar{H} \approx 0.5$ MeV as an rms value of the off-diagonal many-body matrix element. The parameter b^2/N is therefore very large in our case which implies that the localization properties of the eigenstates are different from those considered in [72]. The standard BRM theory considers matrices in which the diagonal matrix elements do not increase monotonically. In the nuclear case the presence of the monotonically increasing diagonal part generated by the mean field (centroids \bar{E}_k) is crucial for many statistical regularities.

The banded structure of the shell-model hamiltonian is the reflection of the selection rules specific for the two-body interaction (exact selection rules related to conservation of angular momentum and isospin are already accounted for by the projection inside a partition). The emerging structure of interpartition links is clearly seen in Fig. 7. At the same time there is no distinct order for the submatrix of the hamiltonian within a given partition. As shown in Fig. 8, the off-diagonal matrix elements in the largest 0^+0 partition cover the field of the matrix more uniformly (only matrix elements with magnitude greater than 0.5 MeV are shown).

Another theoretical model which has some similarity with our system is the two-body random ensemble of Brody et al. [7]. Again we have to stress that our hamiltonian matrix is neither random nor banded in the strict meaning of this term because, due to the two-body selection rules, it is impossible to reach a precisely banded form by reordering.

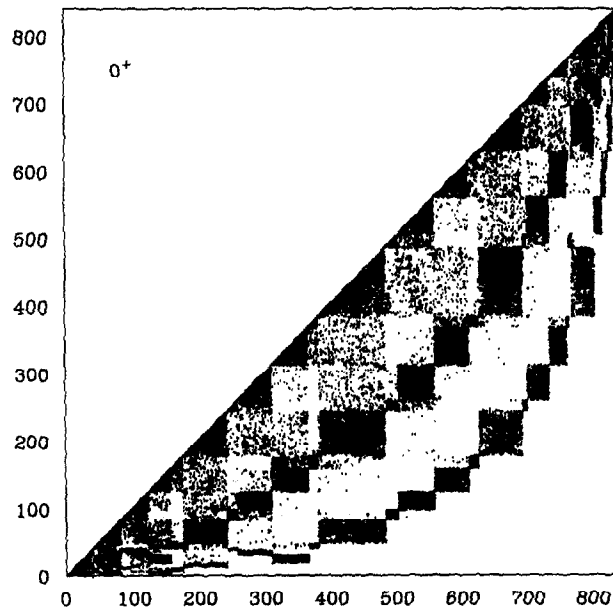


Fig. 7. The hamiltonian matrix for the 0^+0 states.

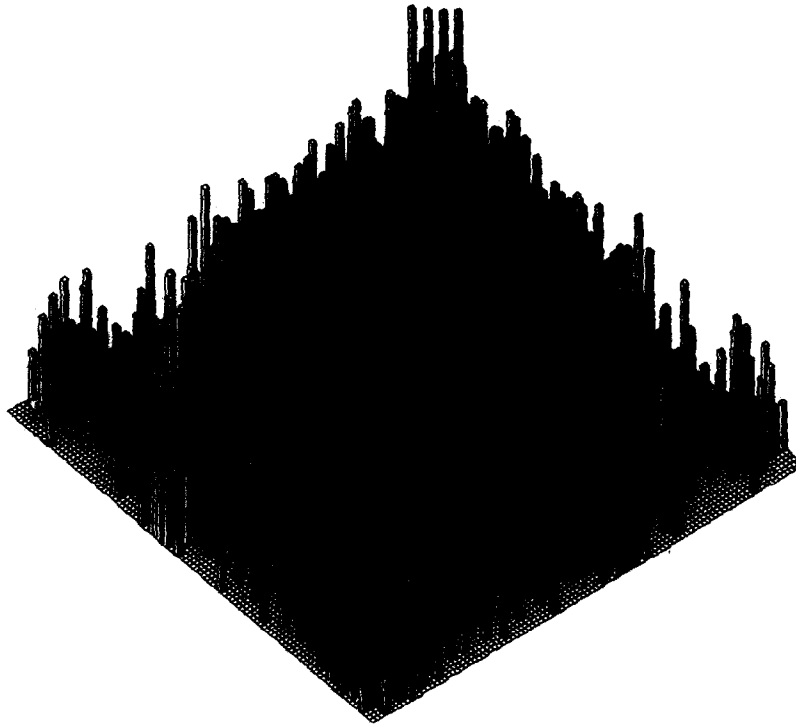


Fig. 8. Off-diagonal matrix elements of the magnitude larger than 0.5 MeV between the 0^+0 states within the largest partition, the dimension is $N = 103$.

2.6. Distribution of matrix elements

The random matrix theory usually considers matrix elements of the hamiltonian as random normally distributed variables. In the canonical Gaussian ensembles, the matrices have no regularly increasing diagonal elements. Therefore these ensembles have nothing to do with the evolution along the spectrum (“secular” behavior) and can properly account for the local correlations and fluctuations only. In our case of a time-reversal invariant system, we shall use for comparison the GOE. We write down the pair correlation function for matrix elements of the hamiltonian in the GOE as

$$\overline{H_{kl} H_{k'l'}}^{\text{GOE}} = (a^2/4N) (\delta_{l'k} \delta_{kl} + \delta_{k'k} \delta_{l'l}) \quad (29)$$

where the center of the spectrum is taken as the origin of the energy scale, $\overline{H_{kl}} = 0$. Here and below the bar stands for the ensemble average. Due to the orthogonal invariance of the GOE, Eq. (29) is valid in an arbitrary basis. Since in the GOE case there is no subdivision into parts analogous to H_0 and H' in (1), all matrix elements have the same variance (29) with the only difference in a factor two for the diagonal matrix elements compared to the off-diagonal.

The normalization used in (29) implies the idea of N -scaling [29, 43, 30, 42]. If, in a given ordered basis $|k\rangle$, the expansion (5) of generic stationary functions $|\alpha\rangle$ is concentrated in a compact region, the number of principal simple components corresponds to the localization length l in Hilbert space [5, 71]. This language comes from the theory of disordered solids where localization has its direct meaning in the coordinate space. However, one should keep in mind that in the solid state case the coordinate localization manifests chaoticity, since the hamiltonian of a perfect crystal would have completely delocalized Bloch waves as its eigenstates. A closer analogy can be found in the quantum chaotic systems as kicked rotor [5] where classical diffusion is saturated on a finite level by the quantum interference of the components of the wave function. This phenomenon is typical for banded hamiltonians [3, 72] and reflects the finite energy range of interaction.

As the level density increases and the basis states get strongly mixed, the eigenstates become exceedingly complicated superpositions of the basis states (in the Introduction this process was called stochastization). The typical matrix elements of simple operators (for example, those of the one-body operators or two-body residual interaction) between the complicated states on average decrease $\sim l^{-1/2}$ [29, 43]. At the same time, the energy range $\Gamma \simeq lD$ ($D \sim \rho^{-1}$ is the average level spacing) characterizes the spreading width of simple states with their strength fragmented among the eigenstates (5). In the stochastic regime, the typical magnitude of mixing matrix elements can be estimated as $|\overline{H'_{12}}| \simeq v/l^{-1/2}$, where v is the characteristic strength of original matrix elements of the residual interaction between simple states. In the GOE limit of complete delocalization, generic wave functions cover the entire finite Hilbert space, $l \simeq N$. Then we come to the estimate $|\overline{H'_{12}}|^2 \simeq v^2/N$, and Eq. (29) shows that the parameter a should be of the same order of magnitude as typical matrix elements v .

The Gaussian ensemble of banded random matrices (BRM) can be defined as a straightforward generalization of (29). For each matrix element, the distribution function is still Gaussian with the mean value equal to zero but the variances depend now on the “distance” between the states in the matrix element,

$$\overline{H_{kl} H_{k'l'}}^{\text{BRM}} = (a^2/4N) (\delta_{k'l} \delta_{l'k} + \delta_{k'k} \delta_{l'l}) \eta_{kl} \quad (30)$$

where η_{kl} reflects selection rules which effectively confine nonzero matrix elements to the band $|k - l| \simeq b$. The band can be taken to have a sharp boundary with $\eta_{kl} = 0$ for $|k - l| > b$ but the exact way in which the matrix elements decrease is not significant [72]. Now the orthogonal invariance is lost, and the representation (30) with a distinct band structure takes place in a specific ordered basis only.

The analysis [35] of the similar shell-model problem for a heavy atom showed that the actual distribution of off-diagonal matrix elements \tilde{H}_{kl} is far from being Gaussian. It can be written in the form analogous to the Porter–Thomas distribution,

$$P_{\kappa}(\tilde{H}_{kl}) = \frac{1}{2} [(2\tilde{H})^{\kappa+1} \Gamma(\kappa + 1)]^{-1} |\tilde{H}_{kl}|^{\kappa} e^{-|\tilde{H}_{kl}|/2\tilde{H}} \quad (31)$$

where Γ stands for the Γ -function and κ is a numerical parameter. For the distribution (31) taken literally for all values of \tilde{H}_{kl} , the mean absolute value of \tilde{H}_{kl} is $2(\kappa + 1)\tilde{H}$. The power κ found in [35] is close to the Porter–Thomas value $\kappa_{PT} = -\frac{1}{2}$ (compare with Eq. (51) below). The distribution of matrix elements found in the shell-model calculations by Wambach [73] also agrees with (31). A similar distribution was found by Kusnezov [74] in the interacting boson model. Since our study reveals a very similar picture (see below), the conclusion is plausible that this class of distributions is generic for the many-body interactions in heavy atoms or nuclei.

Note that the Porter–Thomas distribution for the reduced widths γ of the resonances follows [7, 21] from the Gaussian distribution for the decay amplitudes A if the proportionality $\gamma \propto |A|^2$ is assumed. Therefore Eq. (31) implies that the normally distributed quantities in the realistic case are not the off-diagonal matrix elements themselves, as would be the case in canonical Gaussian random matrix ensembles but rather some quantities resembling square roots of them. The underlying physical reason might be related to presence of the dominating multipole–multipole forces. This is by construction the case in the interacting boson model. The Coulomb interaction in atoms is actually determined by a small number of multipoles. The specific role of the pairing

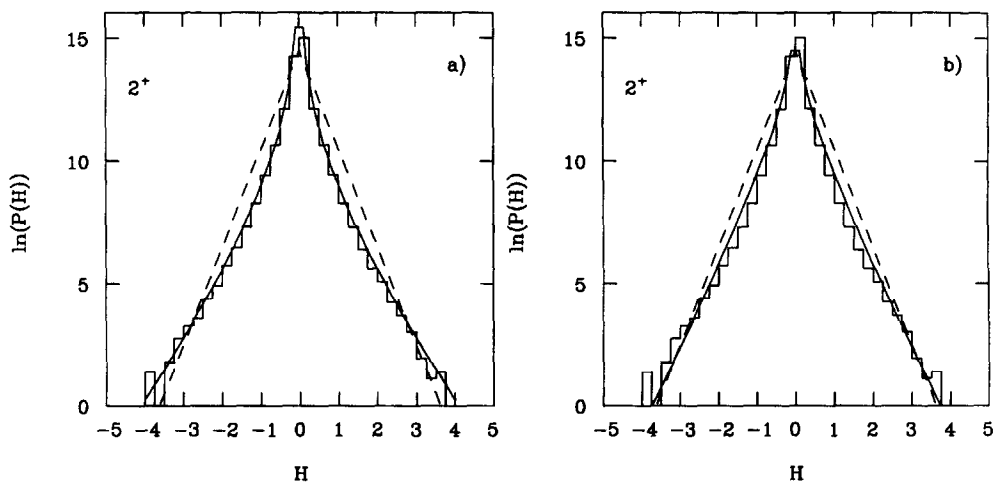


Fig. 9. (a) The distribution of off-diagonal matrix elements between the 2^+0 states (histogram), dashed line—pure exponential fit, Eq. (31) with $\kappa = 0$, solid line—fit with $\kappa = -2$; (b) the same with solid line as fit with $\kappa = -1$.

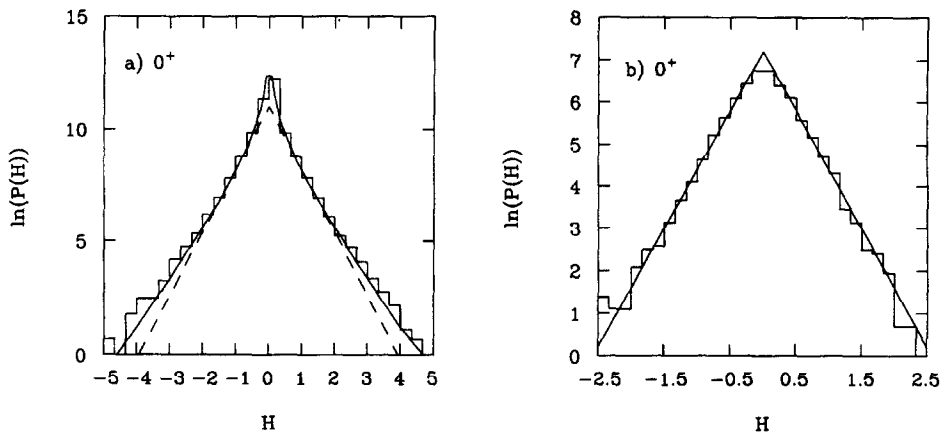


Fig. 10. The distribution of off-diagonal matrix elements between the 0^+0 states (histogram), pure exponential fit, Eq. (31) with $\kappa = 0$ (dashed line), fit with $\kappa = -1$ (solid line). Panel *a* takes into account all 0^+0 states, panel *b* is limited by the states of the largest partition.

and quadrupole interactions in nuclei is also well known. The case of the factorizable forces leading to the distribution of type (31) is outlined in Appendix A.

The distribution (31) diverges at small values of the matrix elements if $\kappa \leq -1$. In the actual analysis it is difficult to make a precise fit to this region. Fitting the rest of the histogram we allow all values of κ . The distribution function for 5.36×10^6 off-diagonal matrix elements between the 2^+0 states of the sd shell model is shown in Fig. 9. Except for the above-mentioned region around zero and extreme wings corresponding to the exceptionally big elements, the distribution is in good agreement with expression (31) for $\kappa = -2$, see panel *a*; this value gives a better fit than $\kappa = 0$ or $\kappa = -1$, panel *b*. The fit covers a change of matrix elements by four orders of magnitude. The fitted value of \tilde{H} is equal to 0.25 MeV. Under similar conditions, the off-diagonal matrix elements for the 0^+0 states, Fig. 10(a), agree with the distribution (31) at $\kappa = -1$ and $\tilde{H} = 0.27$ MeV.

For comparison, Fig. 10(b) shows the distribution of the matrix elements taken for the subset of 103 0^+0 states belonging to the largest partition. Here again we see the exponential fall of the probability but the preexponential factor is now absent, $\kappa \approx 0$. We can conclude that such a factor presumably comes from the weak transitions between partitions. The origin of the apparent difference in the preexponent factor for different classes of states is not clear at this point.

3. Level statistics

In this section we begin to present the analysis of our “empirical” data obtained via the diagonalization of the shell-model problem. The results of the exact solution for the Schrödinger equation with the fixed hamiltonian acting in the finite space are to be compared with the predictions of random matrix ensembles. This comparison is based upon an assumption of ergodicity. For sufficiently high dimensionality N , we expect that the eigenvalues and eigenfunctions taken from the different parts of the actual spectrum can be treated similar to different members of a statistical ensemble. This turns out to be the case locally, for small fragments of the

spectrum which still include a large number of levels. However, this hypothesis of self-averaging does not account for the secular behavior of physical quantities which depend smoothly on excitation energy in actual systems. Thus, low-lying shell-model states supposedly have a simpler structure than highly excited states with developed mixing. The increasing complexity reflects the stochastization of dynamics and represents one of the goals of our studies. This feature is absent in canonical random matrix ensembles where degree of complexity is uniform over the spectrum.

Another general issue to be considered is that the states in the model calculations suffer from the artificial truncation of mixing with states outside the model space. Such a distortion should influence mainly the highest states. Accordingly, the procedure can be twofold: either consider the entire set of all states available as a model for a system with finite Hilbert space [49], or cut off some part of high-lying states as an artifact of the model. The second option is the only one appropriate for comparing the model with actual experimental data. The procedure of unfolding [7], which locally rescales energies taking into account the secular behavior of the level density, can be a compromise between those two approaches. Unfolding is necessary if the local properties of different parts of the spectrum are superimposed in order to get rich statistics, as will be discussed below for the study of local level correlations and fluctuations. However the global properties of the finite shell model having no counterpart in realistic nuclear structure might be, in turn, of specific theoretical interest (see for example the study of the 3-level Lipkin model in [49]).

3.1. Level density

The simplest characteristic of the spectrum of the eigenvalues E_α is the total density $\rho(E)$ of states with given values of exact integrals of motion. In Section 2.4 we have introduced this function, Eq. (24), with its lowest moments, Eqs. (26) and (27). In our finite Hilbert space $\rho(E)$ vanishes at lower and upper boundaries of the spectrum, being maximum in the middle. As usual in the problems with the pure discrete spectrum, the original set of the δ -peaks $\sum_\alpha \delta(E - E_\alpha)$ converts into a continuous function $\rho(E)$ when averaged over several adjacent levels.

The behavior of $\rho(E)$ can be compared with the GOE predictions. By our normalization of the GOE correlators defined with the aid of the parameter a in (29), the trace $\text{Tr} \overline{H^2}$, which is equal to $\sum_\alpha E_\alpha^2$, increases linearly with N as $Na^2/4$ for large N . This shows immediately that a provides a scale for the whole energy range covered by the GOE spectrum. In fact, for $N \gg 1$ the GOE predicts the Wigner semicircle rule for the level density with the radius equal exactly to a ,

$$\rho(E) = N \frac{2}{\pi a^2} \sqrt{a^2 - E^2} \theta(a^2 - E^2) \quad (32)$$

where the normalization (24) was used.

Many ways exist to derive the semicircle rule (see for example [7]). One of the simplest versions calculates the average level density as an imaginary part of the average Green function $\overline{(E - H)^{-1}}$ in the limit of $N \rightarrow \infty$. Then the main diagrams are nonintersecting (rainbow), and their contribution is directly given by the correlator (29). The summation of this class of diagrams leads to the semicircle rule (32). Such a derivation shows that the validity of the semicircle rule is not limited to the pure GOE case. It is rather associated [7] with the domination of binary correlations in the limit of large N .

The BRM theory predicts, both numerically and analytically [71, 72], the semicircle level density for a sufficiently broad band. At $b \gg 1$ but $2b/N \ll 1$, the summation of the same class of diagrams for the average Green function leads to the semicircle level density with the compressed radius, $a \rightarrow r = a\sqrt{2b/N}$. Of course, it agrees with the direct estimate for the trace $\text{Tr} H^2$. Even in the presence of the nonrandom part H_0 which has a uniform level density of unperturbed states $\rho_0(\varepsilon) \simeq N/2a_0$, the random perturbation (30) leads to the semicircle-like average density of stationary states with

$$r \approx \sqrt{a_0^2 + (2b/N)a^2} \quad (33)$$

if the strength $a/N^{-1/2}$ is not small compared to the unperturbed level spacings. For the semicircle density with radius r , the energy dispersion defined by Eq. (27) is $\sigma_E^2 = r^2/4$. Therefore the BRM result (33) agrees with the exact result of statistical spectroscopy (27). The regular part a_0 from (33) is analogous to the contribution of the average diagonal field, Δ_E in Eq. (17); and quantities a in (33) and $\bar{\sigma}$ in (27) are related mostly to the off-diagonal interaction. For the 2^+0 states we obtain $a_0 \approx 16 \text{ MeV}$, $a \approx 56 \text{ MeV}$, $r \approx 26 \text{ MeV} = 2\sigma_E$.

On the other hand, we deal with a realistic hamiltonian (1) which has no random elements. We have already mentioned that, due to the two-body character of interaction and exact conservation of angular momentum, there is a noticeable number of vanishing matrix elements of H' in the truncated configuration space. All many-body matrix elements are determined by a rather small number of the two-body interaction matrix elements. What is even more important, the realistic interaction strongly mixes configurations but it is not strong enough to destroy completely the partition structure. In such cases, according to simple arguments given in [7], we should expect the level density $\rho(E)$ to be closer to the Gaussian shape than to the semicircle shape. The transition from Gaussian to semicircle level density occurs [75, 7] when many-body forces are introduced, lifting the selection rules for interactions between the partitions. One should mention also that the two-body matrix elements are the same for all classes of states with various J and T which can induce correlations between the classes.

Fig. 11 shows the cumulative level number

$$\mathcal{N}(E) = \int_{-\infty}^E dE' \rho(E') \quad (34)$$

for the $J^\pi T = 2^+0$ states. Fig. 11(b) and (d) corresponds to the absence of the off-diagonal mixing interaction \tilde{H} . The staircase pattern is determined by the partitions. Fig. 11(a) and (c) is obtained for the full hamiltonian. As a consequence of strong mixing, we see a more smooth behavior. The remaining irregularities at low excitation energy come partly from the weak remnants of the partition structure and partly from the pairing effects, Section 7. A similar picture is found for the 0^+0 states, Fig. 12. The resulting curves $\mathcal{N}(E)$ for different classes are clearly correlated.

The local level density $\rho(E)$ reveals fluctuations of various scales (“wavelengths” [7]) depending on the range of averaging. This can be seen in Fig. 13 where $\rho(E)$ for 0^+0 states was taken as the average inverse level spacing on a segment including 5 levels to the left and 5 levels to the right from a given energy E for the panel *a* and ± 20 levels for the panel *b*. In the second case the edge behavior is distorted by the large averaging range. Depicting the level densities for 0^+0 and 2^+0 states as histograms we can fit both of them, Figs. 14(b) and (c) respectively, by the Gaussians with

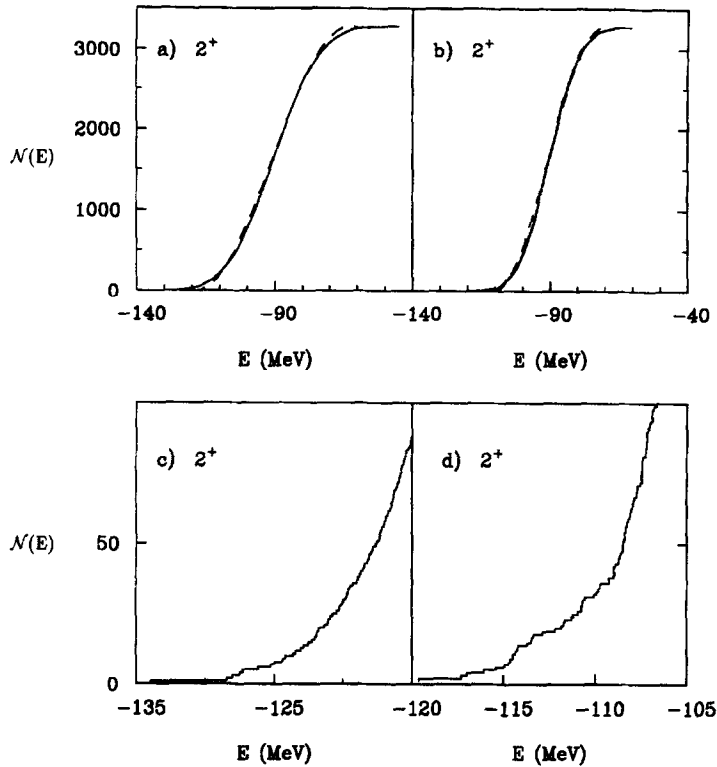


Fig. 11. The cumulative level number for the 2^+ states with no off-diagonal interaction \tilde{H} (b); the same for the full Hamiltonian (a), dashed line shows the fit according to Eq. (35). Expanded parts of (a) and (b) are shown in parts (c) and (d) respectively.

the same values of the centroid $E_0 = -90$ MeV and the dispersion $\sigma_E = 13$ MeV predicted by the simple consideration of Section 2.4. For comparison, Fig. 14(a) shows the density of the unperturbed energies H_{kk} of the 0^+ states. In this case with no off-diagonal interaction, the Gaussian shape of the level density with the dispersion $\Delta_E \approx 8$ MeV is entirely due to the combinatorial nature of the fermionic excitation spectrum. The origin of this shape is discussed in [7]. The level density $\rho(E)$ is very different from the semicircle, in agreement with what is expected for the two-body residual interaction [7].

Performing similar calculations in the p–n formalism, we get practically the same results for the level density of the superpositions of the states with different (all) isospins. This means that different isospin sectors have similar properties defined by a common two-body interaction. This point is illustrated in Fig. 15 by the level density for 1161 0^+ states in the valence system of 4 protons and 4 neutrons (${}^2_4\text{Mg}$). The histograms for $\rho(E)$ are identical, except for a shift as a whole, for both versions of the interaction, WPN (panel a) and WPNC (panel b). The Coulomb interaction present in the WPNC version mainly pushes up the entire set of levels.

To clarify the origin of the Gaussian level density in our case of the strong interaction, we have carried out several numerical experiments. As we discussed in Section 2.5, the actual distribution of the matrix elements is exponential with the preexponential power law. One can generate the

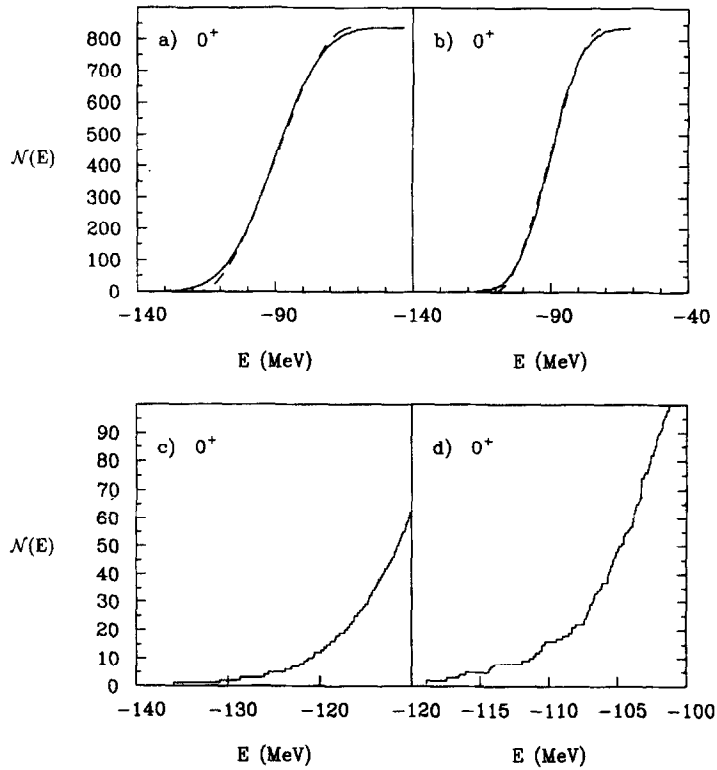


Fig. 12. The same as Fig. 11 for the 0^+0 states.

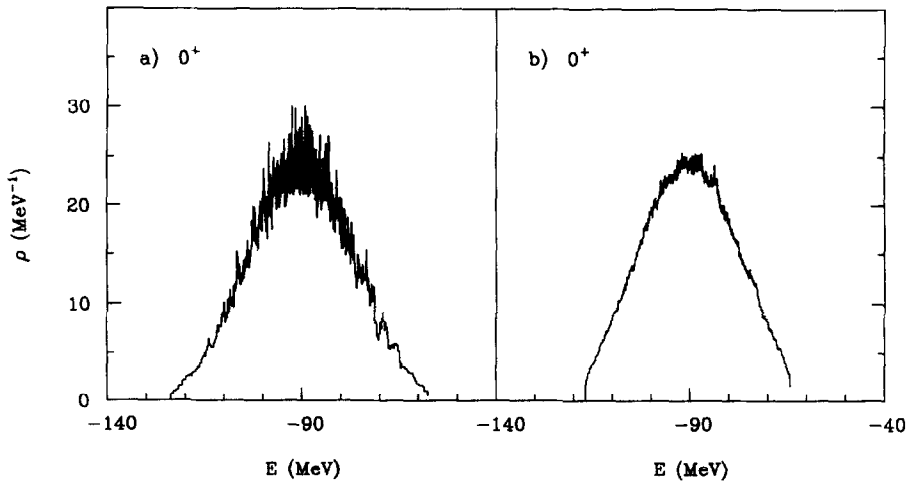


Fig. 13. Level density for the 0^+0 states averaged over ± 5 levels, panel a, and ± 20 levels, panel b.

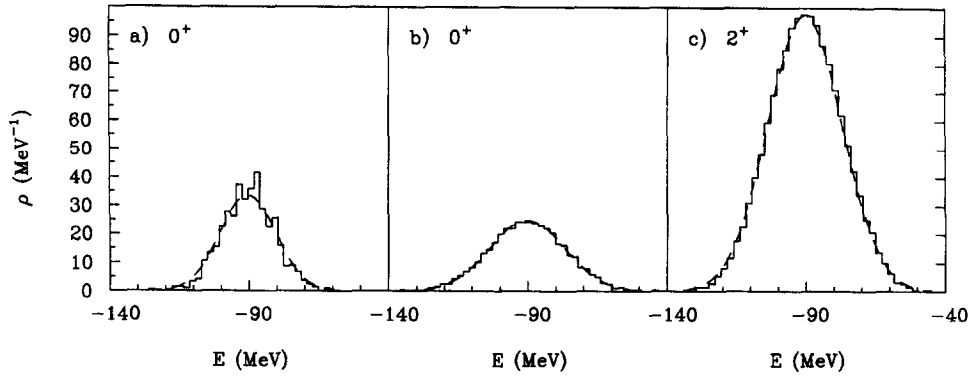


Fig. 14. Level densities for the 0^+0 (panel *a* corresponds to the absence of the off-diagonal residual interaction and panel *b* shows the result of the diagonalization of the full hamiltonian), and for the 2^+0 states, full solution (panel *c*). The results of calculations are shown by the histograms and Gaussian fits by the dashed lines.

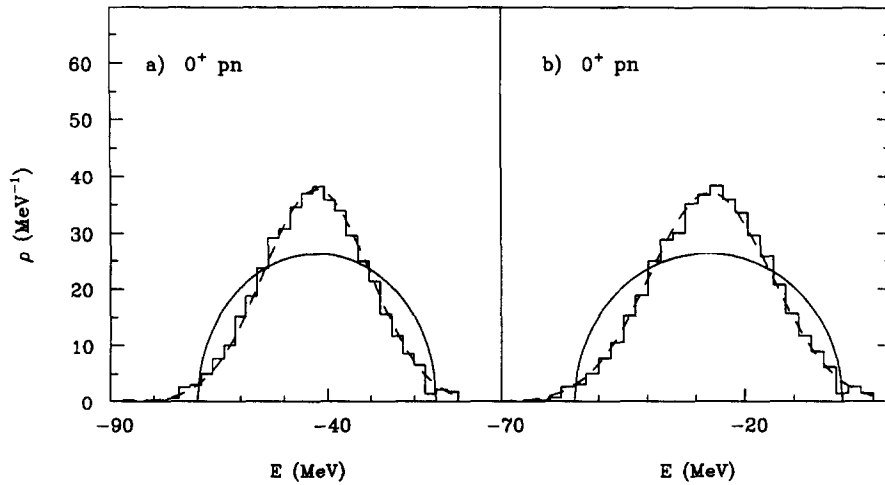


Fig. 15. Level densities for the 0^+0 states in the system of 4 valence protons and 4 valence neutrons (histograms) and the Gaussian fits (dashed lines); panels *a* and *b* correspond to the calculations in the p–n scheme with the isospin conserving Wildenthal interaction (WPN) and with the interaction (WPNC) of Ref. [67] including Coulomb and isospin-violating nuclear parts, respectively.

random matrix ensemble defined by such a distribution. We have to underline that here the many-body matrix elements are uncorrelated. For the dimension $N = 400$ and the matrix elements of the hamiltonian generated according to the distribution (31) with $\kappa = 0$ and random signs, the level density agrees with the semicircle law, Fig. 16.

For another numerical experiment we considered the single largest 0^+0 partition ($N = 103$). As seen from Fig. 17(a), using the same exponential distribution function (31) with random signs for the off-diagonal matrix elements and the actual diagonal matrix elements H_{kk} , the level density is already close to the semicircle structure. On the other hand, the largest partition level density in the

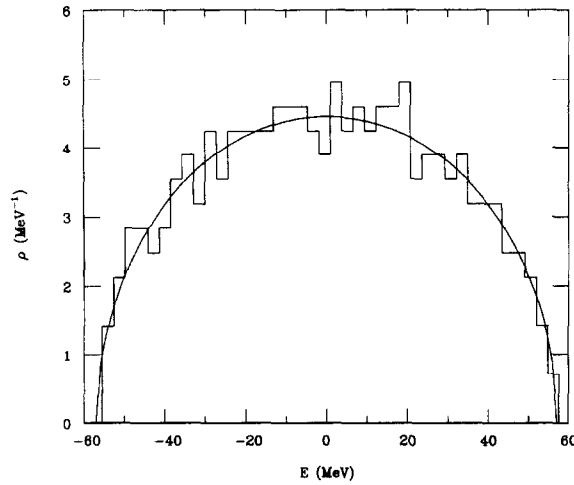


Fig. 16. Level density for the random matrix ensemble with the exponential distribution (31) of the off-diagonal matrix elements (histogram) and the semicircle fit (solid line). The Gaussian distribution with the $\sigma = 10$ MeV is assumed for the diagonal matrix elements.

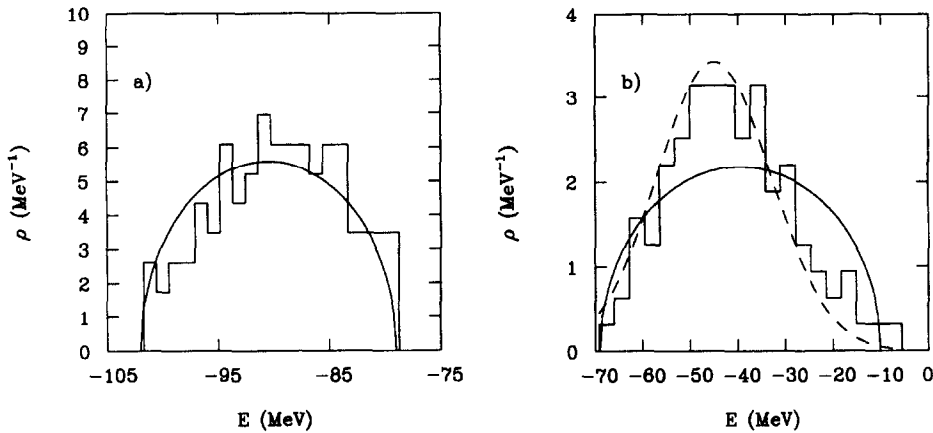


Fig. 17. Level densities for the largest partition, $N = 103$, of the 0^+0 states (histograms), semicircle fit (solid lines) and Gaussian fit (dashed line). Panel *a* corresponds to the off-diagonal matrix elements generated by the exponential distribution function (31) with random signs, and the diagonal matrix elements are taken from the Wildenthal interaction. Panel *b* gives the results of the diagonalization with the many-body matrix elements calculated from 63 two-body matrix elements taken randomly from the range $(-5, +5)$ MeV.

case of the two-body interaction given by 63 random matrix elements taken from the range between -5 and $+5$ MeV is much closer to the Gaussian, Fig. 17(b). The difference between the empirical Gaussian level density and the semicircle should be ascribed to the correlations within the many-body hamiltonian determined by a relatively small number of two-body matrix elements regardless of their regularity or randomness.

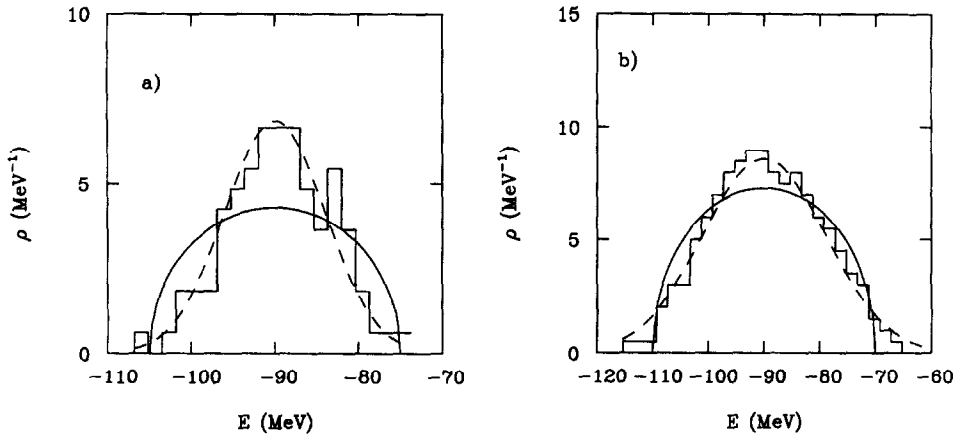


Fig. 18. Level densities for the 0^+0 states calculated with the actual interaction matrix elements (histograms), semicircle fit (solid lines) and Gaussian fit (dashed lines) for the largest partition, $N = 103$, panel a, and for the three largest partitions, $N = 237$, panel b.

The development of the full Gaussian level density can be illustrated by Fig. 18. Fig. 18(a) shows the results of the diagonalization using the actual interaction matrix elements for the largest 0^+0 partition. Fig. 18(b) gives the results for the truncation to the three largest partitions $N = 237$. The mixing between the partitions gradually broadens the curve. The Gaussian variance is $\sigma_E = 9$ MeV in Fig. 18(a) and increases to 11.5 MeV in Fig. 18(b). Similar values for σ_E can be derived by the direct averaging of the off-diagonal matrix elements according to Eq. (27).

It is worth mentioning that the difference between Gaussian and semicircle level densities can at least partly be removed by a procedure similar to unfolding, used routinely in the analysis of local level statistics. Namely, using the “natural” smooth scale of cumulative level number $\mathcal{N}(E)$, Eq. (34), instead of energy E itself, we obtain (Fig. 19) the level density $\rho(\mathcal{N})$ much closer to the semicircle shape. It is easy to see that the cumulative level number written as

$$\mathcal{N}(E) = \frac{N}{2} \left[1 + \sin \frac{\pi(E - E_0)}{2a_c} \right] \quad (35)$$

would precisely correspond to the semicircle level density in the \mathcal{N} -scale

$$\rho(\mathcal{N}) = \frac{\pi}{2a_c} \sqrt{\left(\frac{N}{2}\right)^2 - \left(\mathcal{N} - \frac{N}{2}\right)^2}. \quad (36)$$

The dashed lines in Figs. 11(a) and 12(a) show that Eq. (35) with $a_c = 28$ MeV describes well the cumulative level number for both classes of states, 0^+0 and 2^+0 , except for the edges. The effective semicircle level density with the same variance of energy as in the Gaussian fit of Fig. 11 would have a radius $r = 2\sigma_E = 26$ MeV which is close to the value of a_c . Below we use both the energy and \mathcal{N} -scales (the latter called also α -scale) on equal footing for various quantities remembering that the Gaussian-like behavior in the first scale corresponds to the semicircle-like in the second one.

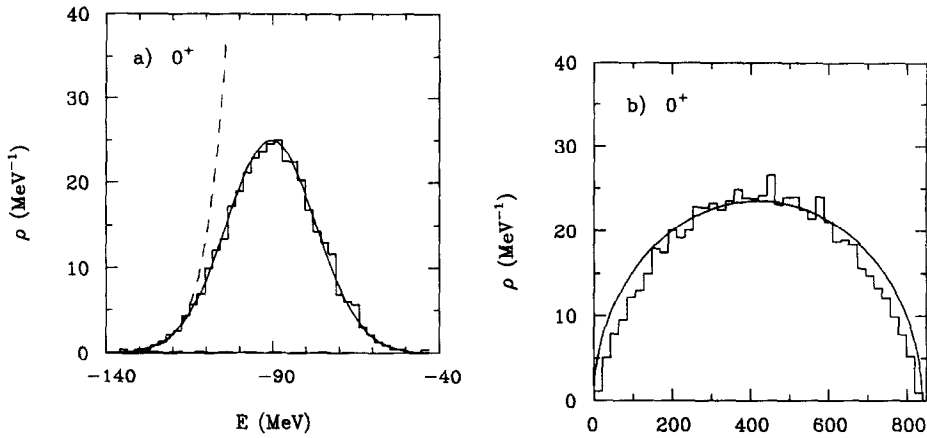


Fig. 19. Level densities from the full calculation for the 0^+0 states with actual interaction matrix elements in function of energy, panel *a*, and in function of cumulative level number \mathcal{N} , panel *b* (histograms). The solid lines correspond to Gaussian (panel *a*) and semicircle (panel *b*) fits, respectively; dashed line on panel *a* gives the Fermi-gas level density, Eq. (37).

The initial part of the spectrum agrees also with the Fermi-gas level density [62, 21],

$$\rho_J(E) = \frac{a_0^{3/4} b_0^{3/2}}{\sqrt{48\pi}} \frac{2J+1}{\tilde{E}_J^{7/4}} \exp(2\sqrt{a_0 \tilde{E}_J}), \quad (37)$$

see the dashed line in Fig. 19(a) which corresponds to values of $a_0 = 1.4 \text{ MeV}^{-1}$, $b_0 = 0.24 \text{ MeV}$ both for the 0^+0 and 2^+0 states. As well known, the parameters of the model are related to the single-particle level density at the Fermi surface g_0 (in our notations $a_0 = (\pi^2/6)g_0$) and to the effective statistical moment of inertia, $b_0 = \hbar/2I_{\text{eff}}$ which determines the thermal excitation energy $\tilde{E}_J = E - b_0 J(J+1)$. The level density parameter a_0 is smaller than the Fermi gas estimate $a_0 \approx (\pi^2/4)(A/\varepsilon_F) \approx (A/14) \text{ MeV}^{-1}$. This difference may reflect the presence of single-particle orbitals of both parities in the Fermi gas model. In our sd shell-model space the average single-particle angular momentum projection is $\langle m^2 \rangle \approx 2$. This would result in $b_0 = \pi^2/(12a_0 \langle m^2 \rangle) \approx 0.2 \text{ MeV}$ with $a_0 = 2 \text{ MeV}^{-1}$ and $b_0 = 0.3 \text{ MeV}$ with the empirical value of a_0 . The conventional statistical assumption of random coupling of angular momenta implied in the derivation of (37) agrees qualitatively with our arguments of “geometrical chaoticity”, Section 2. For high excitation energy the whole Fermi-gas approach breaks down due to limitations of the finite Hilbert space.

3.2. Level spacing distribution

The degeneracies caused by the shell structure in the spherical mean field are lifted by the residual interaction. In the stochastic limit, the mixing by the off-diagonal hamiltonian leads to the level repulsion and to a more uniform level spacing distribution. It results in the nearest level spacing distribution close to the Wigner surmise:

$$P_W(s) = \frac{1}{2} \pi s e^{-(\pi/4)s^2}. \quad (38)$$

The linear repulsion and Gaussian tail in Eq. (38) are the distinctive features of chaotic level statistics in contrast to the Poisson distribution of random events

$$P_P(s) = e^{-s} . \quad (39)$$

which is characteristic for integrable systems. Here $s = (E_{\alpha+1} - E_{\alpha})/\bar{D} \equiv \mathcal{E}_{\alpha+1} - \mathcal{E}_{\alpha}$ is the nearest neighbor spacing in units of the local average spacing \bar{D} . This rescaling, or unfolding [7], $E_{\alpha} \rightarrow \mathcal{E}_{\alpha}$, is important to separate local level correlations from the global secular behavior. All the results discussed below were obtained by the procedure of unfolding using the relevant average local level density.

Fig. 20 shows the nearest level spacing distribution $P(s)$ for 0^+ states calculated for the degenerate case (for the single-particle energies $e_{\lambda} = 0$), Fig. 20(a) and for the realistic e_{λ} , Fig. 20(b). The intermediate situations with the realistic single-particle spectrum e_{λ} and a residual interaction which is gradually turned on are shown in Figs. 21(a)–(c), which correspond to the relative intensity of the off-diagonal matrix elements \tilde{H}_{kl} equal to $\lambda = 0.0, 0.1$ and 0.2 , respectively. In Fig. 20 the chaotic behavior is in qualitative agreement with the Wigner distribution (38), especially for the degenerate case. With the realistic single-particle energies, onset of chaos is delayed, with respect to increasing λ , by persistence of the shell-model structure. The noninteracting case of Fig. 21(a) reveals the Poisson-like distribution. However, the transition to the Wigner distribution occurs already at a relatively weak strength of the interaction, about 0.2 of the realistic value. The level spacing distribution is universal as can be seen from Fig. 22 for the 2^+ states.

An important factor for establishing the Wigner level spacing distribution is the interpartition interaction. Diagonalization within the single largest partition alone both for 0^+ states, Fig. 23(a) and for 2^+ states, Fig. 23(c), results in a level spacing distribution with an excess of small and large spacings which is still far from the Wigner level spacing. Qualitative features of the Wigner distribution appear only after the diagonalization is performed in the model space of the three largest partitions, Fig. 23(b) for the 0^+ states.

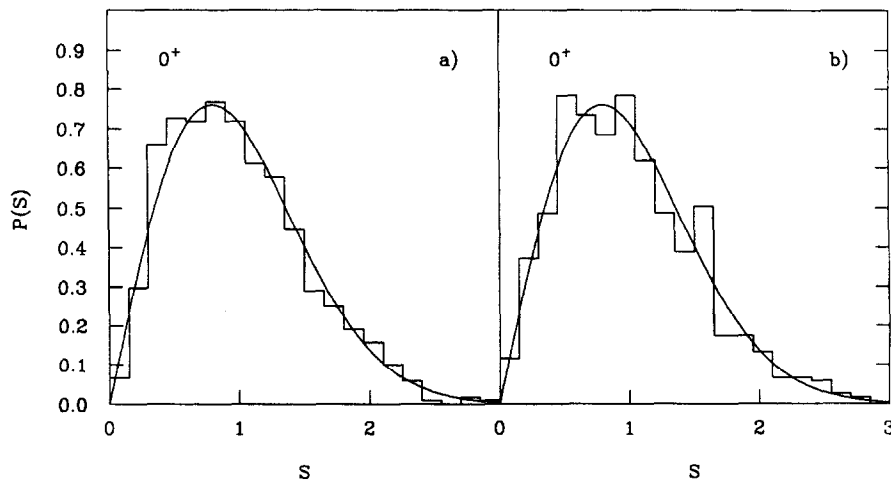


Fig. 20. Nearest level spacing distribution (histograms) and Wigner surmise, Eq. (38), (solid lines) for the 0^+ states in the system with degenerate single-particle orbitals (a) and in the realistic case (b).

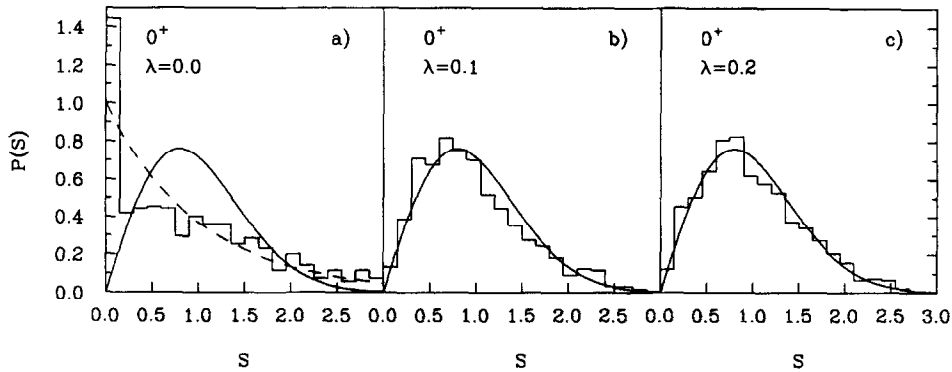


Fig. 21. Nearest level spacing distribution (histograms) compared to the Wigner surmise (solid lines) and the Poisson distribution for the 0^+0 states at different interaction strength, $\lambda = 0, 0.1, 0.2$ (panels *a, b, c*, respectively).

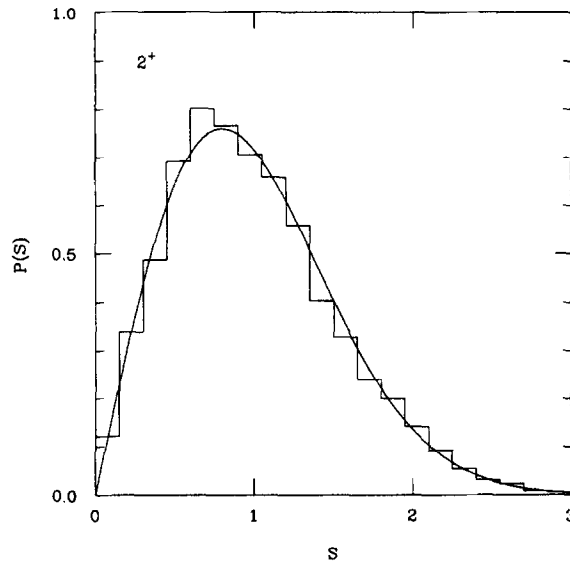


Fig. 22. Nearest level spacing distribution (histogram) and Wigner surmise (solid line) for the 2^+0 states.

In consideration of the nearest level spacing distribution, the proton–neutron formalism gives results distinctly different from those for the single isospin states. This is expected [7] for the case of a superposition of spectra belonging to nonoverlapping sectors of Hilbert space. The histogram of Fig. 24, computed in the p – n formalism for the 0^+0 states of the 4 proton + 4 neutron system, reveals the nearest level spacing distribution intermediate between the Wigner and Poisson functions due to the absence of mixing and repulsion between levels with different isospin. As shown first in [76], the superposition of independent level sequences quickly gives rise to the Poisson limit. The picture is qualitatively similar for both versions of the interactions, panels *a* (WPN) and *b* (WPNC). However, panel *b* is closer to the Wigner limit giving reduced values of $P(s)$ at small s .

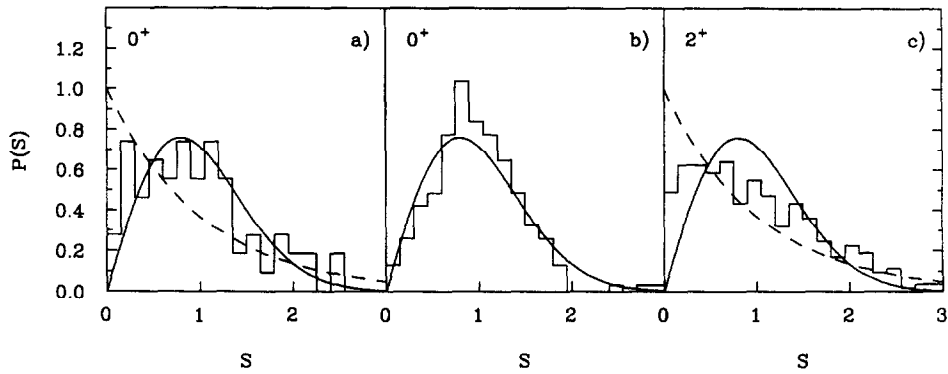


Fig. 23. Nearest level spacing distribution (histogram), Wigner surmise (solid line) and Poisson distribution (dashed line) for the diagonalization within the largest partition ($N = 103$) of the 0^+0 states (a) and within space of three largest partitions (b). Panel c presents the same results for the largest partition ($N = 390$) of the 2^+0 states.

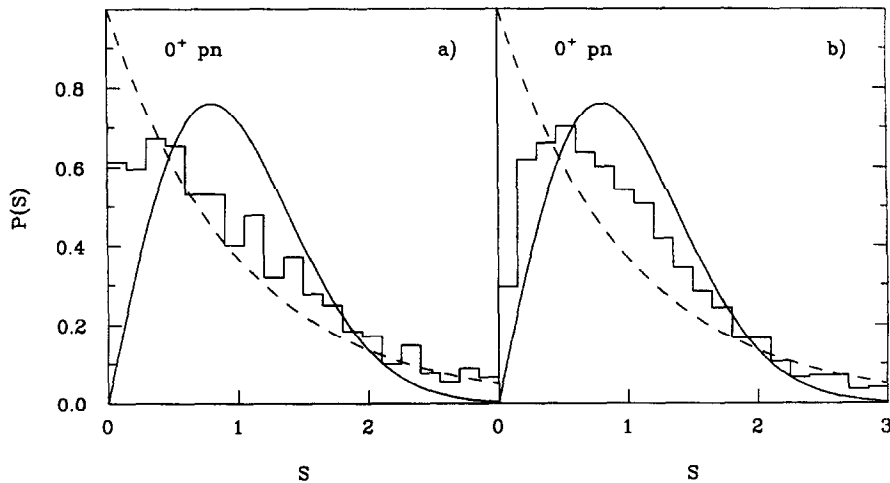


Fig. 24. Nearest level spacing distributions for the 0^+0 states ($N = 1161$) in the ^{24}Mg (4 valence protons and 4 valence neutrons): results of diagonalization in the p–n formalism (histograms), Wigner surmise (solid lines), Poisson distribution (dashed lines) for the WPN interaction (a) and for the WPNC interaction (b).

3.3. Level repulsion at small spacings

An interesting unresolved theoretical problem is related to the precise form of the level repulsion law at small distances s . The GOE, eq. (38), and regular dynamics, Eq. (39), predict the behavior $P(s) \propto s^\beta$, $s \rightarrow 0$, with $\beta = 1$ and $\beta = 0$, respectively. The repulsion becomes stronger for the Gaussian unitary and Gaussian symplectic ensembles ($\beta = 2$ and $\beta = 4$, respectively).

In the pure independent particle shell model with no residual interaction, the level spacings are quantized according to the single-particle excitation spectrum (3). Including the diagonal part \bar{H} of the residual interaction we come to the case of the integrable dynamics. Here the adjacent states are

not mixed and one expects the random (Poisson) distribution (39) of the nearest level spacing. There is no consistent theory explaining how the Poisson level spacing (39) evolves into the Wigner distribution (38) as the stochastization occurs and levels repel each other. Based on the estimates of the regular and chaotic volume fractions of the classical phase space, the Berry–Robnik theory [22] predicts $P(s = 0) = \text{const}$. The value of this constant is supposed to go from 1, Eq. (39), to 0 as the dynamics become more and more chaotic.

In contrast to the Berry–Robnik theory, a recent study [77] of a large number of levels in a chaotic billiard shows that in the transitional region between regular and chaotic dynamics the small spacing behavior agrees with the fractional power law $P(s) \sim s^\beta$, $0 < \beta < 1$. Various interpolation formulae with the power law were suggested [7, 5] and used with variable success. The parameter β is supposed to change from 0 (Poisson distribution) to 1 (Wigner distribution) in parallel to the onset of chaos. The correlation of this parameter with the degree of localization of wave functions was pointed out in [5].

The fractional power repulsion is seemingly in contradiction with the simple perturbation theory. Assuming that in the limit of $s \rightarrow 0$ it is sufficient to consider the mixing of the two nearest neighbors, one can use the standard expression for the level spacing

$$s = \sqrt{(H_{11} - H_{22})^2 + 4|H_{12}|^2} \quad (40)$$

in terms of the interaction matrix elements. When applied to the time-reversal invariant case, the mixing matrix element H_{12} is real so that $s \rightarrow 0$ requires that two quantities $x = H_{11} - H_{22}$ and $y = 2H_{12}$ go to zero simultaneously. For a uniform measure in the xy -plane this leads to the linear repulsion. If the mixing interaction has matrix elements of the order $y \sim y_0$, one expects the linear repulsion at spacings $s \leq y_0$. According to this way of reasoning, the Poisson distribution (39) is valid in the completely integrable case only. Any perturbation destroying the integrals of motion gives rise to a region of linear repulsion which has a size proportional to the magnitude of the perturbation.

Here one can mention that an interesting scenario takes place in the case when a chaotic system with the Wigner level spacing distribution is allowed to decay [32, 78]. Interaction with the continuum creates the repulsion of complex energies $E - (i/2)\Gamma$. On the real energy axis (E) the nearest neighbor behavior can be approximated [78], similar to the Berry–Robnik conjecture, by the superposition of the Wigner (38) and Gaussian distributions with finite $P(0)$ depending on the ratio Γ/D of the decay width to the level spacing in the closed system. In an open system with small widths Γ of isolated resonances, interaction with the continuum removes [32] the linear repulsion at the spacings $s \simeq \Gamma$.

The perturbative arguments do not take into account that, as a rule rather than the exception, there is an accumulation of small mixing matrix elements which destroys the uniformity in the xy -plane. In the semiclassical domain it can occur if the classical phase space should consist of separated parts. The possibility of degeneracies between the states localized in different areas would lead to the Poisson distribution of level spacings (39). However, the quantum tunneling restores the communication between those areas. The corresponding matrix elements are concentrated at small values of y . As we discussed in Section 2.6, the relative abundance of small off-diagonal matrix elements seems to be a generic feature of realistic many-body systems even with no tunneling effects.

The mechanism for the emergence of fractional power level repulsion becomes clear already in the two-level model (40). Considering x and y as random variables with the distribution function $p(x, y)$ we have

$$P(s) = \int dx dy p(x, y) \delta(s - \sqrt{x^2 + y^2}) = s \int d\theta p(s \cos \theta, s \sin \theta). \quad (41)$$

For a function $p(x, y)$ which is regular near the origin, Eq. (41) gives the linear repulsion at small s . However, for the empirical distribution of the type $P_\kappa(y)$, Eq. (31), and assuming that the smooth dependence on the diagonal elements x introduces only a constant factor, one obtains $P(s) \propto s^{\kappa+1}$. Thus, the Porter–Thomas distribution of the off-diagonal matrix elements, $\kappa = -\frac{1}{2}$, leads to the fractional power repulsion with $\beta = \frac{1}{2}$. In contrast to that, the depressed probability of small matrix elements as in (A14) at $q > 2$ would result in a stronger repulsion than in the Wigner distribution. This enhanced repulsion can mimic the transition to the unitary or symplectic ensembles.

It is not clear to what extent the naive two-level estimates resembles the actual small distance behavior. As an example one can take the case [79] of the simplest ensemble of 3×3 random matrices with the Gaussian distribution of all matrix elements except for $H_{13} = H_{31}$ which is kept equal to zero. This singular feature gives rise to the nearest level spacing distribution $P(s) \sim s \ln(1/s)$ at small s . Logarithmic behavior was also found [80] when the tail of exponentially small mixing matrix elements $y \sim \exp(-t/t_0)$ is present; as might be the case, for example, due to the tunneling between classically forbidden regions. This can be understood in the two-level model, assuming that the range t of tunneling is uniformly distributed up to $t \approx N$. Then the probability density $p(0, y)$ and the resulting $P(s)$ can be estimated as

$$p(0, y) \propto \int_0^N dt \delta(y - y_0 e^{-t/t_0}) = \frac{t_0}{y}, \quad e^{-N/t_0} < \frac{y}{y_0} < 1, \quad (42)$$

$$P(s) \sim P(0) + \ln s. \quad (43)$$

This estimate is expected to be valid for small s which are still larger than the smallest tunneling matrix elements $y_0 \exp(-N/t_0)$.

To study the region of $s \ll 1$ with high precision, one needs statistics much better than we have currently at our disposal. It can be achieved combining properly the data for different classes of states. Below we present the first results in this direction. Fig. 25 shows the magnified nearest level spacing distribution in the region $s < 0.2$ which shows no deviations from linear repulsion at the realistic interaction strength.

The whole question of transition from Poisson to Wigner level spacing distribution is far from being solved.

3.4. Spectral rigidity

It is known [7, 81] that chaotic dynamics lead to rather rigid spectra. The level repulsion creates a sequence of levels which “crystallize”; they have fluctuations which are strongly suppressed in comparison with a pure random sequence. The mechanism of crystallization and its relation to the semiclassical theory of periodic orbits was elucidated by Berry [82]. As an appropriate quantitative

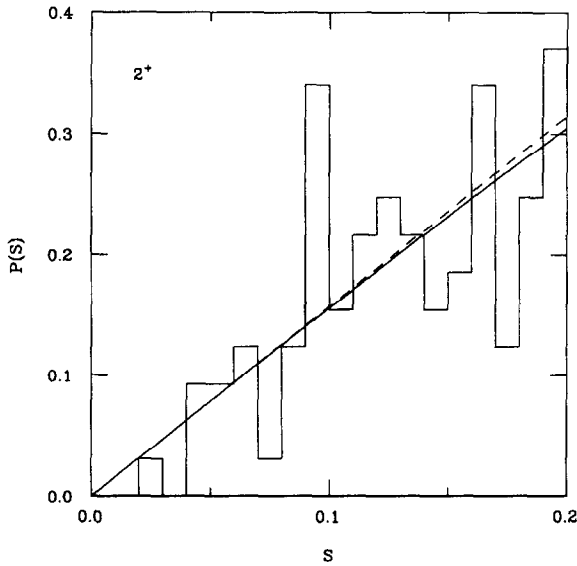


Fig. 25. Nearest level spacing distribution in the region of small $s \leq 0.2$ (histogram), linear fit $P(s) = \text{const} \times s$ (dashed line) and the Wigner surmise (solid line).

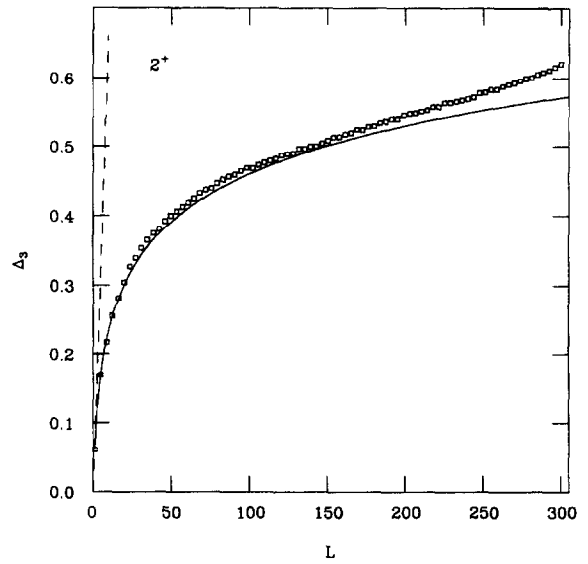


Fig. 26. The spectral rigidity $\Delta(L)$ for the 2^+0 states, squares (calculations) and solid line (the GOE prediction).

measure, the spectral rigidity $\Delta(L)$ is conventionally used,

$$\Delta(L) = \left\langle \min_{A,B} \int_x^{x+L} \frac{d\mathcal{E}}{L} [\mathcal{N}(\mathcal{E}) - A\mathcal{E} - B]^2 \right\rangle_x. \quad (44)$$

Here the average is taken of integral deviations of the cumulative unfolded level number $\mathcal{N}(E)$ from the best linear fit over various (overlapped) segments of length L .

For regular dynamics, and therefore a random level sequence with the Poisson nearest level spacing distribution (39), the deviation grows linearly, $\Delta(L) = L/15$. For the chaotic case and Wigner nearest level spacing distribution (38), the spectra are rigid. Starting at small L with the same linear behavior as in the regular case, the deviation only grows logarithmically at $L \gg 1$,

$$\Delta(L) \approx (1/\pi^2) \ln L - 0.007. \quad (45)$$

As follows from the analysis by Berry [82], in the semiclassical limit $\Delta(L)$ is expected to saturate at a nonuniversal value of $L \simeq L_{\max} \simeq 2\pi\hbar/t_{\min}D$ determined by the shortest periodic orbits with a period t_{\min} . The number L_{\max} measures the Weisskopf recurrence time of a wave packet, $2\pi\hbar/D$, in units of the shortest period which provides a natural scale. At large $L > L_{\max}$ one expects pseudooscillatory behavior with constant $\Delta(L)$. If the period t_{\min} is related to the major shell structure with a typical energy interval $\delta\varepsilon \sim 10$ MeV, the Berry estimate would give $L_{\max} \simeq \delta\varepsilon/D \simeq 300$ for the 2^+0 states.

Using the large matrix of the 2^+0 states we can trace the behavior of $\Delta(L)$ up to very large L . Previous to this study the largest value of L considered was about 100 [10, 52]. The results shown in Fig. 26 display an agreement with the GOE prediction with no evidence of saturation up to $L \simeq 150$.

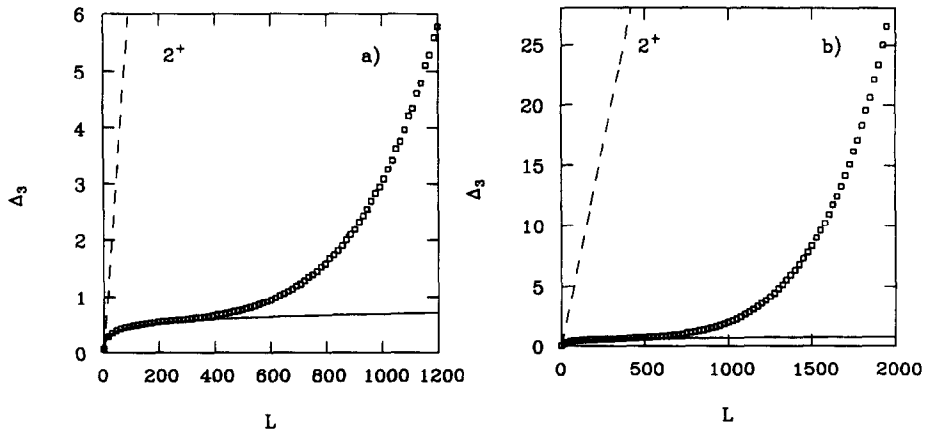


Fig. 27. The spectral rigidity $\Delta(L)$ for the 2^+ states in the limit of large L , $L \leq 1200$ (panel a) and $L \leq 2000$ (panel b); squares (calculations) and solid line (the GOE prediction).

At higher L , the spectral rigidity decreases revealing the upbend from the GOE curve. Such behavior is known in “one-body chaos” (anisotropic Kepler problem [83], Sinai billiard [84] or the experiment with a superconducting stadium billiard [10]) where the deviations start at much smaller L . According to Mottelson’s conjecture [85], the remnants of regular behavior determine dynamics at times too short to resolve the signatures of chaos. It was shown explicitly that for the stadium billiard [10] the effect is due to the contribution of the marginally stable “bouncing ball” orbits. In [84] the upbend point L_d was associated with the inverse Lyapunov exponents which give the time scale for the development of classical chaos. The upbend of the curve $\Delta(L)$, Fig. 27(a), starting at $L \approx 200$ corresponds to the energy interval $\delta\epsilon \approx 7$ MeV. Remarkably, this behavior lasts (Fig. 27(b)) up to the highest values of $L \approx 2000$ attainable for our computations.

In many-body dynamics within one major shell, the available regular energy parameters are the single-particle level spacings $\delta\epsilon \approx 3$ to 7 MeV which would give $L_d \approx 100$ to 200. One could also think of the “scars” in the partition space related to the quasiperiodic motion induced by the most coherent two-body matrix elements. This role can be played by pairing which will be discussed in Section 7. The reversible transfer of a pair between the subshells generates such motion which is destroyed after some time by incoherent parts of the interaction. The corresponding energy scale is rather low, $\delta\epsilon \approx 4$ –5 MeV. In this case one would expect the saturation of the spectral rigidity at $L_d \approx 100$ to 150.

On the other hand, the inverse lifetime of the simple configurations can be estimated by the fragmentation width of Eq. (20), $\bar{\sigma} \approx 10$ MeV. The initial simple configuration $|k\rangle$ evolves in time governed by the total hamiltonian H . The evolution can be described by the survival amplitude

$$A_k(t) \equiv \langle k(t) | k \rangle = \langle k | e^{iHt} | k \rangle \quad (46)$$

which is the Fourier transform of the strength function (14). At small times the decrease of the absolute value of A_k is given by the energy uncertainty of the basis state $|k\rangle$ which is nothing but

the energy dispersion (19),

$$|A_k(t)| \approx 1 - \frac{t^2}{2} [\langle k|H^2|k\rangle - \bar{E}_k^2] \approx e^{-t^2\sigma_k^2/2}. \quad (47)$$

One can argue that at times shorter than $t_d \simeq \sqrt{2}/\bar{\sigma}$ the chaotic component of the evolution is still of minor importance. It would lead to the upbend of the spectral rigidity at $L_d \simeq \bar{\sigma}/\sqrt{2D} \simeq 200$ which approximately agrees with the observation.

Let us note however that the time interval t_d cannot in general be identified with the inverse Lyapunov exponent. In contrast to the exponential decay, the survival amplitude, due to the hermiticity of the hamiltonian, decreases as a Gaussian function. To have an exponential decay at short times, one needs the Lorentzian wings of the strength function and, hence, an infinite second moment of the energy distribution. The decrease (47) takes place even in the case of regular dynamics if the initial state is not an eigenstate of the hamiltonian.

Another plausible explanation of the upbend can be associated with the range of the interaction between the simple configurations. We measured this range by the parameter ω_k , Eq. (28) which determines the effective band width ~ 7.5 MeV and the corresponding value of L_d between 200 and 250. At shorter time intervals, the band boundaries are not resolved so that motion in the configuration space is analogous to that in the full GOE matrix. The more detailed study of the influence of various parameters is necessary in order to pin down definitively the mechanism responsible for the deviation of the spectral rigidity from the GOE behavior.

To illustrate the role of hidden integrals of motion in the level rigidity, we again give an example of calculations in the p–n formalism. Fig. 28 shows $\Delta(L)$ for the 0^+0 states (dimension 1161) in the system of 4 protons and 4 neutrons. Here we do not discriminate the states by isospin. As a result, the level rigidity is intermediate between the GOE and Poisson predictions. Comparison of panels a and b shows stability of the conclusions with respect to slight modifications of the residual

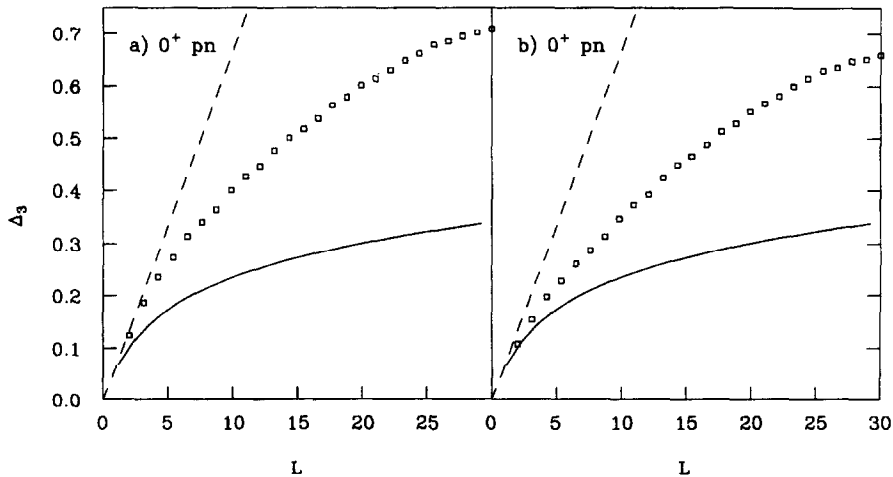


Fig. 28. The spectral rigidity $\Delta(L)$ for the 0^+0 states in the system of 4 valence protons and 4 valence neutrons calculated in the p–n formalism with the WPN interaction (a) and the WPNC interaction (b); squares (calculations), solid line (the GOE prediction) and dashed line (Poisson level distribution).

interaction. The small fraction of the isospin violating forces slightly shifts the resulting curve in the GOE direction.

3.5. Level dynamics

Classical chaotic trajectories are unstable with respect to variations of initial conditions [1, 2]. The straightforward analogy with classical chaos would lead to the expectation of strong sensitivity of chaotic quantum spectra to small changes of the hamiltonian parameters. There have been many suggestions of quantifying this sensitivity [3, 4]. The actual situation in the initial stage of the stochastization process (measured by the evolution of the parameters from the regular to the chaotic region) is determined by the level dynamics (for the introduction into the subject see [3] and references therein). Multiple avoided crossings [86–88] create on average a rigid “crystalline” structure. Once this structure is formed, the pattern is stabilized so that the rate of crossing decreases at larger values of the hamiltonian parameter.

Each individual pairwise level crossing is similar to a particle collision in a gas. It can be described by the level velocities (slopes $v_\alpha = dE_\alpha/d\lambda$), the distance of the closest approach (crossing gap [88]), the range of the forces (the correlation function of levels $\langle E_\alpha(0)E_\alpha(\lambda) \rangle$ [89]), and the scattering angle (the level curvature $K_\alpha = d^2E_\alpha/d\lambda^2$ [90, 91]). Here λ is a variable parameter in the hamiltonian.

The distribution functions of the crossing parameters for the canonical Gaussian ensembles can be found exactly [88, 91, 92]. As an example, we discuss here the level curvature distribution $P_c(k)$ which is predicted in the limit of $N \rightarrow \infty$ as

$$P_c(k) = \frac{\Gamma(1 + \beta/2)}{\sqrt{\pi}\Gamma((1 + \beta)/2)} (1 + k^2)^{-(2+\beta)/2} \quad (48)$$

with the standard identification of $\beta = 1, 2, 4$ for Gaussian orthogonal, unitary and symplectic ensembles, respectively.

To compare with our data, first the level energies are unfolded, $E_\alpha(\lambda) \rightarrow \mathcal{E}_\alpha(\lambda)$, to get rid of secular behavior (the “collective flow” of the bundle of levels). Then the actual curvatures K_α of unfolded eigenvalues $\mathcal{E}_\alpha(\lambda)$ are rescaled so that the dimensionless curvature $k = K/(\pi\bar{\rho}\langle v^2 \rangle)$ eliminates the local variations of the slopes v .

The rigidity of the chaotic spectrum results in the fact that the most probable curvatures are small. Moreover, contrary to expectations, the probability of finding a large curvature $k \gg 1$ is smaller in the chaotic case than for regular dynamics ($\beta = 0$) when the close level collisions, which are very sensitive to the changes of parameters, are more frequent. The limiting behavior at large k in (48), $P_c(k) \propto k^{-(2+\beta)}$, directly follows from the power law $P(s) \sim s^\beta$ for the nearest level repulsion in the Gaussian ensembles, see for example (38) for $\beta = 1$. Indeed, the asymptotics of large k presumably correspond to a pairwise interaction of two levels when the influence of remote levels is negligible. Then the curvature is determined by the small energy denominator, and the distribution of the level spacings s is translated into the curvature distribution, $P_c(k \gg 1) \rightsquigarrow P(s = 1/k)/k^2$. The fractional power level repulsion $\sim s^\beta$, Section 3.2, would give the asymptotics $P_c(k) \sim 1/k^{2+\beta}$ with $0 < \beta < 1$. In all cases with $\beta \leq 1$, the decrease of $P_c(k)$ is rather slow so that the second moment of the distribution diverges, logarithmically for the GOE.

The natural parameter λ in our shell-model calculations is the strength of the residual interaction changing from 0 to 1. We already saw in Figs. 11 and 12 how the global level density reacts to switching on the interaction. Fig. 29(a) shows a total spectrum of 326 0^+0 states for 8 valence particles (^{24}Mg nucleus) as a function of λ (in percent) taken as a common factor in front of the interaction hamiltonian H' . Fig. 29(b) shows the same set of levels on an unfolded number scale, and a magnified fragment containing about 30 levels in the middle of the spectrum is shown in Fig. 29(c). The avoided crossings, being very frequent at $\lambda \leq 0.4$, become more rare at larger λ . As was discussed in [91], as λ increases, the level gas with finite N is expanding. This general expansion is clearly seen in Fig. 29(a). It goes approximately linearly with λ . In this region the increase of λ mainly rescales the energies rather than mixing the states.

In Fig. 30 we display the empirical curvature distribution for 50 central unfolded levels \mathcal{E}_α , $\alpha = 138$ to 188. To get more statistics, the data for the intervals $\Delta\lambda = 0.2$ are grouped together. At small $\lambda < 0.2$ there is an excess of small and a deficit of larger curvatures. The small k behavior is determined mostly by a presence of gaps in the irregular Poisson-like chain of levels in a weakly interacting system. A purely random sequence of levels with a weak random interaction would generate a singularity $\sim 1/\sqrt{k}$ at small k . However, the range $\lambda = 0.2$ to 0.4 gives good agreement

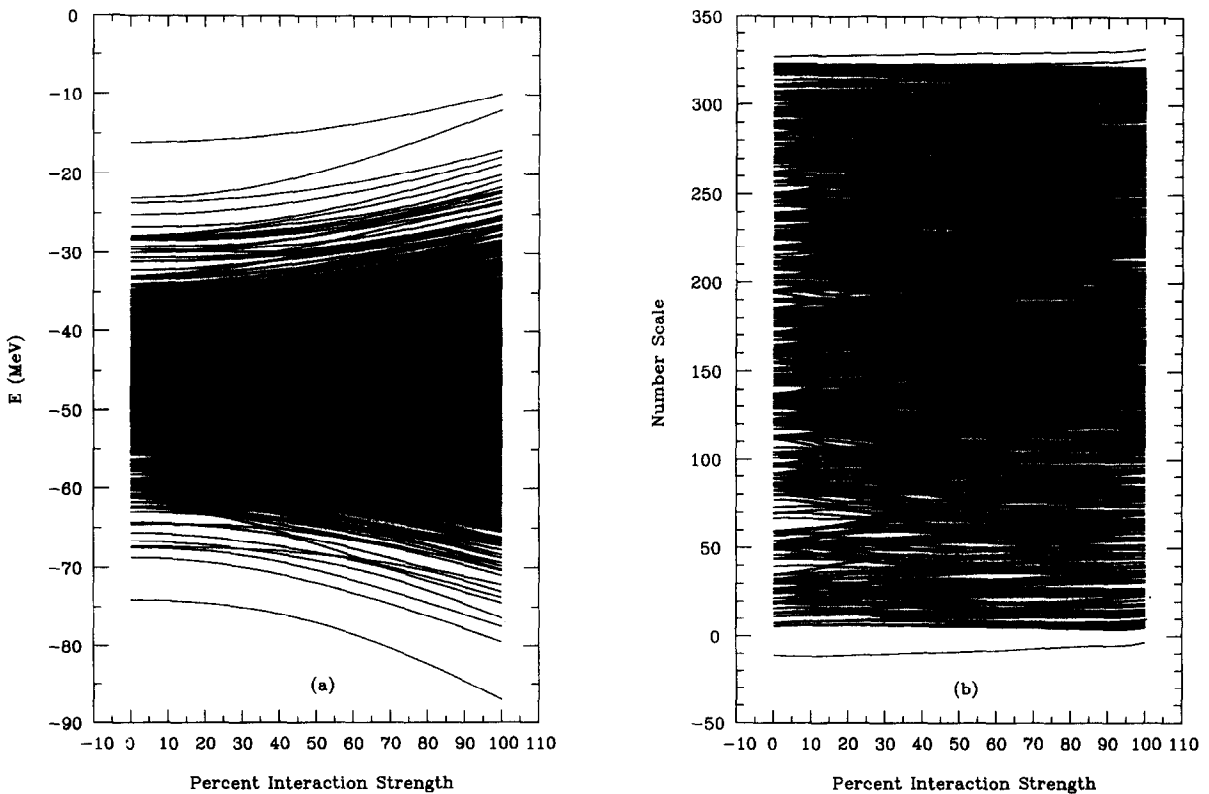


Fig. 29. The level spectrum of the 0^+0 states for 8 valence particles, panel a, the same spectrum after unfolding, panel b, and the fragment of the middle part of the unfolded spectrum, panel c.

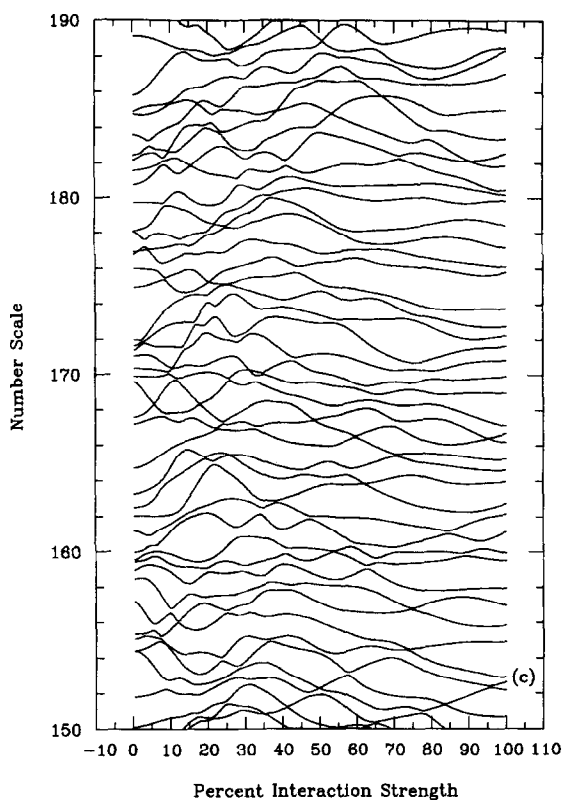


Fig. 29. Continued.

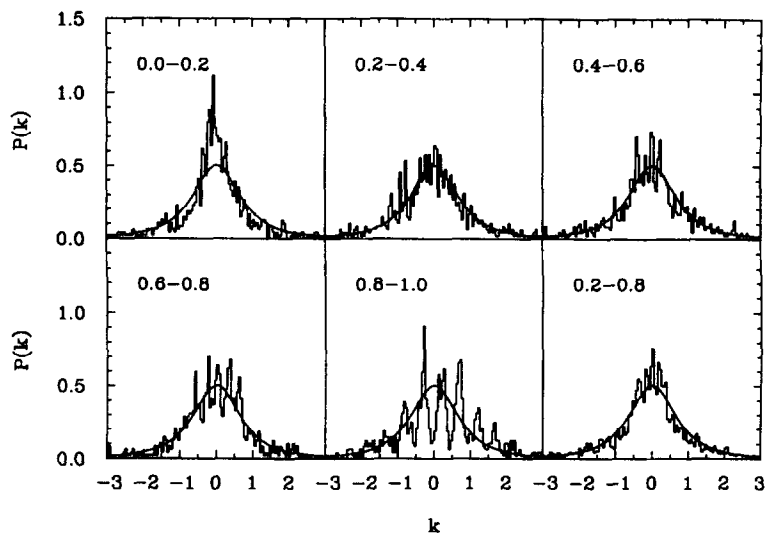


Fig. 30. The level curvature distribution in the unfolded spectrum; the histograms correspond to calculations for 50 middle levels $\alpha = 138$ to 188 of Fig. 29 for various ranges of λ . The solid line gives the GOE prediction, Eq. (48) with $\beta = 1$.

with the GOE result (48), $\beta = 1$. This is the same value of strength which manifests the onset of chaos in the nearest level spacing distribution, Section 3.2. A further increase of λ signals the gas expansion regime which is getting more pronounced at larger λ .

The work studying other correlation functions for the shell-model eigenvalues and eigenvectors is in progress and will be reported elsewhere [93].

4. Complexity of wave functions

4.1. Distribution of components

In the random matrix ensembles, amplitudes C_k^α of eigenstates (5) become random variables. Distribution functions for these amplitudes are known for canonical Gaussian ensembles [94, 7]. The GOE case corresponds to complete delocalization, that is when all N components C_k^α for various k contribute equiprobably to the total normalization (6), and all N eigenfunctions $|\alpha\rangle$ have the same distribution of components. We are interested in the limit $N \gg 1$ when the individual amplitudes are normally distributed with $\bar{C} = 0$ and $\overline{C^2} = 1/N$ so that the exact GOE distribution function

$$P_{\text{comp}}(C) = \frac{\Gamma(N/2)}{\sqrt{\pi}\Gamma[(N-1)/2]} (1 - C^2)^{(N-3)/2} \theta(1 - C^2) \quad (49)$$

reduces to the Gaussian distribution

$$P_{\text{comp}}(C) = (N/2\pi)^{1/2} \exp\left(-\frac{N}{2} C^2\right). \quad (50)$$

Weights $W = C^2$ of the components in the limit (50) obey the Porter–Thomas distribution

$$P_w(W) = (N/2\pi)^{1/2} \frac{1}{\sqrt{W}} \exp\left(-\frac{N}{2} W\right). \quad (51)$$

The same amplitudes C_k^α describe the fragmentation of the simple state $|k\rangle$ over exact eigenstates $|\alpha\rangle$.

Due to the orthonormalization (6), the amplitudes in the GOE are slightly correlated [94, 7]. Thus, in the limit $N \gg 1$

$$\overline{W_k^\alpha W_l^\beta} = (1/N^2)(1 + 2\delta^{\alpha\beta}\delta_{kl}), \quad (52)$$

$$\frac{\overline{W_k^\alpha W_l^\alpha}}{(\overline{W_k^\alpha})(\overline{W_l^\alpha})} - 1 = -\frac{2}{N}, \quad k \neq l, \quad (53)$$

whereas the similar correlation function of weights for unrelated components, $\alpha \neq \beta, k \neq l$, is $2/N^2$.

According to the pattern of a gradual transition from regular to stochastic dynamics, one should expect the number N_α of principal components of the stationary wave function $|\alpha\rangle$ to increase along with excitation energy towards the limit of complete delocalization. In a given energy range,

$E \approx E_\alpha$, the distribution of components C_k^α presumably is similar to the Gaussian one, Eq. (50), but with the local width $\overline{(C_k^\alpha)^2} = 1/N_\alpha$,

$$P^\alpha(C^\alpha) = (N_\alpha/2\pi)^{1/2} \exp\left[-\frac{N_\alpha}{2}(C^\alpha)^2\right]. \quad (54)$$

This hypothesis was successfully utilized in statistical spectroscopy [53, 54] of nuclear levels even for relatively low-lying states as long as $N_\alpha \gg 1$. A similar assumption is used in the semiclassical theory [95], where the wave functions $\psi^\alpha(q)$ in configuration space are used instead of our Hilbert space representation (5) in terms of amplitudes C_k^α . In this case N_α is substituted by the area \mathcal{A}_α of the classical configuration space at energy E_α . The importance of using the projected states, with good exact quantum numbers instead of the m -scheme determinants, in studying the amplitude distribution was stressed in [51].

Using (54) and approximating sums by integrals over C extended to infinity, we can evaluate local ensemble averages by

$$\sum_k F(C_k^\alpha) \rightsquigarrow N_\alpha \int_{-\infty}^{\infty} dC F(C) P^\alpha(C). \quad (55)$$

This approximation is justified for large N_α when the contribution to the integral from the unphysical region of $C > 1$ is negligible.

4.2. Information entropy

Postponing the analysis of the distribution of the components of eigenvectors to Section 5, we introduce here the integral measures of complexity which characterize each eigenfunction as a whole. As mentioned in the Introduction, in contrast to the invariant signatures associated with the eigenvalues, we need to fix a representation in order to study the increasing degree of complexity of the eigenvectors. Using the mean field (in our case shell model) basis of H_0 we can try to quantify the complexity emerging from complete diagonalization [96]. The basis dependence provides an additional physical insight as we show below.

Information entropy [97, 98, 5, 40] seems to be a suitable candidate for measuring the degree of complexity of individual wave functions. It can be defined for a given normalized function $|\alpha\rangle$, and expanded as in Eq. (5) with the aid of a given basis $|k\rangle$, in terms of the weights (13) of the components,

$$S^\alpha = - \sum_k W_k^\alpha \ln W_k^\alpha. \quad (56)$$

Being dependent on the choice of the reference basis $|k\rangle$, this quantity reflects a complicated mutual relationship between the eigenbasis and the basis of representation. The entropy of eigenstates in their own eigenbasis, $W_k^\alpha \rightarrow \delta_k^\alpha$, vanishes. The formal maximum of the functional (56) corresponds to the “microcanonical” distribution with equal weights, $W_k^\alpha = \text{const} = N^{-1}$. In that case $S^\alpha = \text{const} = \ln N$. But the orthogonality conditions do not allow a significant fraction of the states to reach this limit.

In the local Gaussian approximation (54), the weights fluctuate around $(N_\alpha)^{-1}$ which implies [5] that the average over the ensemble value of entropy is smaller than the “microcanonical” value:

$$\overline{S^\alpha} = \ln(0.48N_\alpha) + \mathcal{O}(1/N_\alpha). \quad (57)$$

This result can be easily derived with the aid of (54) and (55),

$$\overline{S^\alpha} \rightsquigarrow -2 \sqrt{\frac{2N_\alpha}{\pi}} N_\alpha \int_0^\infty dC C^2 \ln C \exp\left(-\frac{N_\alpha}{2} C^2\right). \quad (58)$$

After the change of variable $x = \sqrt{N_\alpha/2}C$, one obtains

$$\overline{S^\alpha} = \ln\left(\xi \frac{N_\alpha}{2}\right) \quad (59)$$

where ξ does not depend on N_α ,

$$\xi = \exp\left(-\frac{8}{\sqrt{\pi}} \int_0^\infty x^2 \ln x e^{-x^2} dx\right) = 4e^{C-2} = 0.964 \quad (60)$$

where $C = 0.577$ is the Euler constant. This coincides with (57) being in perfect agreement with calculations for the GOE [5] where the results are uniform over the spectrum, $N_\alpha \rightarrow N$.

The entropy S^α (56), or the corresponding length in Hilbert space

$$l_S^\alpha = \exp S^\alpha, \quad (61)$$

characterizes the degree of delocalization of a given eigenfunction $|\alpha\rangle$ with respect to an original basis. The deviation of l_S^α from the GOE limit $0.48N$ indicates the incomplete mixing of basis states. For a similar purpose one can use [98] the moments of the distribution of amplitudes,

$$M_n^\alpha = \sum_k (W_k^\alpha)^n, \quad (62)$$

which are also related to the number of principal components of a given eigenstate. The zeroth moment is equal to the size N of the matrix, and the first moment follows from normalization, $M_1^\alpha \equiv 1$. The second moment (“participation index”) M_2^α determines the average $\overline{W^2}$; in the microcanonical case it coincides with the inverse number $1/N^\alpha$, whereas the Gaussian average, see Eqs. (52) or (55), gives $3/N^\alpha$. For higher moments in those two cases one has $M_n^\alpha = 1/(N^\alpha)^{n-1}$ and $M_n^\alpha = (2n-1)!/(N^\alpha)^{n-1}$, respectively. The entropy (56) (or l_S^α) emphasizes the small components of the eigenfunctions, whereas the higher moments (62) emphasize the larger components – they are all average measures of delocalization.

Fig. 31 shows the calculated information lengths l_S^α for all 839 states 0^+0 ordered on the energy scale. We see, Fig. 31(a), the same qualitative behavior as that of the level density $\rho(E)$ shown in Fig. 14. The transformation to the “natural” α -scale, Fig. 31(b), is also very similar to what was observed for $\rho(\mathcal{N})$, Fig. 19. This comparison shows the strong correlation between our information entropy and conventional thermodynamic entropy $\sim \ln \rho$ defined by the level density, see below (Section 6). Note that in the most chaotic (middle) part of the spectrum the information entropy does not yet reach the GOE value (57) with $N_\alpha = N$ which would give $l_S^\alpha = 0.482N = 404$ in the 0^+0 case. The entropy of the most “chaotic” states is about 90% of that in the GOE. The same situation

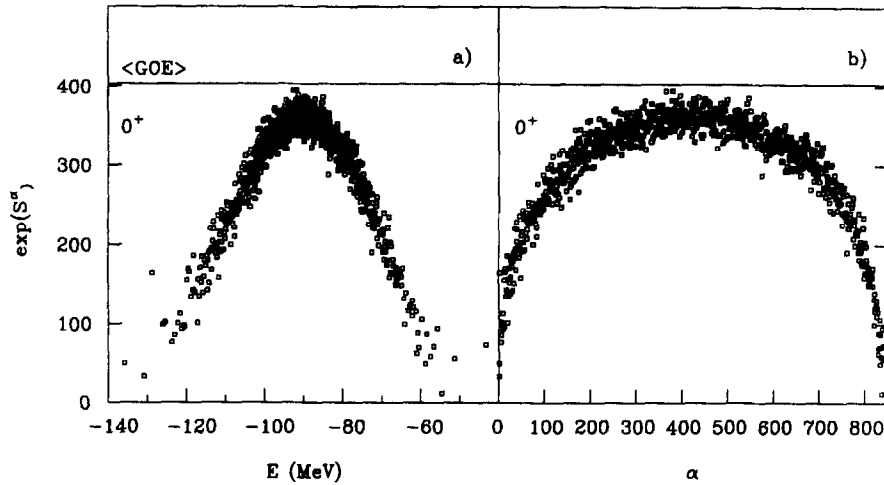


Fig. 31. Information length, Eq. (61), of the 0^+0 states as a function of energy (a) and in the α -scale (b). The horizontal solid line corresponds to the GOE value 404.

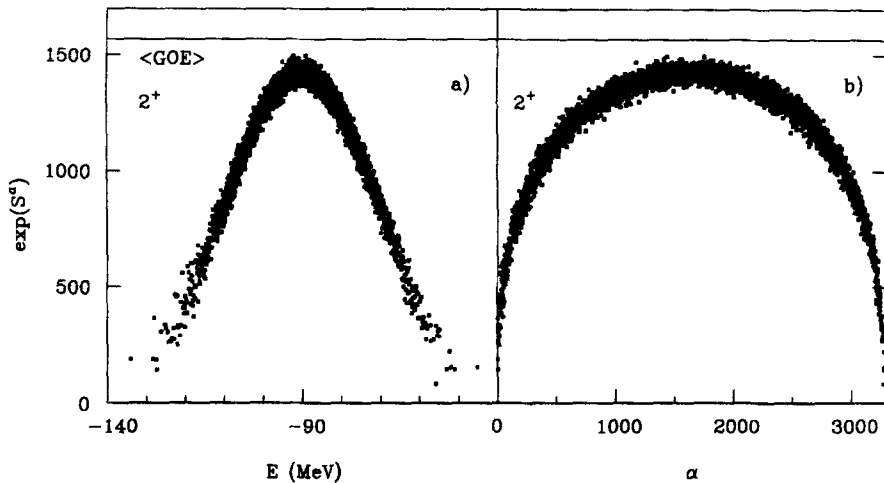


Fig. 32. The same as Fig. 31 for 2^+0 states, the GOE value is 1578.

is observed for 3276 states 2^+0 , Fig. 32. The fluctuations are weaker compared to the 0^+0 case due to the increased statistics. In both cases, the regular behavior of information entropy allows one to consider this quantity as a function of the excitation energy and, therefore, as a thermodynamic variable. However, if one goes to the case of degenerate single-particle orbitals by artificially setting to zero the single-particle energies e_λ , the chaotic limit is reached for a significant portion of 0^+0 and 2^+0 (Fig. 33) states. In this case information entropy ceases to be sensitive to the spectral evolution.

The distribution function of the information length l_S is shown with the help of histograms in Fig. 34. For the set of all 2^+0 eigenstates, Fig. 34(a), the distribution of l_S has a maximum at the

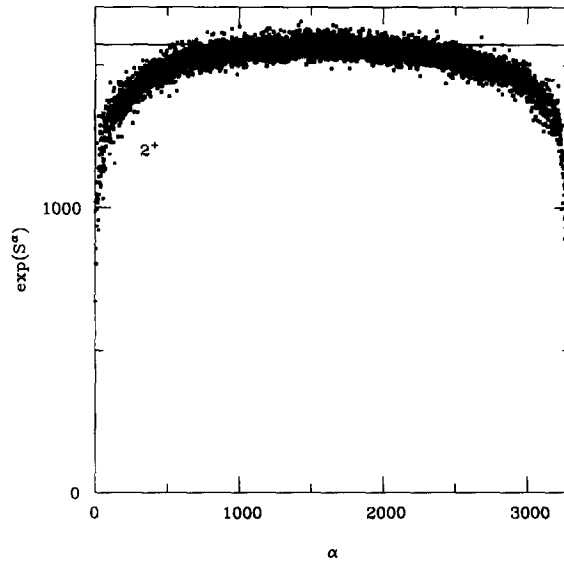


Fig. 33. Information length for the 2^+0 states for the degenerate model of single-particle orbitals.

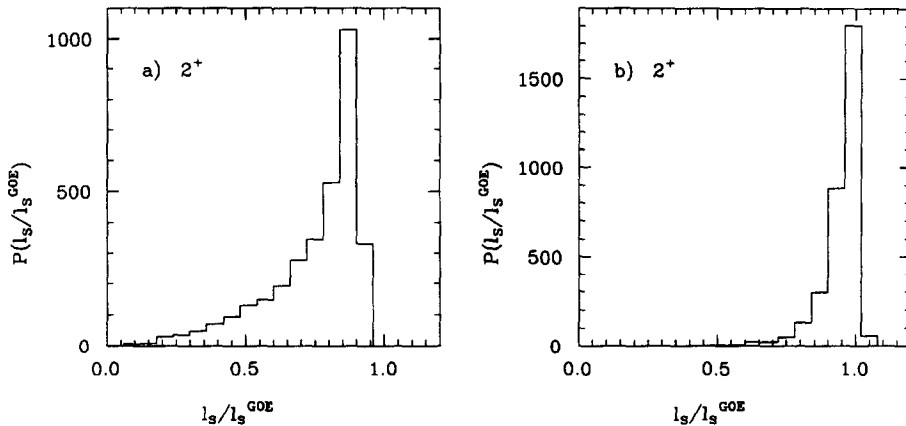


Fig. 34. The distribution function of the information length, Eq. (61), for all 2^+0 states calculated with actual Hamiltonian (a) and for 1600 2^+0 states in the middle of the spectrum calculated with the degenerate single-particle orbitals.

localization length which is less than the GOE value. A noticeable tail corresponds to the more localized states. For 1600 states 2^+0 in the middle of the spectrum calculated in the degenerate model, Fig. 34(b), the centroid of the obtained distribution is still shifted to the values less than unity, although the tail is strongly suppressed.

It is of some interest to see how information entropy is gradually accumulated as the coupling between the partitions is turned on. Solving the diagonalization problem exactly in the truncated space of the largest 0^+0 partition ($N = 103$) with the realistic interaction gives, Fig. 35(a), the

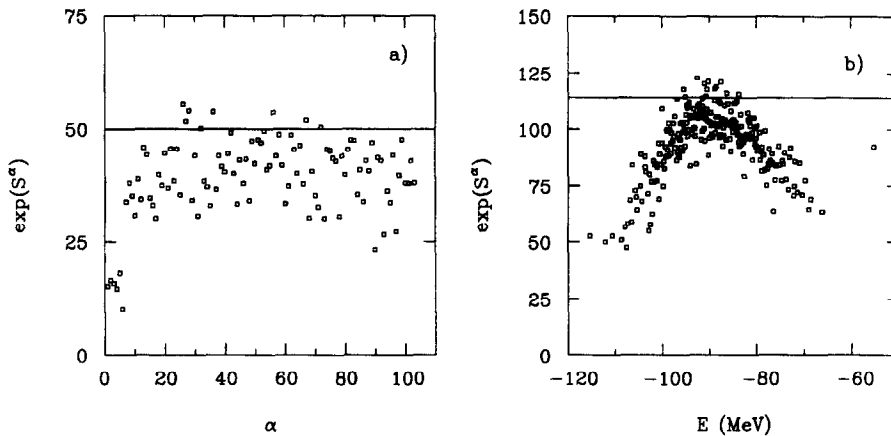


Fig. 35. Information length of the 0^+0 states calculated within the truncated largest partition (a) and within space of three largest partitions (b); the GOE values (solid lines) are 50 and 114, respectively.

localization length l_3^2 close to but lower than GOE limit of 50. The mixing is rather uniform within the one-partition space and statistical fluctuations are large because of the low dimension. Only the 6 lowest states have small information entropy, supposedly due to the approximate conservation of the integrals of motion like seniority. The uniformity of complexity is a consequence of the degeneracy of the basis states within the partition. The interaction is too strong on the scale of narrow splitting due to the diagonal matrix elements \bar{H}_{kk} . A similar situation will be discussed in Section 6.4, in connection with thermalization.

The typical pattern of the regular bell-shape behavior of information entropy is formed due to the interpartition interaction, which takes place on the background of the nondegenerate single-particle orbitals. The initial stage of the formation process is seen (on an energy scale) in Fig. 35(b) where information entropy is calculated for the space including the three largest partitions of total dimension $N = 237$. It corresponds to the GOE limit of 114 which is reached in the middle. It is clear that the intrapartition interaction does not support any selection rules except for those related to the two-body character of the hamiltonian. The two-body forces govern the coupling between the partitions and give rise to the observed regularities.

Information entropy behaves similarly in different isospin sectors. This can be seen from Fig. 36 where it is presented for the 0^+0 states of ^{24}Mg in the p–n formalism. Here the GOE value of the entropy is 560. To clarify this picture, the dimensions of the classes of states with various isospins are shown in Table 3, along with the absolute energies of the lowest states in every class. Regardless of the computational procedure, the eigenstates have a certain isospin. However, their information entropies are calculated in the p–n basis where the basis states are mixed in isospin. Therefore the GOE limit refers to the total dimension of $N = 1161$, rather than to the partial dimensions of the 0^+T classes. Fig. 36(a) allows one to distinguish the families of the states belonging to different isobaric classes by following the sequences starting at the corresponding threshold energies of Table 3. A small number of the 0^+4 states with the highest possible isospin have rather different structure, and therefore their mixing in the basis p–n states is comparatively weak. The results are not sensitive to slight variations of the residual interaction (Fig. 36(a) for the WPN case and

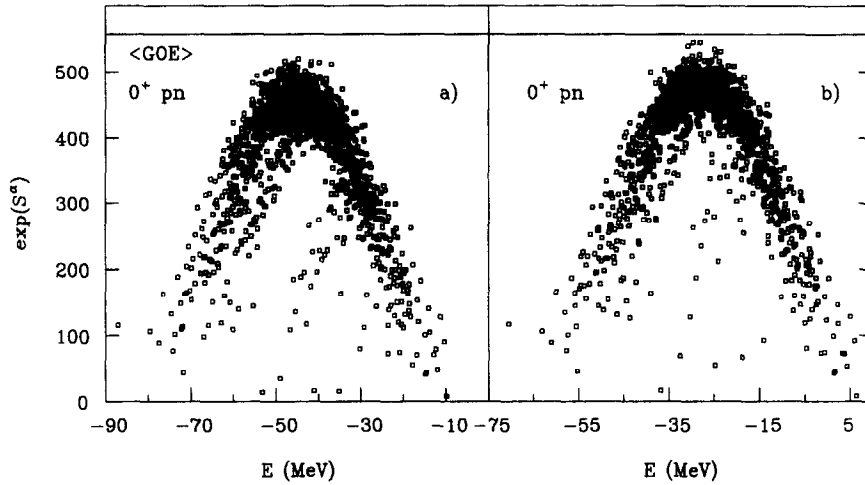


Fig. 36. Information length of the 0^+0 states for a system of 4 valence protons and 4 valence neutrons calculated in the p–n formalism with the WPN interaction (a), and the WPNC interaction (b); the solid line corresponds to the GOE value.

Table 3

Dimensions $N(T)$ and the lowest energies $E_{\min}(T)$ of the 0^+0 states for a system of 4 protons and 4 neutrons; calculations are carried out in the p–n formalism with the WPN interaction

T	Dim	$E_{\min}(T)$
0	325	– 87.09
1	482	– 77.55
2	287	– 71.66
3	59	– 54.56
4	9	– 41.05

Fig. 36(b) for the WPNC case), although the admixture of isospin violating forces in Fig. 36(b) slightly smears the isobaric families.

The overall suppression of the interaction strength changes the results drastically. The onset of chaos in the local level statistics occurred at a relatively weak interaction strength, Section 3.2. The information entropy of the 0^+0 states is shown in Fig. 37 at $\lambda = 0.4$ (this is the common factor in all off-diagonal residual interaction matrix elements as used in Section 2.4). We still see the regular evolution of information entropy as a function of energy but the localization length is strongly diminished roughly in proportionality to λ . We will return to this question in discussing the spreading width, Section 5.2.

Finally, we would like to show that the behavior of information entropy found in the above example is generic, and that the resulting pattern is qualitatively the same in quite different model spaces. Fig. 38 shows the information entropy for $N = 1183$ 0^+0 states in ^{12}C . The calculations were performed in a model space of the first four harmonic oscillator major shells, taking into

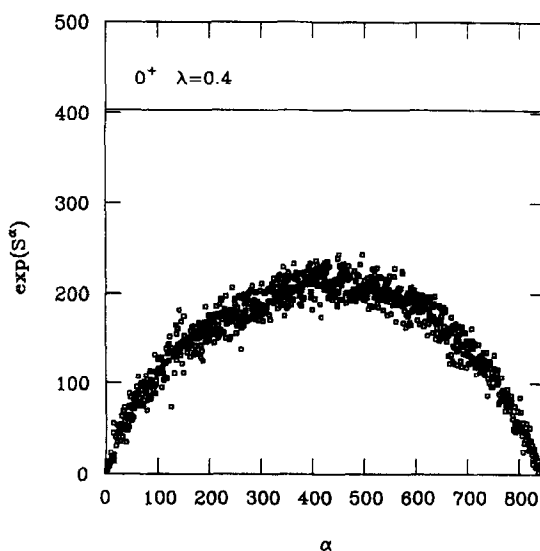


Fig. 37. Information length for the 0^+0 states at the strength of the off-diagonal matrix elements of the residual interaction, suppressed by a factor 0.4. The solid line shows the GOE value.

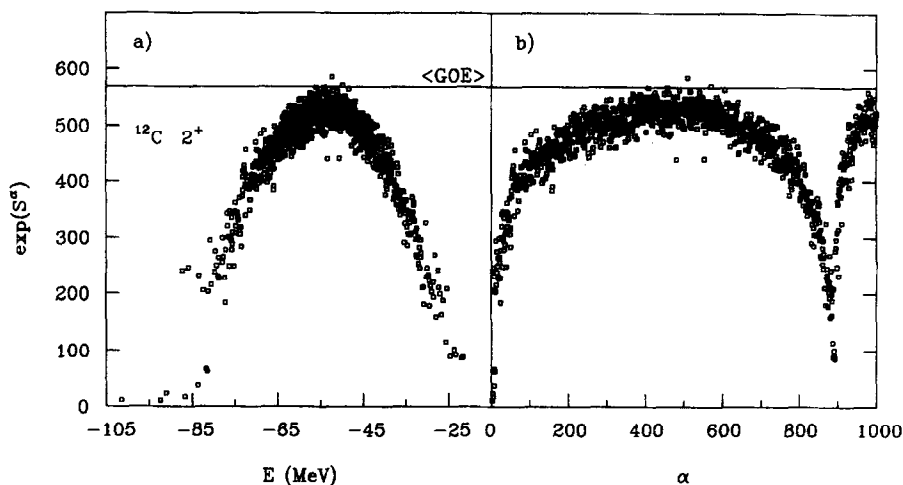


Fig. 38. Information length for 1183 2^+0 states in ^{12}C calculated with the Warburton–Brown interaction [99] in 4 major oscillator shell space for $(0 + 2)\hbar\omega$ excitations; panel a is given in the energy scale; panel b is given in the α -scale where states with and without center-of mass motion are differentiated. The solid line shows the GOE value.

account $(0 + 2)\hbar\omega$ excitations. This space is complete for the center of mass excitation in $0p$ -shell nuclei. The interaction used in the calculation was that of Warburton and Brown [99] which contains a cross-shell part. The information length l_3^2 , Fig. 38(a), has a generic Gaussian energy dependence with the maximum at the GOE limit equal to 570. Depicting the same data in the α -scale, Fig. 38(b), we can clearly differentiate the states with the lowest center of mass energy (first

arch) from those with the excited center of mass motion (second arch). They have the same degree of internal complexity.

4.3. Representation dependence

In the previous section all results were obtained using the shell-model basis as a reference representation. From the physical point of view, this representation reflects the main ideas of the mean field approach which starts with the independent constituents. Their residual interaction is responsible for the mixing of basis states and stochastization of the dynamics. Two important features of our results are to be stressed.

(i) The information entropy was calculated in the original shell-model basis for all individual eigenfunctions with no averaging elements. The eigenfunctions, adjacent on the energy scale, could have very different intrinsic structure and localization properties. Therefore one could expect strong fluctuations of their degree of complexity or the localization length. Contrary to this expectation, our results, Figs. 31 and 32, show only modest fluctuations superimposed onto a very smooth function of excitation energy. The fluctuations around the average level are of statistical nature (in a rough approximation, their relative magnitude is $\propto N^{-1/2}$ as can be seen from the comparison of Figs. 31 and 32).

We can conclude that the eigenstates presented in the mean field basis display on average the degree of complexity regularly evolving along the spectrum. This complexity reflects common features of neighboring eigenstates which are apparently unrelated in a direct dynamic sense. Being a function of excitation energy only, the degree of complexity can therefore be considered as a thermodynamic variable. We return to this question in Section 6.

(ii) The resulting degree of localization of the eigenfunctions in the shell model basis depends strongly on the strength of the mixing interaction, compare Fig. 32(b) with Fig. 33 where the stabilizing influence of the mean field is turned off. This once more confirms the general trend of the mean field to quench the chaotic signatures of many-body dynamics.

To illustrate the exceptional role of the mean field as a reference representation, we compare the results for the degree of complexity calculated with the aid of this “natural” basis with similar calculations using different representations.

The $\mathcal{SU}(3)$ hamiltonian is a popular model [100] which explains from the group-theoretical viewpoint the appearance of quadrupole deformation and rotational bands. The attractive feature of this approach is that the angular momentum is strictly conserved which is not the case in the cranking model. The exact solution of the $\mathcal{SU}(3)$ hamiltonian is well known. Apart from collective dynamics, it was used for the test of statistical spectroscopy [55].

We computed the informational entropy of our exact eigenvectors, taking the basis of the eigenfunctions of the $\mathcal{SU}(3)$ as a reference basis. The results shown in Fig. 39(a) clearly demonstrate that in the $\mathcal{SU}(3)$ basis almost all eigenvectors are completely delocalized over the entire available Hilbert space. It means that the $\mathcal{SU}(3)$ basis, invented to account for the collective rotational features of nuclei, is not able to probe the evolution of complexity along the spectrum. It turns out to be practically random with respect to the process of stochastization, quite analogously to a pure random basis which was taken as a representation basis in Fig. 39(b).

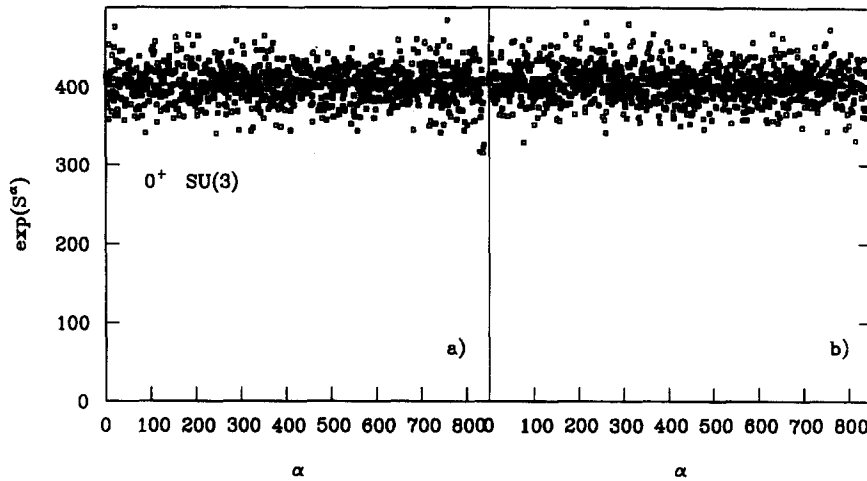


Fig. 39. Information length for 839 0^+0 eigenstates of the realistic hamiltonian in the eigenbasis of the $\mathcal{SU}(3)$ hamiltonian (a) and in the eigenbasis of the 839-dimensional random hamiltonian (b). The solid line gives the GOE value.

One can speculate that the shortcomings of the $\mathcal{SU}(3)$ basis for our purposes are connected with the unrealistic features of the single-particle level scheme and absence of the strong pairing-type interaction in the particle–particle channel. Its interference with the multipole interaction in the particle–hole channel should be helpful for the smooth increase of the degree of complexity. On the other hand, it might be important that the realistic interaction contain a fraction of incoherent scattering processes (“noise”).

We can conclude that a certain degree of self-consistency between the representation basis and the residual interaction is necessary to achieve a meaningful description of stochastization. The mean field basis is the most appropriate for this purpose.

4.4. Other measures of complexity

As we mentioned, the use of the moments (62) of the distribution function of the components can give complementary information. The effective number of principal components (NPC) as defined from the participation index,

$$(\text{NPC})^\alpha = (M_2^\alpha)^{-1}, \quad (63)$$

is shown by Fig. 40 in the α -scale for 2^+0 states. Although the qualitative behavior is again strongly correlated with the level density and the information entropy, this quantity also does not reach the GOE limit $N/3 = 1091$. The deviation is about 12% for the middle part of the spectrum. It means that in the realistic shell model with no degeneracies the eigenstates have finite localization length. However their structure is close to the random superposition of N_α basic states, as is visualized in Fig. 41(a). One can eliminate the variable local average value of N_α by calculating various ratios of moments, for example $l_3^\alpha/(\text{NPC})^\alpha$. For a Gaussian distribution of components (54), this ratio has the universal value $l_3^\alpha/(\text{NPC})^\alpha = 1.44$. As seen from Fig. 41, the results for the majority of the 2^+0 state vectors are close to this expectation.

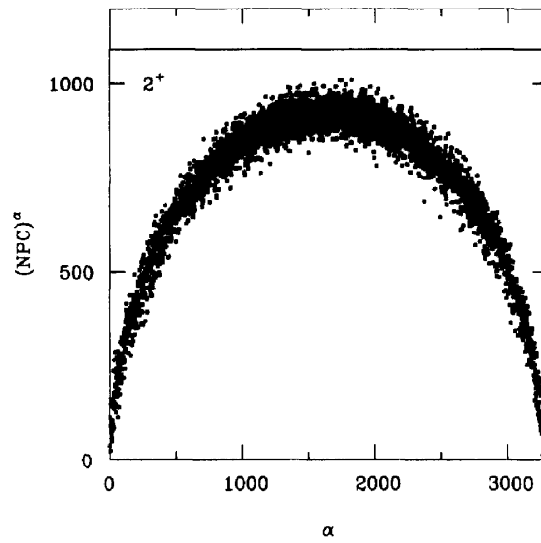


Fig. 40. Number of principal components, Eq. (63), for the 2^+0 states, the solid line gives the GOE value.

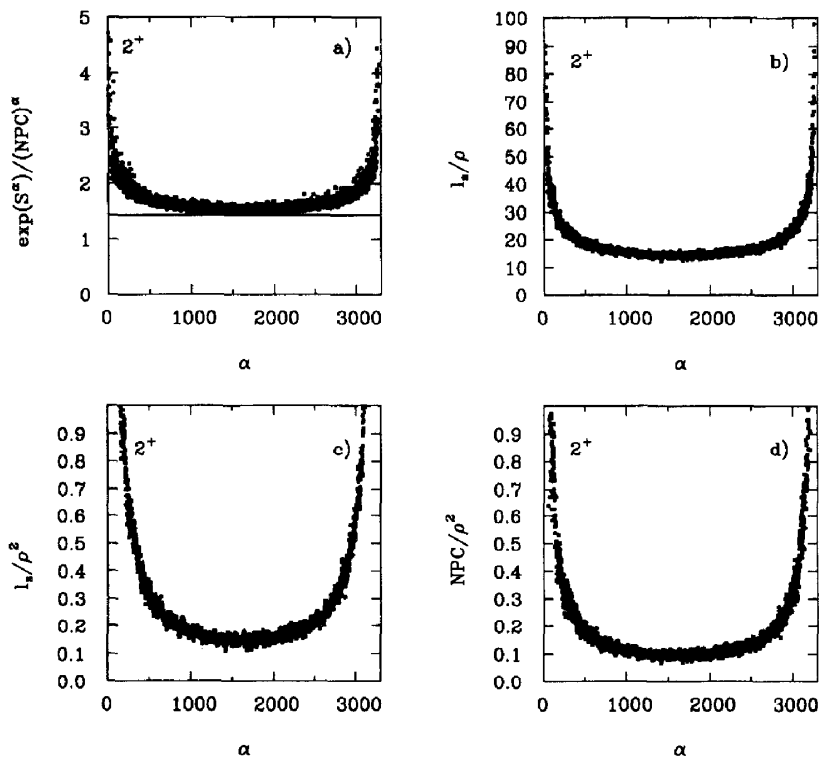


Fig. 41. Correlations of different measures of complexity for individual 2^+0 states. (a) Ratio of the information length to the number of principal components, the horizontal line shows the GOE value 1.44. (b) Ratio of the information length to the level density. (c) Ratio of the information length to the squared level density. (d) Ratio of the number of principal components to the squared level density.

In the Gaussian BRM ensemble [72] the localization length of eigenstates is proportional to the square of the local level density $\rho(E)$. This prediction is checked for both localization measures, $\exp(S^\alpha)$ and $(NPC)^\alpha$, plotting their ratios to $\rho^2(E)$ in Figs. 41(c) and (d), respectively. We see that the localization lengths drop faster than they would in the BRM ensemble. One should remember that the BRM ensemble [72] does not include the regular diagonal part of the hamiltonian which is more effective in the region of lower level density. Fig. 41(b) in comparison with 41(c) shows that, except for the edges of the spectrum, the localization length l_S is approximately proportional to the density $\rho(E)$ rather than to its square. This means the strong correlation between thermodynamic entropy $\sim \ln \rho$ and information entropy, see below Section 6.

4.5. Correlations of eigenvector components

As we mentioned in Section 4.3, in the GOE the components of the eigenvectors are dynamically independent. The only source of correlations between those components is the unitarity of the transformation from the original basis $|k\rangle$ to the eigenbasis $|\alpha\rangle$. In the N -dimensional space, N normalization conditions and $N(N-1)/2$ orthogonality conditions still leave $N(N-1)/2$ free parameters determining the amplitudes. Therefore the correlations of the weights W_k^α , Eqs. (52) and (53), are weak and die out in the limit of large N . In contrast to the GOE, the realistic strongly interacting system has dynamical correlations built in. The first obvious candidate in the nuclear case is the pairing correlation of the superconducting type which will be discussed in more detail in Section 7. Using the calculated eigenstates, we can examine the correlation functions of their components looking for comparison with the GOE and for remnants of regular collective behavior.

The correlation function of the weights is presented for the 0^+0 states in Fig. 42. We fix the eigenstates $|\alpha\rangle$ in the product $W_k^\alpha W_l^\alpha$, see Eq. (52), and average over all components k and l keeping a certain value of the “distance” $l-k$ where the basis states $|k\rangle$ are ordered according to their centroid energy \bar{E}_k . The cyclic boundary conditions are assumed so that the state $|k=1\rangle$ is the next one after the state $|k=N\rangle$. The result of averaging is multiplied by N^2 in anticipation of the order of magnitude of the correlation foreseen by the GOE (52).

Figs. 42(a) shows the diagonal ($l=k$) correlation function $N^2 \overline{(W_k^\alpha)^2}$ for all eigenvectors $|\alpha\rangle$. In the middle of the spectrum it is constant and equal approximately to 3.6 for all $|\alpha\rangle$. This number is close but still deviates from the GOE value of three, corresponding to the random distribution of the orthogonal unit vectors over the surface of the $(N-1)$ -dimensional sphere in N -dimensional space. At the edges of the spectrum, the typical values are higher by almost an order of magnitude due to the smaller complexity and larger typical weight of components of these states. Of course this is just another representation equivalent to the calculation of the $(NPC)^\alpha$ in the preceding subsection. Figs. 42(b)–(e) display the correlation functions $N^2 \overline{W_k^\alpha W_l^\alpha}$ of different components, $l-k=1, 10, 100$, and 400. The majority of states reveal a correlation function close to unity in qualitative agreement with the GOE prediction (52). However, the shorter range correlations do still exist. The case of the adjacent components, $l=k+1$, Fig. 42(b), displays a correlation pattern almost identical with that for the diagonal case $l=k$, Fig. 42(a), with the same enhancement 1.2 with respect to the GOE. Figs. 42(a) and (b) differ merely by the overall factor of three originating from the close to Gaussian distribution of the components.

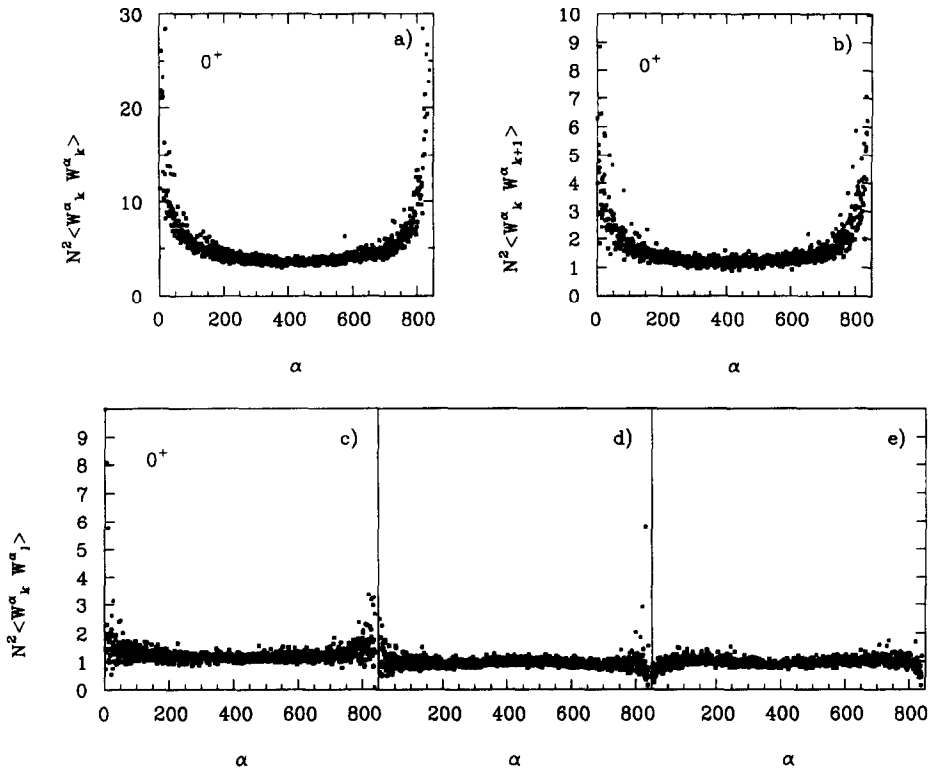


Fig. 42. The correlation function of the weights $N^2 \overline{W_k^\alpha W_l^\alpha}$, Eq. (52), for the 0^+0 states; $l = k, k + 1, k + 10, k + 100$ and $k + 400$ for parts a, b, c, d, and e, respectively. The GOE values are equal to 3 in case (a) and to 1 in all other cases.

The correlation function for $l = k + 10$, Fig. 42(c), is also enhanced by the factor 1.2 in the middle. This reflects the incomplete mixing. If the corresponding normalization factor in the definition of the correlation function were taken as N_α^2 instead of N^2 , in the middle part of the spectrum one would receive $N_\alpha/N = (1.2)^{-1/2} = 0.9$ in agreement with what we extracted earlier from information entropy and the NPC.

The long range correlation functions, $l = k + 100$ (Fig. 42(d)) and $l = k + 400$ (Fig. 42(e)), are rather close to unity with correlational edges strongly suppressed. The correlation length of the order of 100 in the k -scale can be translated into the correlation energy interval of the order of 10 MeV with the use of the typical level spacing 100 keV for the 0^+0 states. This agrees with the magnitude of the energy dispersion of Eq. (20) which is related to the fragmentation of the basis states and the spreading width, see Section 5.

The fact that the correlation functions evolve along the spectrum in a regular way can also be illustrated by direct comparison with the information entropy and the number of principal components. Fig. 43 shows the correlation function of the adjacent components $\overline{W_k^\alpha W_{k+1}^\alpha}$ multiplied by $[\exp(S^\alpha)/0.48]^2$, Fig. 43(a), or by $[3(\text{NPC})^\alpha]^2$, Fig. 43(b). Both quantities would be equal to unity for all states in the GOE case; the result would be the same if one could use the Gaussian distribution with an effective local number of states N_α in all characteristics of complexity of a given state. We see that these products approach unity in the middle part. However, they still depend on

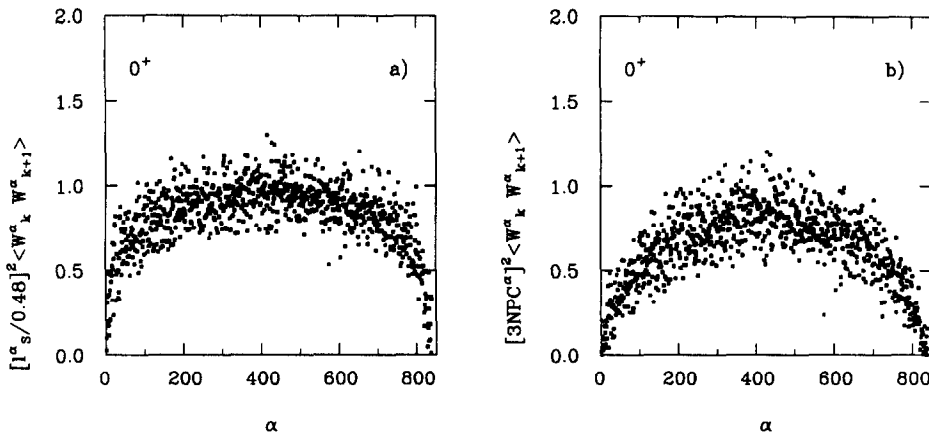


Fig. 43. Interrelation between the decorrelation of the neighboring components and various measures of the delocalization for the 0^+0 states: the correlation function $\overline{W_k^\alpha W_{k+1}^\alpha}$ multiplied by $[l_s^\alpha/0.48]^2$, panel a, and by $[3(\text{NPC})^\alpha]^2$, panel b. The GOE value is 1.

excitation energy. The effective number of components contributing to information entropy or to (NPC) is smaller than the decorrelation factor in (52), except for the most complicated states. It means that decorrelation occurs faster than the delocalization of the wave functions, and the actual distribution function of the eigenvector components systematically deviates from the local Gaussian distribution.

4.6. Do we really measure complexity?

The essential shortcoming of using such characteristics as information entropy or the moments of the distribution function of the components is their inability to distinguish a genuine chaotic behavior from the complexity (more precisely, delocalization) associated with collective motion or with the improper choice of the basis. Certainly, this is also related to the representation dependence discussed in Section 4.3.

Collective excitations $|c\rangle$, as for example found in the framework of the random phase approximation (RPA), of course also can be presented by superpositions (5). But in this case the amplitudes C_k^c are coherent with respect to a certain simple (one-body in the RPA) operator Q . The coherence means that the phases of the amplitudes C_k^c are synchronized with those of the matrix elements Q_{k0} for a transition between simple states, for example between the ground state $|0\rangle$ and a 1p–1h state $|k\rangle$. For a coherent linear combination $|c\rangle$, the partial amplitudes add constructively so that the transition probability $|0\rangle \rightarrow |c\rangle$ is enhanced, as compared to the probability of the elementary shell model transition $|0\rangle \rightarrow |k\rangle$, by a factor N_c which is a number of coherent components contributing to the wave function $|c\rangle$. If N_c is large enough, our measures of complexity will signal an appearance of a complicated state which definitely has nothing to do with chaos. For instance, a coherent state $|\alpha\rangle$ of a harmonic oscillator defined as an eigenstate of the annihilation operator, $a|\alpha\rangle = \alpha|\alpha\rangle$, is a quantum counterpart of regular semiclassical motion. For a large average number of quanta $\bar{n} = |\alpha|^2$, both $\exp(S^\alpha)$ and $(\text{NPC})^\alpha$ are growing $\propto \sqrt{\bar{n}}$ (the exact result is $(\text{NPC})^\alpha = \exp(-2\alpha^2)I_0(2\alpha^2) \approx 2\sqrt{\pi\bar{n}}$ where I_0 is a modified Bessel function).

We should however keep in mind that (i) the actual degree of collectivization in nuclei N^c is usually small compared to the degree of complexity of typical complicated states; only in the case of low lying quadrupole excitations of vibrational or rotational type in heavy nuclei one has $N^c \simeq 10^2$; (ii) the fraction of collective states is small ($\sim 1/N^c$) so their statistical weight is presumably negligible, (iii) as the excitation energy increases, the relative degree of complexity of such states actually decreases (in the example of coherent states $(NPC)/\bar{n} \propto \bar{n}^{-1/2}$ as it is necessary for the transition to the regular classical limit), and (iv) in a realistic many-body system only the lowest collective states are approximately stationary, but in that energy domain there is no chaos anyway. Nuclear collective states at sufficiently high excitation energy are strongly mixed (damped), so the only surviving signature of collectivity could be a nonstatistical excess of specific 1p–1h basis components concentrated at a certain energy in the interval of the spreading width and manifested by a peak of the strength function of the operator Q .

The problems associated with an inappropriate choice of the basis can be more dangerous. Considering, for example, a tight binding model of a particle in a periodic N -well potential and using the localized states as the basis states, we easily find for the stationary delocalized standing wave solutions $(NPC) = (2/3)(N + 1)$ for all wave vectors. This complexity, being higher than in the GOE ensemble, is simply a manifestation of the uncertainty relation between the coordinate and the wave vector. (In our studies we never saw complexity which would considerably exceed the GOE limit). In many cases there exists a smooth evolution or phase transition of the mean field along with increasing energy (or temperature). Change of shape of the mean field, even if the new shape supports regular single-particle motion, can be misinterpreted as an onset of chaos due to the complexity of new stationary eigenstates expressed in the old representation. But in such cases the invariant measures of chaos connected to the level statistics unequivocally indicate absence of chaos.

5. Fragmentation and spreading

In the preceding section we discussed the average properties of the distribution of components of the stationary wave functions and found a qualitative overall agreement with the local Gaussian distribution along with small deviations revealed by the correlational analysis. In many physical problems it is important to study the fragmentation of simple states $|k\rangle$ over the exact eigenstates $|\alpha\rangle$ rather than the inverse problem of localization discussed earlier. Of course, both questions are to be answered by means of the same matrix of transformation amplitudes C_k^α which are real in our case of time-reversal invariance. In this section we will be interested in details of the distribution of components for a given simple state and in generic features of this distribution.

In a time-dependent picture, specific states $|k\rangle$ describe the initial stage of the excitation process induced by a simple (one- or two-body) external field. As in the Landau theory of Fermi-liquid, one can have a reasonable description of the response to an external perturbation in terms of undamped individual elementary excitations only on a relatively short time scale until the relaxation processes lead to the finite lifetime of simple modes. In our language of stationary states, this relaxation is nothing but mixing with more complex configurations. (Consideration of decay to the continuum [32] being an important issue both from practical and conceptual viewpoints is outside the scope of the present work). As the result of mixing, the strength of the original mode is fragmented over exact stationary states within an energy interval Γ (the spreading width).

5.1. “Standard model” of the spreading width

The definition of the spreading width traditionally assumes that the decomposition of the simple state in terms of the stationary components with energies E_α has the Breit–Wigner shape. This would correspond to the pure exponential decay of a simple excitation with the mean lifetime $\tau \sim \hbar/\Gamma$. This is the case in the “standard” model [21] of the strength function, where a simple mode is coupled with the infinite picket fence of complicated background states via constant (or weakly fluctuating) matrix elements. As we discussed in relation to the spectral rigidity, in the discrete spectrum with the finite energy uncertainty of the initial state, its damping cannot be exponential on a short time scale which corresponds to the non-Lorentzian tails of the strength function. The question of how good is the Breit–Wigner approximation of the strength function has to be studied using the specific dynamical properties of the system.

Let us consider fragmentation of the strength of a simple state $|k\rangle$. In the standard model one acts in two steps. First, the state $|k\rangle \equiv |1\rangle$ is excluded and the $(N - 1) \times (N - 1)$ submatrix of the hamiltonian including the remaining original $N - 1$ basis states is fully diagonalized to give intermediate eigenvectors $|v\rangle$ and eigenvalues E_v , $v = 2, \dots, N$. This diagonalization defines the transformation matrix $\langle k'|v\rangle$, $k', v \geq 2$. After the prediagonalization the transformed hamiltonian consists of the diagonal elements ($H_{kk} = \bar{E}_k$ and E_v) and the coupling matrix elements

$$V_{kv} \equiv \langle k|H'|v\rangle = \sum_{k' > 1} H'_{kk'} \langle k'|v\rangle \tag{64}$$

in the k th row and the v th column, $v \neq k$.

The second step is the explicit diagonalization of the intermediate hamiltonian, i.e. transformation from the states $|k\rangle$ and $\{|v\rangle\}$ to the eigenstates $|\alpha\rangle$, Eq. (5). The exact energies $E = E_\alpha$ are the roots of the secular equation (poles of the Green function $G(E)$)

$$G^{-1}(E) \equiv E - \bar{E}_k - \sum_v V_{kv}^2 / (E - E_v) = 0. \tag{65}$$

Here the intermediate energies E_v and the matrix elements (64) do depend on the choice of the removed state $|k\rangle$ but the roots E_α do not.

The eigenvectors can be represented by a superposition similar to that of Eq. (5) with the new amplitudes D_v^α ,

$$|\alpha\rangle = C_k^\alpha |k\rangle + \sum_{v \neq k} D_v^\alpha |v\rangle = C_k^\alpha |k\rangle + \sum_{k', v \neq k} C_{k'}^\alpha \langle v|k'\rangle |v\rangle. \tag{66}$$

The amplitude C_k^α , which is of course the same as in (5), determines the fraction of the strength of a simple state $|k\rangle$ carried by an eigenstate $|\alpha\rangle$,

$$W_k^\alpha \equiv (C_k^\alpha)^2 = \left(\frac{dG^{-1}}{dE} \right)_{E=E_\alpha}^{-1} = \left[1 + \sum_v \frac{V_{kv}^2}{(E_\alpha - E_v)^2} \right]^{-1}. \tag{67}$$

The standard model assumes that (i) the “background” states $|v\rangle$ have the rigid energy spectrum with mean level spacing D , (ii) this spectrum does not considerably change due to the removal of a single state $|k\rangle$, and (iii) the squared matrix elements V_{kv}^2 are uncorrelated with the energies E_v being of the same order of magnitude for all background states. For the dense uniform background characterized by the level density $\rho(E) \simeq D^{-1}$, one can introduce, instead of the

discrete set of the fragmentation amplitudes (67), the smooth strength function $F_k(E)$ of the state $|k\rangle$, see Section 2.4,

$$F_k(E) = \sum_{\alpha} W_k^{\alpha} \delta(E - E_{\alpha}) = \rho(E) \langle W_k^{\alpha} \rangle_{E_{\alpha}=E} \quad (68)$$

where the average is taken over several eigenstates in the vicinity of energy E . The assumptions of the standard model allow one to substitute V_{kv}^2 effectively by the appropriate average value $\langle V^2 \rangle$. The following summation over the infinite picket fence of the background states implies the infinite energy dispersion. Under these conditions, Eqs. (65)–(68) lead [21] to the Breit–Wigner strength function,

$$F_k(E) = \frac{1}{2\pi} \frac{\Gamma}{(E - \bar{E}_k)^2 + \Gamma^2/4}, \quad (69)$$

where the spreading width is given by the golden rule,

$$\Gamma = 2\pi \frac{\langle V^2 \rangle}{D}. \quad (70)$$

This value is widely used for the estimates of the spreading widths. Below we present the more general treatment, taking into account the finite spreading width of the doorway states. The arguments follow those of Ref. [44].

5.2. Spreading width in the stochastic regime

Let us discuss the main ingredients of the standard model. The assumption (i) of the dense uniform background is quite reasonable in the stochastic regime we are interested in. However, in the region of strong mixing the spreading width can be large enough so that the level density $\rho(E)$, which is an important factor in the strength function (68), changes significantly in the relevant energy range. Of course, as assumed in (ii), the properties of the background are not influenced by the omission of one of the basis states. However, the assumption (iii) of the coupling matrix elements uncorrelated with the energies of the background states can easily be violated. In general, the matrix elements are decreasing as one moves away from the centroid of the original state. This can be understood from the band-like structure of the shell-model hamiltonian, in contrast to the full GOE matrix.

The shell-model selection rules define, for each basis state, its doorway states as those participating in the first mixing step. In the exciton (particle–hole) language they belong to the same or to the next level of complexity. But the doorway states have their own finite spreading widths. Therefore their strength covers a finite range of energy ΔE . Outside of this interval the magnitude of the coupling matrix elements V_{kv} decreases. As discussed in [58, 59], this restricts the validity of the standard model, which corresponds to the limit $\Delta E \rightarrow \infty$, and can bring the shape of the strength function closer to Gaussian. In particular, this effect can be responsible for the relatively narrow width of multiple giant resonances scaling as \sqrt{n} with the phonon number n . Even small deviations from the Breit–Wigner shape for a single phonon strength function become more pronounced after the convolution in the double phonon excitation. In agreement with the central limit theorem, the resulting shape is driven in the direction of the Gaussian. In general, the strength function is not

necessarily of the Breit–Wigner shape even in the central part, and the “decay” of simple modes is not exponential.

The standard model is valid if the resulting width Γ is less than the range ΔE of considerable interaction strength (the weak coupling case in terms of Ref. [44]). In the opposite (strong coupling) case the formally calculated spreading width (70) exceeds ΔE , and the assumptions of the standard model break down [58, 59, 44]. Then the actual spreading width is proportional to $\sqrt{\langle V^2 \rangle}$ instead of $\langle V^2 \rangle$ as in Eq. (70). Apparently these two limits were first recognized by Wigner [68]. They were studied recently [101] in application to banded random matrices.

A self-consistent theory for the strength function taking into account the coupling to the doorway states which, in turn, are fragmented in a similar way, was developed in [44]. It is valid for any ratio $\Gamma/\Delta E$. The coupling matrix elements $H_{kk'}$ in the stochastic regime are uncorrelated with the components $\langle k'|v \rangle$ of the background states. Therefore the squared matrix elements (64) on average can be represented as

$$\langle V_{kv}^2 \rangle \approx \sum_{k'} \langle |H_{kk'}|^2 \rangle \overline{|\langle k'|v \rangle|^2} \approx \sum_{k'} \langle |H_{kk'}|^2 \rangle \frac{F_{k'}(E_v)}{\rho(E_v)}. \quad (71)$$

In the stochastic regime a randomly selected state $|k \rangle$ is assumed to be similar to other background states. The case of a nongeneric, for example collective, state embedded into the compound background was considered in [44]. We expect all typical states $|k \rangle$ to be characterized by the same generic strength function $F(z)$ depending only on the energy distance $z = E - \bar{E}_k$ from the corresponding centroid,

$$F_k(E) \Rightarrow F_k(E - \bar{E}_k) \equiv F_k(z_k) \approx F(z_k). \quad (72)$$

Under these approximations, Eqs. (65), (67) and (71) can be transformed into a set of coupled self-consistent equations [44] where the singular integral is defined via the limiting transition from the complex plane,

$$F(z) = \frac{1}{\pi} \text{Im} \frac{1}{z - \Sigma(z)}, \quad (73)$$

$$\Sigma(z) = \int dx \int dy f(x, y) \frac{F(y)}{z - x - i0}. \quad (74)$$

The form-factor $f(x, y)$ (the spectral distribution function) describes the distribution of magnitudes of the original off-diagonal matrix elements H_{ki} as a function of the distance between the centroids \bar{E}_k and $\bar{E}_l = \bar{E}_k + \omega$. For a given state $|k \rangle$ it is defined as

$$f_k(\bar{E}_k, \bar{E}_k + \omega) = \sum_l |H_{kl}'|^2 \delta(\bar{E}_k - \bar{E}_l + \omega) \approx \rho_k(\bar{E}_k + \omega) \langle |H_{kl}'|^2 \rangle. \quad (75)$$

The form-factor in the stochastic regime is assumed to be the same for all generic states $|k \rangle$ and to depend only on the difference $\omega = \bar{E}_l - \bar{E}_k$. It decreases when ω exceeds the range ΔE of the doorway strength. For the states $|l \rangle$ with the centroids within this range, the mixing intensity can be estimated with the aid of the average value $\langle |H_{kl}'|^2 \rangle$. The quantity $\rho_k(E)$ is the density of the doorway states, around unperturbed energy E , for the initial state $|k \rangle$. In the standard model $f(\omega) = \langle V^2 \rangle / D \approx \text{const}$. Note that the form-factor (75) is normalized to the sum of the squared

off-diagonal matrix elements, and therefore gives the spectral decomposition of the fragmentation width (19),

$$\int d\omega f_k(\bar{E}_k, \bar{E}_k + \omega) = \sigma_k^2. \quad (76)$$

As shown in Section 2.4, $\sigma_k \approx \bar{\sigma}$ is practically constant as a function of \bar{E}_k which would be the case for the uniform form-factor $f(\omega)$. Comparison with (19) shows that the interaction range can be roughly estimated as $\Delta E \approx 2bD$ where b is the effective band width ($\Delta E \approx 12$ MeV for our 2^+0 states). The characteristic value of the form-factor is $\bar{\sigma}^2/2bD \approx 8$ MeV for the 2^+0 states.

Fig. 44 shows the histogram for the form-factor (75) summed over all 0^+0 states. It has a Gaussian behavior as a function of ω with the centroid at $\omega = 0$ and the dispersion $\sigma_f = 9.5$ MeV.

Eqs. (73) and (74) found for the stochastic regime allow analytical solutions in the two limiting cases. The weak coupling limit corresponds to the spreading width Γ well within the range ΔE of interaction. The self-energy $\Sigma(z)$ is then a slowly changing function and can be taken at the origin. The integral over y in (74) is effectively confined to the region of the size Γ where the form-factor does not change significantly and can be taken outside the integral at the value near the origin. The remaining integral $\int dy F(y) = 1$ by the normalization (15) of the strength function. In this case we get the Breit–Wigner strength function $F(z)$, Eq. (69), with the universal spreading width

$$\Gamma = 2\pi f(0). \quad (77)$$

The standard model expression (70) is a particular case of (77). The condition for the validity of this result is $2\pi f(0) < \Delta E$. For the parameters of the 2^+0 and 0^+0 classes of states this condition is violated. The quantity (77) exceeds also the energy interval where the level density can be considered as approximately constant.

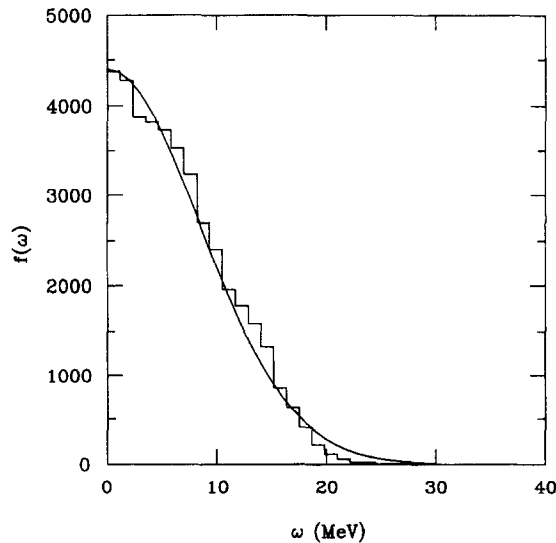


Fig. 44. The spectral form-factor $f(\omega)$, Eq. (75), for the 0^+0 states (histogram) and Gaussian fit (dashed line).

In the opposite limit of the strong coupling $\Gamma > \Delta E$, the effective range of integration is determined by the more rapidly decreasing form-factor. Then one can put the strength function F outside the integral over y in Eq. (74) and use the normalization condition (76). In this case the details of the form-factor play no role, and the result can be expressed in terms of the total fragmentation strength $\bar{\sigma}$. The strength function given by the solution of Eqs. (73) and (74) turns out to be a semicircle with radius $2\bar{\sigma}$,

$$F(z) = \frac{1}{2\pi\bar{\sigma}^2} \sqrt{4\bar{\sigma}^2 - z^2}. \quad (78)$$

The solution is consistent with the definition (18) and (19) of the second moment of the strength function which gives $\sigma^{(2)} = \bar{\sigma}$. The effective spreading width (FWHM) is here $\Gamma = 2\sqrt{3}\bar{\sigma}$. Note the linear dependence on the magnitude of the residual interaction in contrast to the quadratic dependence of the golden rule (70).

The wings of the strength distribution cannot be described by the limiting expressions, Breit–Wigner or semicircle. They depend on the precise shape of the form-factor. Assuming that the equations of the stochastic regime are still valid for the tails of the strength functions, one obtains the limiting behavior

$$F(z) \propto f(z)/z^2 \quad (79)$$

at large z . For the Breit–Wigner form-factor used for illustrative purpose in [44], it would give the wings of the strength function $F(z) \propto z^{-4}$.

As we will see, the actual situation in our shell-model calculations is intermediate between these two limits. The weak coupling limit is ruled out by the fact that the localization length increases with the interaction strength λ much slower than proportional to λ^2 . It was mentioned in Section 4.2 in relation to Fig. 37 corresponding to $\lambda = 0.4$. The strength function drops faster than in the Breit–Wigner case but slower than the semicircle rule so Eq. (78) would overestimate the average spreading width. A similar conclusion was reached [35] for the atomic states. However, the evolution of the eigenstates along the spectrum prevents using the limiting predictions of (79). A large value of Γ means that the strength functions cover the regions of the spectrum where the wave functions manifest different degrees of complexity. Therefore the assumption of global uniformity is broken.

5.3. Strength functions of basis states

In order to examine the fragmented structure of individual basis states $|k\rangle$, we group the weights $W_k^\alpha = (C_k^\alpha)^2$ of several neighboring eigenvectors $|\alpha\rangle$ for given k in bins and build a histogram as a function of an average bin energy. This corresponds precisely to the definition of the strength function $F_k(E)$ of the state $|k\rangle$, Eq. (17). As shown by Fig. 45(1a)–(9a), for 9 individual 0^+0 basis states with the centroids \bar{E}_k in the middle of the spectrum, the resulting histograms are very different in detail and display strongly fluctuating patterns, but they have similar widths. Following the idea of ergodicity and considering these histograms for various $|k\rangle$ as independent realizations of a statistical ensemble, we can average them out in order to extract the typical strength function for this class of states.

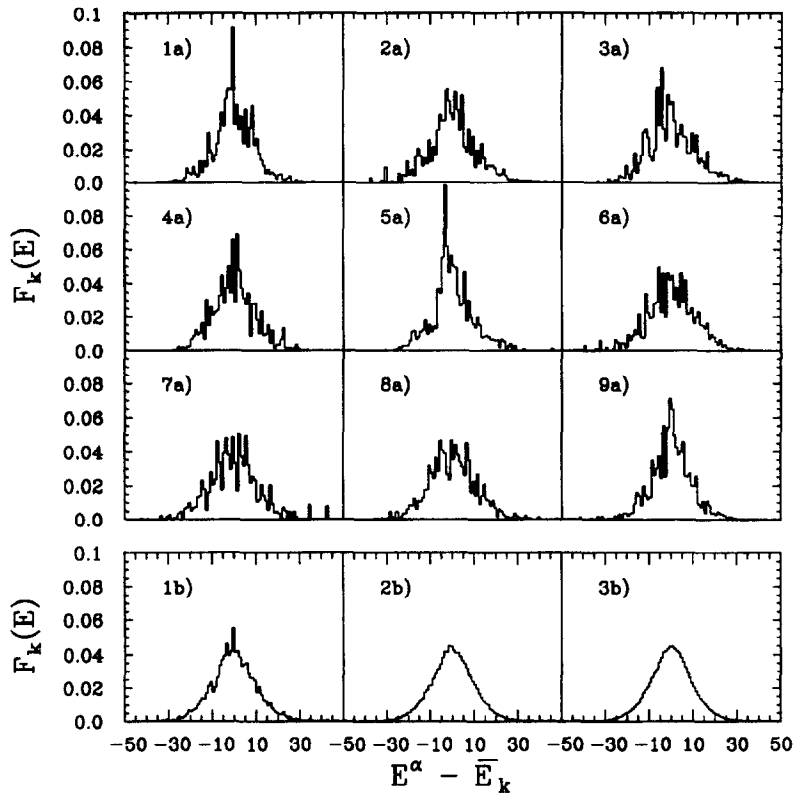


Fig. 45. The strength functions, Eq. (68), for 9 individual 0^+0 eigenstates $|\alpha\rangle$ in the middle of the spectrum (histograms) vs the energy distance, $E^\alpha - \bar{E}_k$ (MeV), from the centroid of the unperturbed state $|k\rangle$, panels 1a–9a, and the strength function averaged over 10, 100, and 400 0^+0 states in the middle of the spectrum, panels 1b–3b, respectively. The bin size is 1 MeV.

The result of such averaging obtained by the superposition of 10, 100, and 400 strength functions in the middle of the spectrum is given by Fig. 45(1b), (2b) and (3b), respectively. The fluctuations are smeared away and one can observe the generic shape. We could not find a simple parameterization which would satisfactorily fit both the central part and the wings of the distribution. Fig. 46(a) shows both the Breit–Wigner and the Gaussian fits to the central region. Beyond the half-maximum height, the data decreases much faster than the Breit–Wigner curve. This deviation is clearer from the logarithmic plot of Fig. 46(b). The Gaussian fit is in good agreement with data except for the wings where it falls off faster than needed. Again this shows up distinctly with the aid of the logarithmic scale. From the Gaussian fit for the main part of the strength function we get a dispersion $\Delta_F = 8.9$ MeV which is close to the value of 9.5 MeV discussed earlier (Fig. 44) for the form-factor $f(\omega)$. It corresponds to a typical spreading width (FWHM) of the middle 0^+0 states equal to $\Gamma = (8 \ln 2)^{1/2} \Delta_F = 21$ MeV.

Using this value, the level density $\rho \approx 10$ MeV $^{-1}$, and the Breit–Wigner relation $\langle N_\alpha \rangle = (\pi/2)\rho\Gamma$ between the spreading width and the number of principal components of the wave function, we get $\langle N_\alpha \rangle \approx 330$, which is roughly consistent with the value observed for the middle part of the spectrum in Fig. 31 obtained for information entropy.

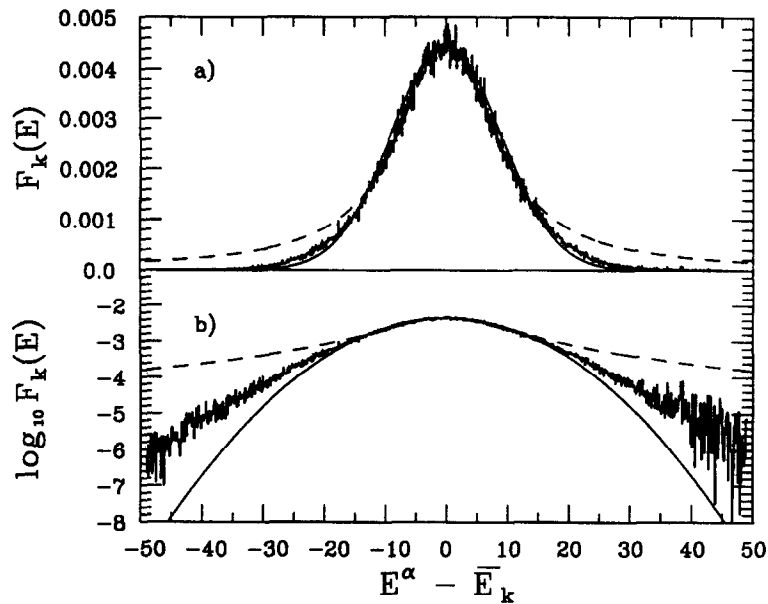


Fig. 46. The Breit–Wigner fit (solid lines) and Gaussian fit (dashed lines) to the central part of the 400-state strength function (histograms), panel *a*, and the same fits on the logarithmic scale, panel *b*. The bin size is 100 keV.

As we discussed in the preceding subsection, the behavior of the tails of the realistic strength functions can be governed by factors different from those determining the main shape. This is not the case in the simple BRM ensemble without the increasing diagonal. Here, we find good agreement with data in the tails using a simple exponential fit

$$\overline{F_k(E)} \sim \exp\left(-\frac{|E - \bar{E}_k|}{L_F}\right), \quad |E - \bar{E}_k| \gg L_F. \quad (80)$$

The localization energy length of the tails of the strength function is $L_F = 5$ MeV, see Fig. 47. The agreement covers three orders of magnitude.

According to (68), the strength function $F_k(E)$ is essentially a product of two factors, namely an average weight of components of a generic eigenstate and the level density. The level density is mostly of combinatorial nature, and the main effect of the residual interaction is in broadening the distribution with the Gaussian shape kept intact. We referred to this behavior in Section 3.1. The distribution for the effective level density which enters into the summation over 400 levels in the middle of the spectrum is shown in Fig. 48. The average weight of the components is directly related to mixing and complexity reached in the stochastization process. We remove the factor of the level density and show the “pure”, intermediate between the Breit–Wigner and Gaussian, behavior of the mixing probabilities in Fig. 49; the width is equal to 13.7 MeV. The long tails of $\langle W_k^\alpha \rangle$ as a function of $E_\alpha - \bar{E}_k$ are obviously responsible for the exponential wings of the strength function.

As discussed in the previous subsection, for small spreading widths well within the interaction range ΔE , we are in the weak coupling limit. In this case the standard model is valid, and the

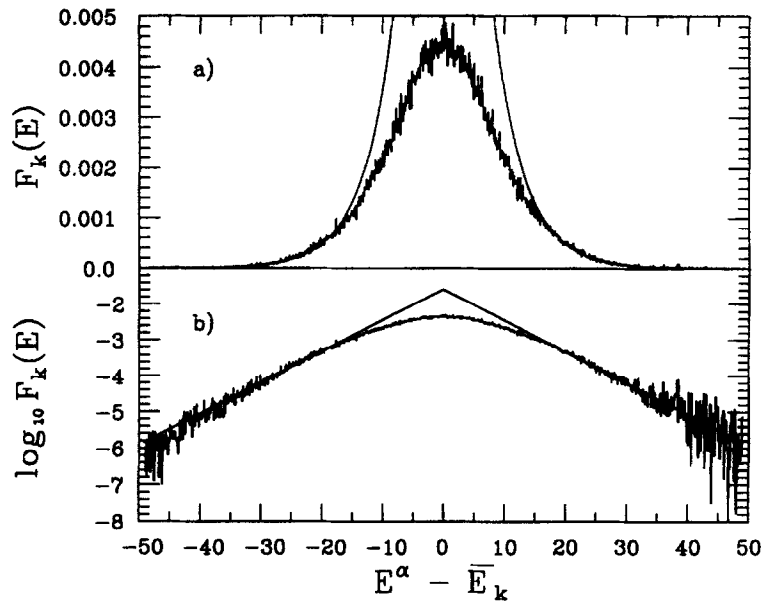


Fig. 47. The exponential fit of Eq. (80), solid lines, to the wings of the 400-state strength function (histograms), panel *a*, and the same fit on the logarithmic scale, panel *b*. The bin size is 100 keV.

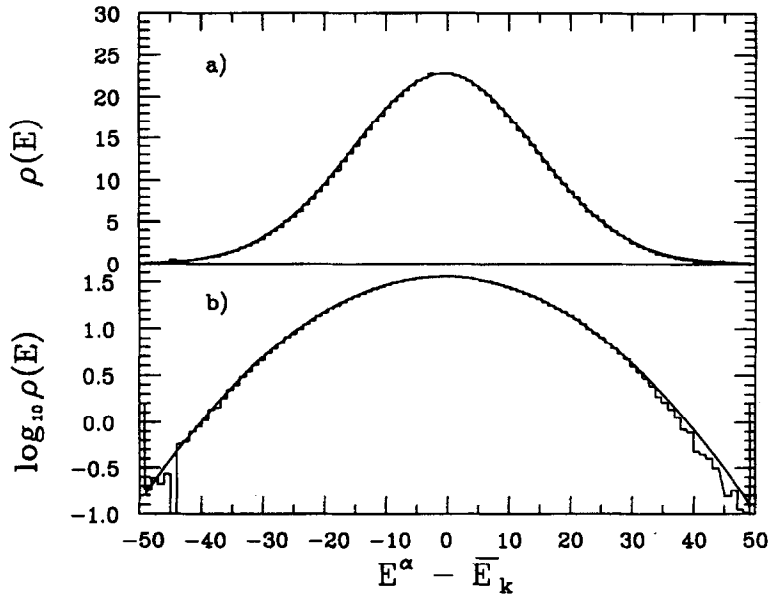


Fig. 48. Gaussian fit (solid lines) to the level density, $\rho(E)$, for the 400-state strength function, panel *a*, and the same on the logarithmic scale, panel *b*. The bin size is 1 MeV.

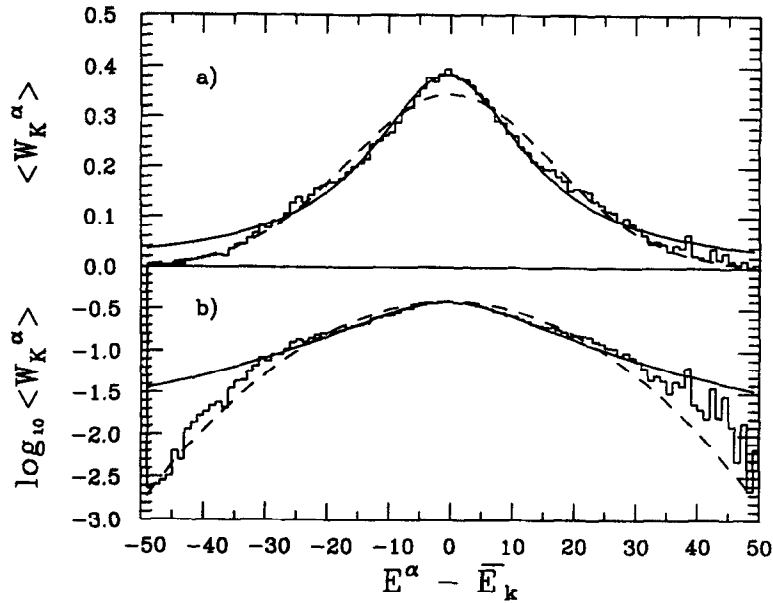


Fig. 49. Breit–Wigner fit (solid lines) and Gaussian fit (dashed lines) to the average weight, $\langle W_k^\alpha \rangle$, for 400 0^+0 states, panel *a*, and the same fits on the logarithmic scale, panel *b*. The bin size is 1 MeV.

strength function should have the Breit–Wigner shape. We performed Gaussian and Breit–Wigner fits to the strength function for the interaction strength reduced by an overall factor $\lambda = 0.2$, Fig. 50(a) and (b). As expected, a Breit–Wigner shape describes our data with high accuracy but a Gaussian is no longer sufficient as a plausible distribution function. The width of the Breit–Wigner fit is 1.1 MeV. The evolution of the shape of the strength function as a function of interaction should be studied further.

Now we are able to construct the realistic distribution function $P_{\text{comp}}(C_k^\alpha)$, see Section 4.1, of the components of the eigenvectors to be used in statistical spectroscopy [54, 56]. Neglecting the correlations discussed in relation to Fig. 43, for the majority of states it can be taken as a Gaussian,

$$P_{\text{comp}}(C_k^\alpha) = \frac{1}{(2\pi\langle W_k^\alpha \rangle)^{1/2}} \exp\left[-\frac{(C_k^\alpha)^2}{2\langle W_k^\alpha \rangle}\right], \quad (81)$$

where, according to (68), the local variance, Fig. 49(b), is given by

$$\langle W_k^\alpha \rangle = F(E_\alpha - \bar{E}_k) / \rho(E_\alpha). \quad (82)$$

The width (FWHM) of this distribution is roughly equal to

$$\Gamma_W \approx \frac{\Delta_F \sigma_E}{\sqrt{\sigma_E^2 - \Delta_F^2}} \approx 11 \text{ MeV}. \quad (83)$$

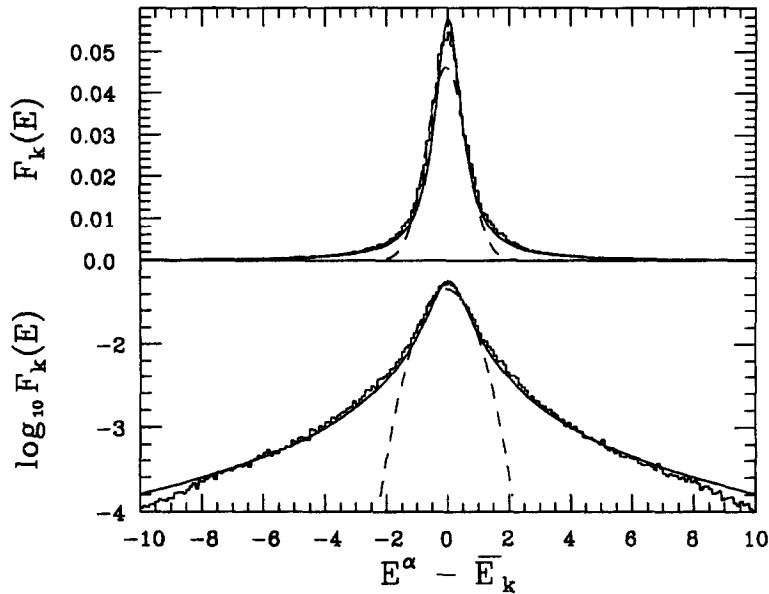


Fig. 50. The Breit–Wigner fit (solid lines) and Gaussian fit (dashed lines) to the strength function averaged over 400 0^+0 states in the middle of the spectrum for 20% interaction strength, panel *a*, and the same on the logarithmic scale, panel *b*. The bin size is 100 keV.

5.4. Two-step diagonalization and the spreading width

In order to observe the spreading widths of individual shell-model states we performed the procedure of the two-step diagonalization described in relation to the standard model [21] in Section 5.1. For this purpose the set of 0^+0 states was used.

Taking out an arbitrary basis state $|k\rangle$ and performing the diagonalization of the remaining matrix we obtain the intermediate basis $\{|k\rangle, |v\rangle\}$ with energies $\{\bar{E}_k, E_v\}$ and coupling matrix elements V_{kv} . The distribution of these matrix elements for a given removed state $|k\rangle$ can be characterized by the spectral function analogous to that of Eq. (75),

$$g_k(\bar{E}_k, \bar{E}_k + \omega) = \sum_v |V_{kv}|^2 \delta(\bar{E}_k - E_v + \omega) \approx \tilde{\rho}_k(\bar{E}_k + \omega) \langle |V_{kv}|^2 \rangle. \quad (84)$$

Here we have defined the density of intermediate states $\tilde{\rho}(E)$ and the average value of the coupling matrix element. Similar to the form-factor f , we expect that the g_k depend only on ω and are nearly the same for different states $|k\rangle$, at least at close energies. Note that, due to the orthogonal invariance of a trace,

$$\sum_{l \neq k} |H_{kl}|^2 = \text{Tr}(A_k \tilde{H}^2 A_k) = \sum_v |V_{kv}|^2 \quad (85)$$

where A_k is the projector onto the state $|k\rangle$. Therefore the form-factor (84) is normalized by the same condition (76) as the original form-factor f ,

$$\int d\omega g_k(\bar{E}_k, \bar{E}_k + \omega) = \sigma_k^2. \quad (86)$$

As the interval of averaging increases, the average form-factor rapidly evolves to the Gaussian shape. The resulting Gaussian fit is shown in Fig. 51(a); the dispersion is equal to $\sigma_g = 17$ MeV. The fitted normalization (86) of the Gaussian gives $\int d\omega g(\omega) = 104$ which agrees with the average value $\sigma_k \approx \bar{\sigma} = 10$ MeV found in Section 2.4.

Dividing out the level density of the intermediate basis states, we determine (Fig. 51(b)) the average coupling intensity $\langle |V_{kv}|^2 \rangle$. Except for the excess corresponding to the coupling to the highest and, less pronounced, lowest states $|v\rangle$, the matrix elements are nearly constant on the level $|V|^2 \approx 0.147$ MeV². It means that in this case the form-factor (84) is determined mainly by the Gaussian level density. In agreement with the idea of N -scaling, the matrix elements are bigger and display stronger fluctuations near the edges where the states of lower complexity are located.

Using this value of the squared matrix element together with the average level spacing $D \approx 0.1$ MeV in the golden rule (70), we obtain a value for the spreading width $\Gamma \approx 9.4$ MeV. Evident disagreement with the actual value of 21 MeV found in the preceding subsection demonstrates that the golden-rule estimate based on the standard model is not justified when dealing with the fragmentation and spreading widths which are of the order or larger than the scale of the change in the level density.

The wings of the strength function can presumably be calculated by perturbation theory. The exact energies E_α are located intermittently between the intermediate energies E_v and the small difference between E_v and E_α is of minor significance at large $|\bar{E}_k - E_v|$. Therefore we expect that

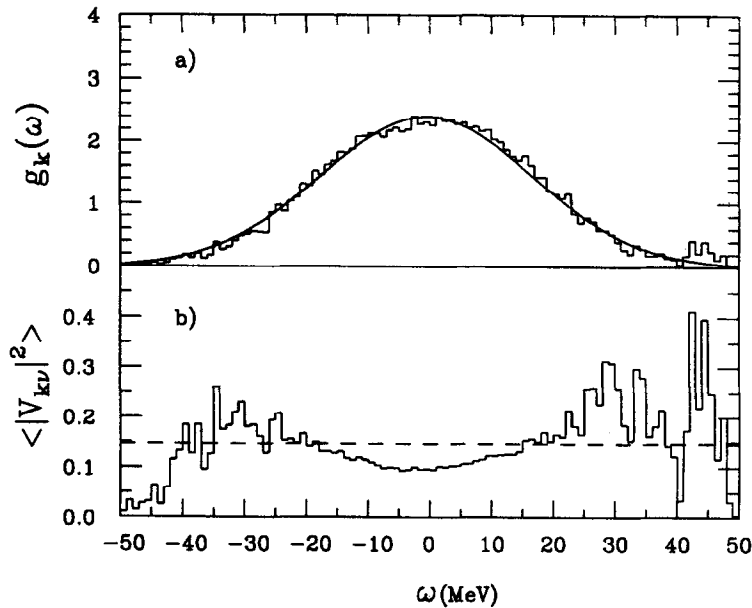


Fig. 51. The spectral form-factor $g(\omega)$ averaged over 100 0^+0 basis states in the middle of the spectrum (histogram) with a Gaussian fit (solid line), panel a, and the coupling intensity $\langle |V_{kv}|^2 \rangle$ for those same basis states $|k\rangle$ in the middle of the spectrum (histogram), as a function of $\omega = E_v - \bar{E}_k$, panel b; dots correspond to the constant value of $\langle |V|^2 \rangle = 0.147$ MeV².

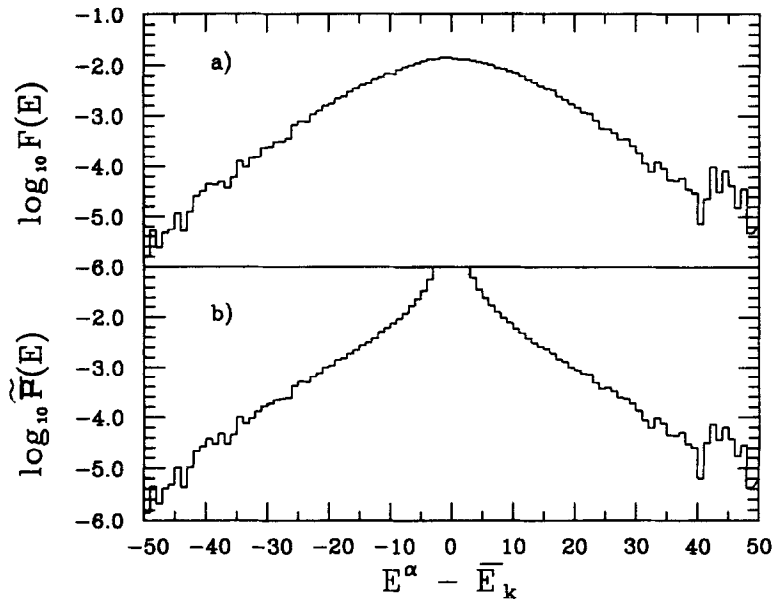


Fig. 52. Strength function $F_k(E)$ (panel a) compared with the perturbative result $\tilde{F}_k(E)$ (panel b) from Eq. (87). The bin size is 1 MeV.

the quantities

$$W_k^v = \left(\frac{V_{kv}}{\bar{E}_k - E_v} \right)^2 \quad (87)$$

are close to W_k^a . Fig. 52 shows, on a detailed logarithmic scale, that the peripheral region of the strength function, Fig. 50(a), agrees with the results of perturbative calculations. Perturbation theory is valid outside the central region of the order of the spreading width.

6. Chaoticity versus thermalization

We saw that the complicated wave functions representing exact stationary states in the shell-model with a finite Hilbert space display the conventional signatures of quantum chaoticity. The global level statistics are similar to those of the GOE. Local level correlations reveal Wigner repulsion. The spectra are rigid with no pronounced contribution from periodic orbits. The independent partition structure is significantly smeared, the stationary eigenstates are delocalized in Hilbert space and their information entropy (56) calculated in the original shell-model basis is close to the GOE limit. These signatures taken together give clear evidence that our system, at least the part of the spectrum located in the middle of the energy range, is near the stochastic limit. Along with this, there exists a noticeable change of the degree of complexity as a function of the excitation energy and level density.

In the usual description of excited states at high level density, the thermodynamic picture of a heated system is frequently used. The question arises [102]: what is the relation between the complicated structure of exact eigenstates and general principles of equilibrium statistical mechanics? To address this question we first discuss the general notion of statistical equilibrium as applied to an isolated mesoscopic system like a nucleus.

6.1. Thermal equilibrium in a small closed system?

The standard approach to the statistical description of a closed equilibrated system with a sufficiently high number of degrees of freedom implies that average (“thermodynamic”) properties of the system are determined by its statistical weight $\Omega(E) = \rho(E)\delta E$, i.e. by a number of states with given values of exact integrals of motion within the energy range δE . The latter is defined by the uncertainty of the total energy E due to the initial conditions, finite duration of preparing the system, interaction with the surroundings or just due to the lack of information. The exact value of δE is not important as long as δE is small compared to the energy interval where the macroscopic properties of the system change considerably. Since the density of states $\rho(E)$ grows very fast (exponentially in the thermodynamic limit of macroscopic systems) with energy E , the interval δE can still contain many levels which makes the concept of the smooth level density meaningful.

Having introduced the statistical weight, one can proceed to define thermodynamic entropy $S^{\text{th}}(E) = \ln \Omega(E)$ and temperature T according to

$$\partial S^{\text{th}}/\partial E = 1/T. \quad (88)$$

Obviously, this concise description corresponds to the minimum information available. In fact, our knowledge of the microscopic state of the system at equilibrium is limited to what is given by exact integrals of motion.

In a situation with incomplete information, a quantum system is described by the density matrix \mathcal{D} rather than by the pure wave function. Given the density matrix, the expectation value of an observable \mathcal{O} can be found as an average, $\langle \mathcal{O} \rangle = \text{Tr}(\mathcal{O}\mathcal{D})$. For a closed system, the only possible assumption about the *a priori* distribution of probabilities for the system to be found somewhere within δE is that the density matrix is a constant equal to $1/\Omega(E)$ inside the energy interval and zero outside. This is the usual way to introduce the microcanonical ensemble for the closed system and further proceed to the canonical or grand canonical ensemble for a subsystem of the closed system. All ensembles are equivalent for large systems in predicting thermodynamic properties but differ in defining the fluctuations. The canonical ensembles can be derived from the maximum of entropy

$$S = -\text{Tr}(\mathcal{D} \ln \mathcal{D}) \quad (89)$$

under additional constraints specified for a given ensemble.

The overwhelming accuracy of the statistical approach implies that the results are absolutely insensitive to the actual microscopic state of the system. It is repeatedly stressed in the textbook on statistical mechanics by Landau and Lifshitz [103] that average over the equilibrium statistical ensemble should give the same outcome as an expectation value for a typical stationary wave function at the same energy. The main underlying assumption is that of similarity of generic wave functions in a given energy region. At the same time, equilibrium statistical averaging discards all

possible phase relationships between different components of wave functions: one deals entirely with probabilities (diagonal elements of the density matrix in the energy representation). This is justified if the phase coherence can appear with a very low statistical weight only.

If we start with a highly coherent state, for example, as in a heavy ion collision where the entire excitation energy is initially concentrated in global synchronized motion of all constituents, this is, as a rule, a wave packet rather than a stationary state. We need to wait for some time to allow for the time evolution to destroy the initial coherence. In general the decoherence does not require the presence of the surrounding. It is sufficient to couple different degrees of freedom inside the system. The process of decoherence, called relaxation or equilibration, is practically irreversible because of the finite lifetime with respect to the decay into the continuum or the extremely long recurrence time for the revival of phase coherence in the case of the discrete but very dense spectrum. However, it does not necessarily mean that full statistical equilibrium requires “that each states included in $\rho(E, N)$ be populated with equal probability” [104]. The point is that the vast majority of states in the region of high level density reveals very similar observable properties, so that the exact distribution of population probabilities among the close stationary states is not important. This is the microscopic counterpart for the second law of thermodynamics and the trend of entropy to the maximum value. Once the phase coherence is destroyed, the details of microscopic population become simply irrelevant for the macroscopic observables which corresponds to the maximum loss of information. The equiprobable microcanonical ensemble is just the simplest choice which gives correct results.

In some cases, as in slow neutron scattering, the uncertainty interval δE may shrink in fact to a single intrinsic state. A rather precise knowledge of energy is crucial for the scenario [29] of parity nonconservation in fission by polarized neutrons. However, it does not prevent one from using thermodynamic concepts for the description of the structure of a specific neutron resonance in terms of thermal particle–hole excitations [105]. The optical model average over the resonances implies their similarity rather than actual equipopulation. One does not need to explore the whole set of similar states to obtain statistically reliable information merely due to this similarity of the individual wave functions.

6.2. *Statistical equilibrium and stochastic dynamics*

Now we discuss briefly under which circumstances one can expect the majority of stationary states in a given small energy range to reveal analogous observable properties.

The picture of the exceedingly large amount of states with very similar macroscopic features is obviously valid for perfect gases. One can easily see that the description of Section 6.1 of the equilibrium ensemble fits as well our limit of stochastic dynamics. In the classical case the correspondence between statistical equilibrium and chaotic trajectories exploring the whole energy surface is taken almost for granted by many authors, see for example [106]. As for the quantum case, the pioneering paper on the compound nucleus by Niels Bohr [31] already gives an equal footing to elements of both patterns, chaos and thermalization. The definition by Percival [36] of chaotic wave functions goes along the same line, stating that all of them look almost similar, covering more or less uniformly the entire available region of configuration space. According to Berry [95, 107], in systems with the chaotic classical limit as a gas of hard spheres, the eigenfunctions should behave like random superpositions of plane waves. This conjecture is actually

equivalent to the statistical microcanonical ensemble and directly leads [108] to the standard (Maxwell–Boltzmann, Bose–Einstein or Fermi–Dirac) momentum distribution functions for individual particles.

One can argue that the gas of hard spheres is a particular case of many-body dynamics where the interaction is reduced effectively to the exclusion of the inner volume of the spheres. This allows one to rigorously prove the conditions for chaoticity of the corresponding classical gas [109]. In fact, the onset of chaos in such a gas occurs at temperatures which are high enough to diminish a thermal De Broglie wave length of a particle to become less than the radius of the sphere. This ensures instability of classical scattering with respect to small variations of the impact parameter. The picture of chaos arising from the irregular scattering is literally applicable to the low density gas only when the interaction proceeds via rare pairwise collisions. However, long ago it was shown by van Hove [110] that a much broader class of gas-like systems displays quantum ergodicity. A random initial wave function of such a system evolves with time into a state which gives the same values of observables as the microcanonical thermodynamic ensemble. The assumption of randomness (phase incoherence of the components) is similar to Berry's conjecture or even to Boltzmann's molecular chaos (*Stosszahlansatz*).

Self-sustained Fermi systems like nuclei behave, according to the Landau–Migdal theory of Fermi liquids, analogously to the gas of interacting quasiparticles. Empirical nuclear level densities are reasonably well described by slightly modified Fermi gas formulae. The effective residual forces used in the shell-model calculations should be considered a phenomenological result of renormalizations, taking into account the hard-core – or more precisely – short-range part of the original nucleon–nucleon interaction, and the necessary truncation of fermionic space. The residual interaction cannot be totally reduced to rare pairwise collisions and is to be treated on exact quantum-mechanical basis. Therefore there is no clearly defined transition to the classical limit and the direct generalization of the results derived for hard spheres is hardly possible.

Having at our disposal exact eigenfunctions of the Fermi system with strong interaction (although in a truncated space), we can compare their statistical properties with those of the equilibrium statistical ensemble. As discussed earlier, one can imagine two opposite situations: (i) adjacent states with very close energies which nevertheless have nothing in common in their structure so that their proximity is a matter of accidental degeneracy; (ii) neighboring states can be considered as a final stage of the mixing process which results in the stochastization and similarity of structure. Only option (ii) corresponds to the idea of the equilibrium ensemble.

We have seen in Section 4 that the degree of complexity measured by information entropy of individual functions in the shell-model basis is the same for many states close in energy. Within small fluctuations, it changes smoothly with excitation energy, and therefore can be treated as a thermodynamic variable. A similar conclusion is valid for more refined measures like the distribution function of the components, Section 5. This gives a strong indication of the equilibrium mixing. It will be shown that under certain conditions a direct correspondence exists between information entropy and thermodynamic entropy. Another question to be addressed is the relationship between the actual wave functions and the Fermi-liquid picture of the heated quasiparticle gas.

The shortcoming of the model comes from the same fact that makes the exact diagonalization feasible, namely a very small number of nondegenerate single-particle orbitals $|\lambda\rangle$. Still, we can draw some interesting conclusions.

6.3. Single-particle occupation numbers

First, let us consider the thermodynamic definition of entropy and temperature (88) which can be directly applied to our empirical level densities. As expected for a model with a finite Hilbert space, the system is increasingly heated as excitation energy increases until the level density reaches its maximum which corresponds to maximum entropy and infinite temperature. For the Gaussian level density $\rho(E)$ with the centroid at E_0 and variance σ_E^2 , the temperature (88), see Fig. 53 (solid lines), is

$$T = \sigma_E^2 / (E_0 - E) \quad (90)$$

while for the semicircle distribution (32) one would obtain $T = [a^2 - (E - E_0)^2] / (E_0 - E)$. The right half of the spectrum, $E > E_0$, is associated with decreasing entropy and negative temperature.

To compare the global thermodynamic behavior with the features of the individual eigenfunctions, we calculate the evolution of single-particle occupation numbers (the isoscalar monopole component of the single particle density matrix) n_λ^α of the orbitals $\lambda = (l, j)$ along the spectrum of stationary many-body states $|\alpha\rangle$,

$$n_{ij}^\alpha = \frac{1}{2} \sum_{m\tau} \langle \alpha | a_{ijm\tau}^\dagger a_{ijm\tau} | \alpha \rangle. \quad (91)$$

The results are shown in Fig. 54 where the panels *a–c* correspond to 0^+0 , 2^+0 and 9^+0 ($N = 657$) states, respectively. We observe a rather smooth regular change starting around the 20th level (in the atomic case [35] the fluctuations of the occupation numbers are considerably larger). This

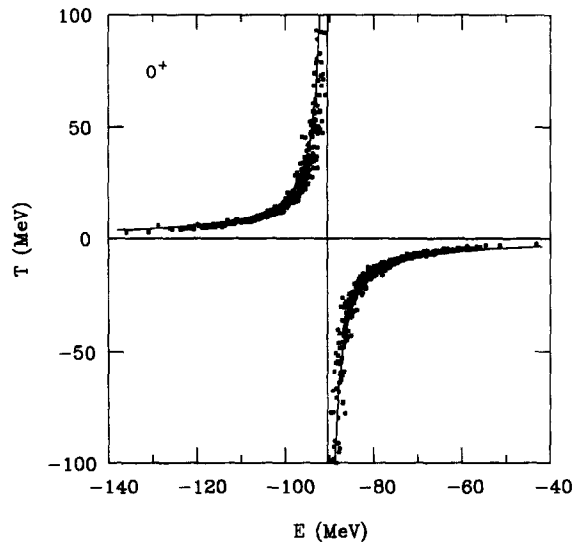


Fig. 53. Temperature calculated from the global fit to the level density of the 0^+0 states (solid line) and found from the occupation numbers of Fig. 54(a) (dots).

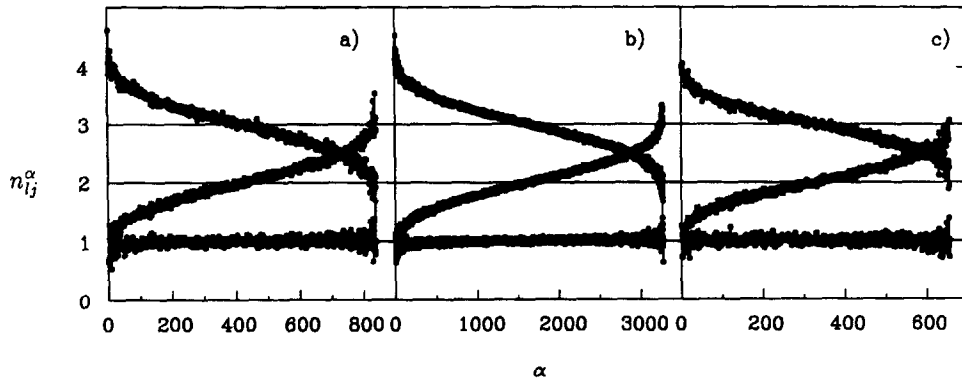


Fig. 54. Single-particle occupation numbers, Eq. (91), versus state number α for states 0^+0 (panel a), 2^+0 (panel b), and 9^+0 (panel c). For all panels the three curves (sets of points) refer to $s_{1/2}$, $d_{3/2}$ and $d_{5/2}$ orbitals, from bottom to top on the left-hand side.

smooth evolution takes place in spite of the fact that the states are orthogonal and apparently have no common dynamical character, as would be the case, for example, for members of a rotational band built on a given intrinsic configuration. The regular component of dynamics which survives averaging over extremely complicated wave functions is closely related to the mean field [40].

All three classes of states exhibit an identical average behavior of occupation numbers. It suggests that one can associate with each eigenstate $|\alpha\rangle$ a single-particle “temperature” T_{s-p}^α defined by the (grand canonical) Fermi distribution

$$f_{ij}^\alpha = \{ \exp[(e'_{ij} - \mu)/T_{s-p}^\alpha] + 1 \}^{-1}. \quad (92)$$

In the center of the spectrum where one expects infinite temperature, all occupancies $f_{ij}^\alpha = n_{ij}^\alpha/(2j + 1)$ indeed become equal to each other – the common value being one-half for our case of 12 particles in the sd-shell of the total capacity $\Omega = 24$.

T_{s-p}^α changes smoothly with energy, being almost the same for all complicated wave functions within the narrow energy interval as it should be for an intensive thermodynamic quantity. It becomes infinite simultaneously with the thermodynamic temperature (88) when the memory of the initial single-particle energies e_λ is lost.

The effective single-particle energies $e'_{ij} - \mu$ can be obtained from the slopes of the lines in Fig. 54. Assuming that the single-particle occupation numbers are described by Fermi statistics (92) with temperature T , their evolution along the spectrum is given by

$$df_\lambda/dT = f_\lambda(1 - f_\lambda)(e'_\lambda - \mu)/T^2. \quad (93)$$

The transition from the energy scale to the cumulative number (\mathcal{N}) scale used in Fig. 54 can be performed with the aid of Eq. (35) which is quite precise except for the very edges, Figs. 11 and 12. It determines $d\mathcal{N}/dT = (d\mathcal{N}/dE)(dE/dT)$ where the derivative dE/dT is found from (90). Finally

we come to the slope of the lines of Fig. 54 in the \mathcal{N} -scale,

$$\frac{df_\lambda}{d\mathcal{N}} = \frac{4a_c}{\pi N \sigma_E^2} \frac{e'_\lambda - \mu}{\cos[\pi(E - E_0)/2a_c]} f_\lambda(1 - f_\lambda). \quad (94)$$

Therefore the slope of lines is directly related to $(e'_\lambda - \mu)$. Near the middle of the spectrum all occupation numbers are close to $f_\lambda = \frac{1}{2}$, and we have a constant slope

$$df_\lambda/d\mathcal{N} = (a_c/\pi N \sigma_E^2)(e'_\lambda - \mu). \quad (95)$$

The resulting effective single-particle energies $e'_{ij} - \mu$ are -3.4 , 0.0 and 4.7 MeV for $d_{5/2}$, $s_{1/2}$ and $d_{3/2}$ orbitals respectively (for comparison, the shell-model d-wave spin-orbit splitting near the ground state is 7.2 MeV). The same results can be derived with a straightforward overall fit.

Using these energies, one can now extract the effective temperature T_{s-p}^α , Eq. (92), and check, with the aid of the actual occupation numbers f_λ^α for each level $|\alpha\rangle$, Fig. 54, that, despite the strong interaction, the “single-particle thermometer” on average measures the same temperature as T obtained from the level density.

These results imply that the system can be considered as an equilibrated Fermi-liquid, and its properties can be expressed in terms of occupation numbers for a gas of interacting quasiparticles. They move in the effective mean field with orbital energies e'_{ij} which in our case are just slightly different from the bare energies e_{ij} . Note that we deal exclusively with the exact eigenstates performing no ensemble averaging. In accordance with our understanding of statistical equilibrium, the eigenfunctions individually show the same distribution of occupancies as one would expect from statistical mechanics of the thermal ensemble described by the equilibrium density matrix.

The microscopic mechanism of equilibration can be understood from the fragmentation of the projected shell-model states $|J^\pi T; k\rangle$. Applying the recipes of statistical spectroscopy [53], one can explain the approximately constant occupation of the $s_{1/2}$ orbital and the smooth evolution of occupation factors for $d_{3/2}$ and $d_{5/2}$ orbitals as a function of excitation energy. An artificial reduction by a factor 10 of the diagonal matrix elements implies (Fig. 55) constancy of occupation numbers (vanishing heat capacity).

We conclude that the thermodynamics of the system are determined mainly by the stabilizing action of the mean field. Using the mean field basis we are able to segregate the incoherent processes leading to stochastization and local chaos from the regular evolution along the spectrum. The stochastic part of the dynamics is responsible for the complexity of the eigenfunctions and their similarity, which can be interpreted in terms of thermal equilibrium. The regular (mean field) features allow us to use a simple language of average occupation numbers for quasiparticles in a heated Fermi liquid.

As was shown in our discussion of the characteristics of complexity, Section 4, a certain level of self-consistency between the mean field and the residual interaction is necessary in order to reach the optimal separation of local and global features. In the shell-model calculations it is ensured by the semiempirical construction of the hamiltonian. Only in this case we can expect a strong correlation between the standard thermodynamical entropy (lack of information about the precise microscopic state of the system) and information entropy (disorder of a given microscopic state computed in the mean field basis of simple quasiparticle configurations). A direct comparison indeed reveals such a correlation.

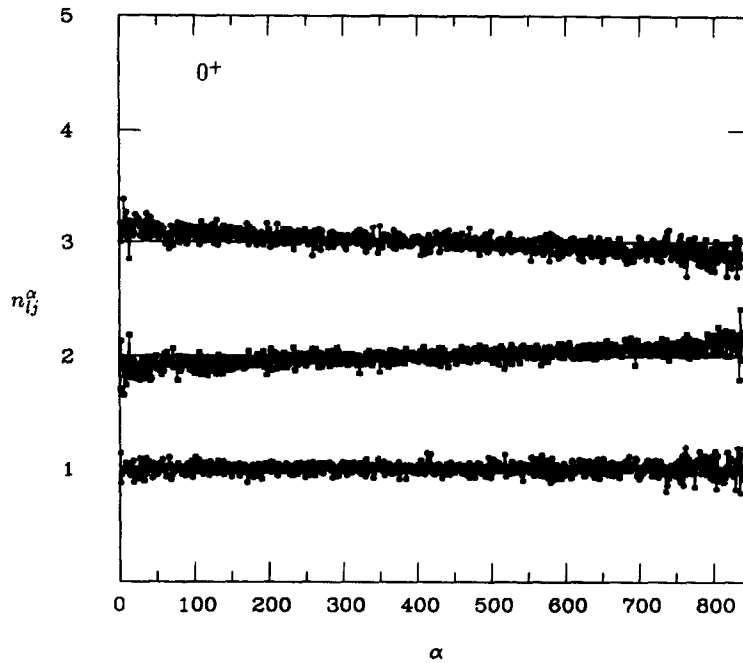


Fig. 55. Single-particle occupation numbers for 0^+ states for diagonal matrix elements reduced by a factor 10 as compared to Fig. 54(a).

6.4. Complexity and thermalization

Using the occupancies f_{ij}^α of individual orbitals one can calculate the single-particle entropy of the quasiparticle gas [103] for each state $|\alpha\rangle$,

$$S_{s-p}^\alpha = - \sum_{ij\tau} (2j + 1) [f_{ij}^\alpha \ln f_{ij}^\alpha + (1 - f_{ij}^\alpha) \ln (1 - f_{ij}^\alpha)] . \quad (96)$$

The expression (96) comes from the Fermi-gas combinatorics. The maximum of the entropy, as a functional of occupation numbers at given average energy and total particle number, again leads to the Fermi–Dirac distribution function (92).

Now we have three, apparently different, entropy-like quantities: thermodynamic entropy $S^{\text{th}}(E) \sim \ln \rho(E)$, information entropy S^α (56) and single-particle entropy S_{s-p}^α (96), the latter two for individual eigenstates. In Fig. 56 we juxtapose the energy behavior of $\exp(S)$ for different physical situations, I, II and III (columns). Rows *a*, *b* and *c* present S^{th} , S^α and S_{s-p}^α , respectively, for 0^+ states.

Column I of Fig. 56 shows the limit of a relatively weak off-diagonal interaction (the diagonal matrix elements are amplified by a factor 10). The thermodynamic entropy *Ia* displays Gaussian behavior of a combinatorial nature typical for a slightly imperfect Fermi-gas in a finite number of states. Within the fluctuations related to the transition from the microcanonical to grand canonical ensemble, it is quite similar to the single-particle picture *Ic*. The information entropy *Ib* is low; only at high level density does one see some effects of mixing. This is an equilibrium picture of almost

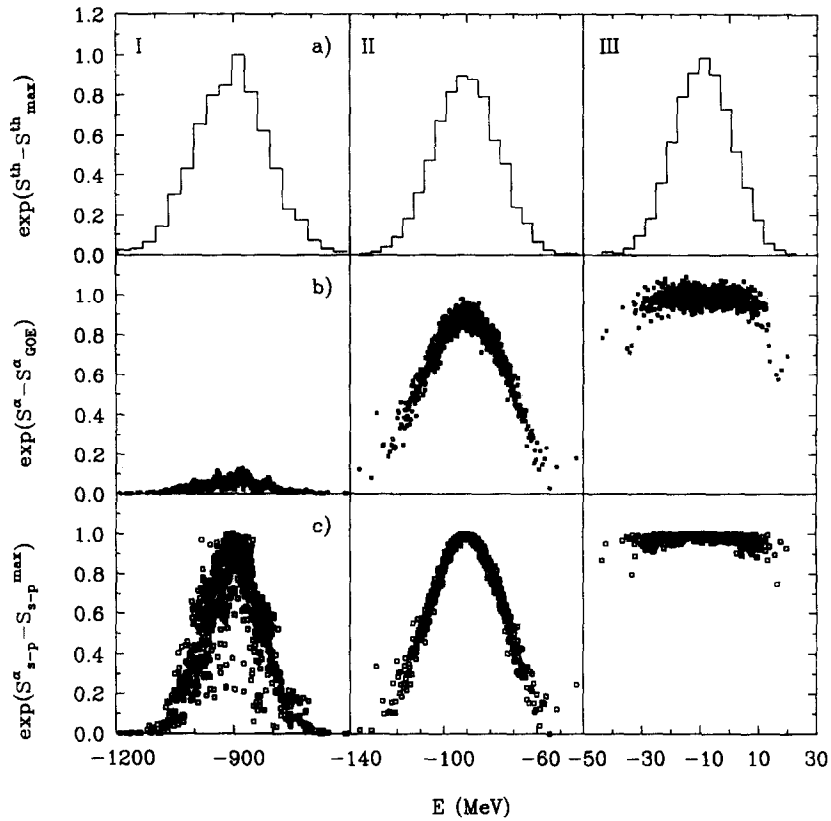


Fig. 56. Entropy-like quantities plotted as a function of energy for 0^+ states. Columns correspond to the diagonal matrix elements multiplied by factors of 10 (I), 1 (II) and 0.1 (III); the latter case coincides with that of Fig. 55. Rows *a*, *b* and *c* correspond to (a) the total statistical weight $\Omega(E)$ in units of the weight for the middle of the spectrum; (b) information entropy, Eq. (56), of individual states in units of the GOE entropy for the complete mixing, $\exp(S_{\text{GOE}}^\alpha) = 0.48N$; and (c) single-particle entropy, Eq. (96), of individual states calculated from the occupation numbers, in units of $S_{s-p}^{\alpha, \text{max}} = 2^{24}$, respectively.

noninteracting particles where the degree of complexity given by the information entropy, is only weakly correlated with thermalization. Using the language of kinetic theory, collisions (mixing) are necessary for equilibration but the equilibrium properties do not depend on the collision rate.

The opposite case III corresponds to a strong off-diagonal interaction (as in Fig. 55, the diagonal matrix elements are reduced by a factor 10). Almost all states are strongly mixed and the information entropy IIIb is near its chaotic maximum (Section 4.2) of $\exp(S^\alpha)_{\text{chaotic}} = 0.48N = 404$ for 0^+ states. S_{s-p}^α (IIIc) is also at the maximum level corresponding to the equiprobable population of orbitals. Within the fluctuations, S^α and S_{s-p}^α coincide. However, as seen from IIIa, the system has normal thermodynamic properties governed by the level density.

Thus, in the absence of the (diagonal) mean field (column III), the response to thermal excitation cannot be expressed in terms of quasiparticles. In both cases (I and III) the information entropy becomes irrelevant for thermodynamics, although it still characterizes degree of complexity of eigenstates in the mean field basis.

The case of the realistic mean field and empirical residual interaction is shown in column II. With the normalized magnitudes, all three entropies are identical within fluctuations except for the edges of the spectrum. Near the ground state the Fermi surface is already smeared due to two-body correlations. In particular, pairing effects are considerably stronger as we illustrate in Section 7. For the low-lying states the single-particle occupation numbers and information entropy show deviations from the frozen Fermi-gas. The difference between low thermodynamic temperature and single-particle temperature, as measured for instance in particle knockout experiments near the ground state, was discussed in [40]. For the majority of states and for the mean field consistent with residual interactions, the thermodynamic entropy (defined either via the global level density or in terms of occupation numbers) behaves similar to information entropy.

6.5. Discussion

One can conclude that (i) equilibrium heating is correlated with the evolution of “many-body” chaos and the increase of complexity of individual eigenstates; (ii) equilibrium properties of a heated system with strong interactions can still be described in terms of quasiparticles and their effective energies in the appropriate mean field (this opens the way for explicit calculation of matrix elements between compound states [105]).

Let us stress the special role of the mean field representation [40] both for studying the degree of chaoticity of specific wave functions (Section 4) and for the statistical description. With the artificially depressed or enhanced diagonal matrix elements, the level density and the thermodynamic entropy S^{th} are qualitatively the same as in the realistic case (Fig. 56(a)). As discussed in Sections 2 and 3, the off-diagonal residual interaction, apart from a possible overall shift, merely widens the level density – keeping its Gaussian shape which is determined mainly by combinatorics.

However, with no mean field (Fig. 56 (III)) the increase of complexity measured by the S^{α} and the mixing of quasiparticle configurations measured by the $S_{\text{s-p}}^{\alpha}$, going together, are different from the heating measured by the level density and the “normal” entropy S^{th} . The interaction is too strong and the mixing does not depend on the actual level spacing. Almost all wave functions “look the same” regardless of level density, and the quasiparticle “thermometer” cannot resolve the spectral regions with different temperatures. In this case only the microcanonical description is possible.

At this point we would like to give a more formal argument in favor of the direct correspondence between information entropy and thermalization. The density matrix \mathcal{D} used for the description of a quantum system with reduced information has, in an arbitrary many-body basis $|k\rangle$, matrix elements $\mathcal{D}_{kk'} = \overline{C_k C_{k'}^*}$ where the amplitudes are averaged [103] over the ensemble. If the ensemble is generated by interaction with the environment, the states of the entire system are $|k; e\rangle$, where e labels the states of the environment compatible with the state $|k\rangle$ of the subsystem under study. Then

$$\mathcal{D}_{kk'} = \sum_e C_{k;e} C_{k';e}^* . \quad (97)$$

The corresponding statistical entropy, Eq. (89), is basis independent and equals zero for pure states of the isolated subsystem. For canonical equilibrium ensembles, S coincides with the thermodynamic entropy.

Let us consider a gas of quasiparticles in the ensemble generated by the residual interaction. This makes sense only after proper separation of global smooth dynamics from quasirandom incoherent processes. Such a separation defines the optimal basis, namely that of the self-consistent mean field [40] (our “simple” states $|k\rangle$). Compound states $|\alpha\rangle$ mimic the “total” system (quasiparticles + interaction field). The intrinsic interaction is responsible for decoherence and formation of the thermal ensemble of quasiparticles. The ensemble average of $\mathcal{D}_{kk'} = \overline{C_k^\alpha C_{k'}^\alpha}$ is to be taken over neighboring states $|\alpha\rangle$. If the amplitudes C_k^α are uncorrelated and all neighboring states $|\alpha\rangle$ are similar, only diagonal elements of $\mathcal{D}_{kk'}$ survive and we come to the information entropy (56). In quite a different context similar arguments were discussed by Elze and Carruthers [111].

The simplest example when such a statement is exact is given by the equilibrium gas of Bose-quanta as black-body radiation. A weak interaction with the environment or between quanta is needed only for relaxation towards the equilibrium. The “natural” basis $|k\rangle$ is that of the states with a certain number of quanta k of each mode. The modes are independent so that it suffices to consider a single mode. To characterize the macroscopic properties of a stationary state $|\alpha\rangle$, we fix the average number \bar{k} of quanta. The maximization of information entropy S^α with respect to the weights W_k^α for given $\bar{k} = \sum_k k W_k^\alpha$ is known [103] to lead to the normalized distribution $W_k^\alpha = \bar{k}^k / (\bar{k} + 1)^{k+1}$. For the mode with single-particle energy ε , this is nothing but the thermal Planck distribution for temperature $T = \varepsilon [\ln(1 + 1/\bar{k})]^{-1}$. The value of information entropy at maximum coincides with the thermodynamic value for this temperature. However it is useful to stress again that in our case we deal with a strongly interacting system.

7. Pairing correlations and stochastization

As discussed in Section 5.5, the residual interaction induces, along with incoherent collision-like mixing, processes corresponding to ordered regular modes of excitation. Table 1 showed that the large matrix elements of the residual interaction are mostly negative. The diagonal part, including the high-order contributions (for example virtual pair transfer), is responsible for the attractive interaction which shifts down the center of gravity of the whole spectrum. The off-diagonal part generates the excitations of coherent type.

Leaving for the future the detailed studies of the collective phenomena in the model, we illustrate the general trends by an example of primary practical importance. Significant effects of the pairing correlations of superconducting type are seen throughout the periodic table. From the microscopic point of view, they are caused by the enhanced attractive matrix elements of the two-body residual interaction $\langle (j_2^2)_{j=0} | V | (j_1^2)_{j=0} \rangle$ corresponding to the self-energy of the monopole pair or to the coherent pair transfer between the orbitals. This is clearly visible in our semiempirical hamiltonian, Table 1.

To treat the pairing correlations in macroscopic systems or in heavy nuclei, the BCS or Hartree–Fock–Bogolyubov (HFB) approximations are used when this part of the interaction is substituted by the average pairing field [21] which serves as a source for pair creation and annihilation. It can be improved by the particle number projection. The phase transition destroying superconductivity can be recognized by the disappearance of the mean pairing field. In our model space we have the exact eigenfunctions which contain all interaction effects including pairing

with the conservation laws strictly fulfilled. Therefore we do not need any additional approximations.

We analyze the energy spectrum and the wave functions to look for the microscopic signatures of the pairing correlations. Our advantage is the possibility to study all individual eigenstates and from their comparison to draw conclusions about quenching of correlations with excitation energy. Here it is worthwhile to mention that global characteristics such as the total level density are not very sensitive to subtle effects such as the possible local enhancement near the threshold $E \approx 2\Delta$ of Cooper pair breaking. In the BCS model the two-quasiparticle levels are pushed out of the energy gap 2Δ and accumulated at the threshold with the (integrable) singularity of $\rho(E) \propto (E^2 - 4\Delta^2)^{-1/2}$. Our “empirical” level densities, Figs. 11–14, show only slight irregularities in the low-energy region. The irregularities are small (compared to schematic models, see for example [112]) due to the small number of pairs in the condensate. The effect in the total level density is smeared by exact fulfillment of the conservation laws and by incoherent parts of the interaction, absent in the schematic models, which rapidly increase the degree of complexity of the eigenstates. But the smoothness of the level density does not contradict the existence of pairing correlations.

We select as a probe the operator

$$\mathcal{H}_P = (P^\dagger \cdot P) \equiv \sum_{t=0, \pm 1} P_t^\dagger P_t \quad (98)$$

where the isovector pair annihilation (P_t) and creation (P_t^\dagger) operators with the isospin projection t are defined in terms of fermion operators $a_\lambda \equiv a_{j_m t}$ and a_λ^\dagger according to

$$P_t = \frac{1}{\sqrt{2}} \sum_{ij} [\tilde{a}_{ij} \tilde{a}_{ij}]_{J=0, T=1, T_3=t}, \quad P^\dagger = \frac{1}{\sqrt{2}} \sum_{ij} [a_{ij}^\dagger a_{ij}^\dagger]_{J=0, T=1, T_3=t}. \quad (99)$$

Here the sums are taken over all single-particle orbitals lj . For each a_λ the time conjugate operator is defined as $\tilde{a}_\lambda = (-)^{j-m} a_{lj-m}$. We use here the isospin invariant $T = 1$ pairing which is suitable for light nuclei with neutrons and protons occupying the same orbitals. The actual calculation of the expectation values $\langle \mathcal{H}_P \rangle$ is facilitated by the fact that it can be considered as a specific residual interaction with the two-body matrix elements $\langle (j_2^2)_{JT} | V_P | (j_1^2)_{JT} \rangle = [(2j_1 + 1)(2j_2 + 1)]^{1/2} \delta_{J_0} \delta_{T_1}$.

In the BCS or HFB theory the mean pairing field is given by the nonvanishing (“anomalous”) expectation values of the operators P and P^\dagger in the trial ground state, which is a coherent packet of states with different particle numbers. These expectation values are proportional to the energy gap and vanish together with the latter at the phase transition. In our case the diagonal elements of the operators (99) over exact stationary states indentially vanish, and the pair operators (99) characterize the strength of the pair transfer to the neighboring nuclei. However the expectation value of the bilinear operator (98) gives the total strength for all transitions from an initial state induced by the monopole pair transfer (analog of a sum rule).

We have calculated the expectation value of \mathcal{H}_P for all individual 0^+0 states in two systems, 8 valence particles in ^{24}Mg ($N = 325$ states) and 12 valence particles in ^{28}Si ($N = 839$). The results are shown in Figs. 57(a) and (b), respectively.

The qualitative picture is the same in both cases. At low excitation energies the states have considerably higher value of $\langle \mathcal{H}_P \rangle$ than the states in the middle of the spectrum. This value drops very fast into a long smoothly decreasing tail. Only a relatively small number of states display

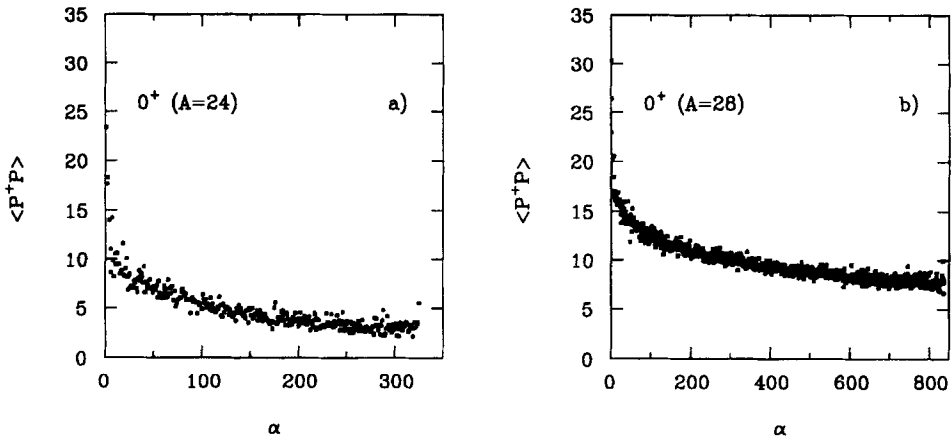


Fig. 57. Expectation values $\langle \mathcal{H}_P \rangle$ of the operator (98) (dots) for all 0^+ states of $A_v = 8$ articles (^{24}Mg), panel a, and $A_v = 12$ particles (^{28}Si), panel b.

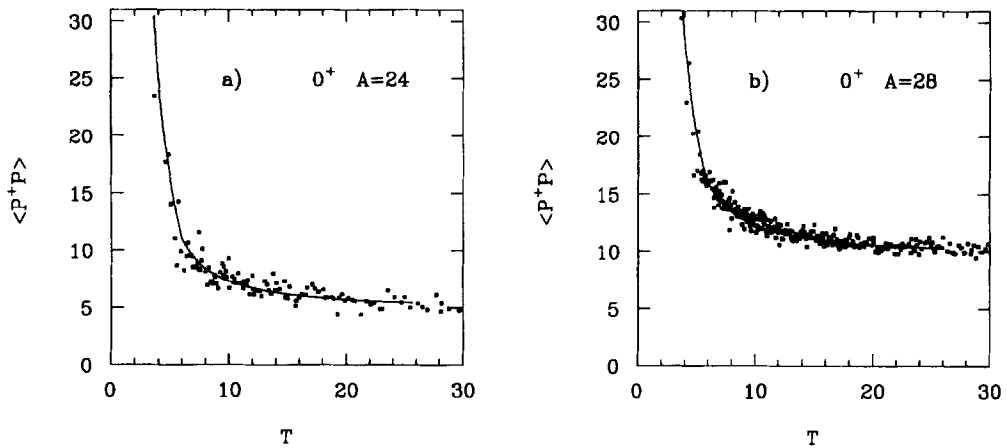


Fig. 58. Expectation values $\langle \mathcal{H}_P \rangle$ of the operator (98) as a function of thermodynamic temperature (dots). The solid lines correspond to the fit given by Eqs. (100)–(102) with parameters of Table 3.

strong enhancement of $\langle \mathcal{H}_P \rangle$. The majority of states have approximately the same nonzero value of this quantity. Similar to what we have observed for other characteristics of individual eigenstates, the fluctuations of $\langle \mathcal{H}_P \rangle$ are small, especially in the case of 12 particles, so that practically one can consider (98) as a function of excitation energy or temperature.

Looking through a magnifying glass at the initial part of Fig. 57(b), we see, Fig. 58, more distinctly the presence of two components – fast and slow – which differ in the rate of decrease. The fast component can be related to the thermal depletion of the pair condensate and the Pauli blocking of the pair transfers by the broken pairs. In a small system this region covers a small fraction of all states only. However, the pairing correlations do not abruptly disappear; they still

slightly exceed the background level $\bar{\mathcal{H}}$ which can be inferred from the middle part of the spectrum. We can interpret this part as evidence of pairing fluctuations which are enhanced near the phase transition and survive long after the static superconducting condensate is destroyed.

The simple fit to the observable energy dependence of Figs. 57 and 58 is given by

$$\langle \mathcal{H}_P \rangle = \bar{\mathcal{H}} + \mathcal{H}_c(E) + \mathcal{H}_{fl}(E) \tag{100}$$

where $\mathcal{H}_c(E)$ represents the condensate contribution and $\mathcal{H}_{fl}(E)$ corresponds to the pairing fluctuations. These effects, in turn, can be described as

$$\mathcal{H}_c(E) = A \frac{1 - (E/E_c)}{1 - (E/E_0)} \theta(E_c - E), \tag{101}$$

$$\mathcal{H}_{fl}(E) = B \exp[-(E - E_c)/w]. \tag{102}$$

The condensate (101) disappears at $E = E_c$, or, for the Gaussian temperature scale (90), at $T = T_c = \sigma_E^2/(E_0 - E_c)$. For the order parameter $\Delta \propto \sqrt{\mathcal{H}_c}$ the parameterization (101) gives the behavior

$$\Delta = \Delta_0 \sqrt{1 - \frac{T}{T_c}} \tag{103}$$

typical for the second-order phase transition in the mean field approximation [103]. The constant term $\bar{\mathcal{H}}$ describes the background value which would exist even with no attractive interaction in a normal Fermi gas. The fits for the case of ^{24}Mg and ^{28}Si are shown as a function of temperature T in Fig. 58. We see a clear signature of the phase transition in a small system. Of course, it is possible to recognize it only due to the fact that we are able to compare the properties of all individual eigenfunctions.

Table 4 shows the best fit parameters E_c , its translation into the Gaussian temperature scale T_c , the condensate parameter A , the fluctuation range w , the fluctuation intensity at the transition point B , and the average background level $\bar{\mathcal{H}}$ both for the 8- and 12- particle cases.

The fluctuation term (102) can be presented as a function of temperature,

$$\mathcal{H}_{fl}(T) = B e^{-C_n(T - T_c)/T}, \tag{104}$$

where the specific heat related to the fluctuations of the pair condensate is

$$C_{fl} = \frac{\sigma_E^2}{wT_c}. \tag{105}$$

Table 4
The fitted parameters (in MeV) for the description of the energy dependent pairing correlation, Eqs. (100)–(102)

A_v	$\bar{\mathcal{H}}$	A	B	w	E_0	E_c	T_c
8	3.0	22.0	8.0	16.0	− 47.0	− 72.0	6.0
12	7.6	14.0	9.0	19.0	− 90.5	− 120.0	5.7

For our system of 12 particles, Eq. (105) with $T_c = 5.7$ MeV and $w = 19$ MeV, see Table 4, gives $C_{fl} = 1.6$, which is only a relatively small part of the total Fermi gas specific heat. The high quality of the exponential fit is shown in Fig. 59(a) (for $A = 28$) as a function of energy.

The average quantity (98) can be independently estimated in many ways. The maximum possible value of $\langle \mathcal{H}_P \rangle$ corresponds to the isospin invariant generalization [113] of the degenerate seniority model [114]. Operators P_i and P_i^\dagger , along with the isospin components, belong to the generators of the $\mathcal{O}(5)$ group which allows one to find the eigenvalues of \mathcal{H}_P . For the lowest $J = 0$, T state of A_v valence particles in Ω degenerate spin-spatial single-particle orbitals,

$$\langle \mathcal{H}_P \rangle_T = \frac{A_v}{4} (2\Omega + 6 - A_v) - T(T + 1) \quad (106)$$

where T is the total isospin of the many-body state. For the sd-shell with $\Omega = 12$ the case of $A_v = 12$ particles corresponds to $\langle \mathcal{H}_P \rangle_0 = 54$; for 8 particles one gets $\langle \mathcal{H}_P \rangle_0 = 44$, both numbers being too large. The pair condensate can be a good approximation only for the lowest states; but as we have seen in Section 5.3, the real structure of those states is far from that in the degenerate model being strongly determined by the single-particle energies in the mean field.

The average of the operator (98) over the whole Hilbert space (no restrictions by angular momentum or isospin) can be calculated with the help of the simple prescriptions of statistical spectroscopy [53],

$$\langle \mathcal{H}_P \rangle = \frac{3}{2(2\Omega - 1)} A_v(A_v - 1). \quad (107)$$

This estimate, $\langle \mathcal{H}_P \rangle = 8.6$ and 3.7 for $A_v = 12$ and 8 respectively, is to be compared to the background term \mathcal{H} in (100). The slight excess of the estimate (107) is partly due to the nonstatistical concentration of the pairing in the low energy states.

An estimate quite close to (107) can be obtained by taking the average of the operator (98) with the single-particle density matrix characterized by the occupation numbers f_λ . Assuming the time reversal symmetry of the occupancies, $f_{\bar{\lambda}} = f_\lambda$, and their identity for neutrons and protons, we obtain

$$\langle \mathcal{H}_P \rangle = 3 \sum_{ijm} f_{ijm}^2. \quad (108)$$

The equiprobable filling of all orbitals λ in the middle of the spectrum, $f_\lambda = 1/2$, $A_v = 12$, and $f_{\bar{\lambda}} = 1/3$, $A_v = 8$, leads to the values $\langle \mathcal{H}_P \rangle = 9$ and 4 respectively. The cooling of the system increases the occupancies of the lowest orbitals, and therefore gives higher values of $\langle \mathcal{H}_P \rangle$ than in the hottest middle region. This agrees with the increase of the fluctuational part (102) of the pairing to the edge of the spectrum.

For the sharp Fermi surface at $T = 0$, the occupation numbers are equal to 1 or 0, $f_\lambda^2 = f_\lambda$, and Eq. (108) would give $\langle \mathcal{H}_P \rangle = (3/2)A_v$. However in reality the Fermi surface is smeared by interactions including pairing. For the lowest states in the 12-particle case we have Fig. 54) the occupation numbers $f(d_{5/2}) \approx 2/3$, $f(s_{1/2}) \approx 1/2$, $f(d_{3/2}) \approx 1/4$. Then the estimate (108) gives $\langle \mathcal{H}_P \rangle = 10.25$. One can say that this part of the total value comes from the cooled Fermi gas, whereas the rest (for the low-lying states) is of dynamic origin due to the pairing forces. Fig. 59(b), solid line, shows the relation between the total pairing correlator and the single-particle effect (108)

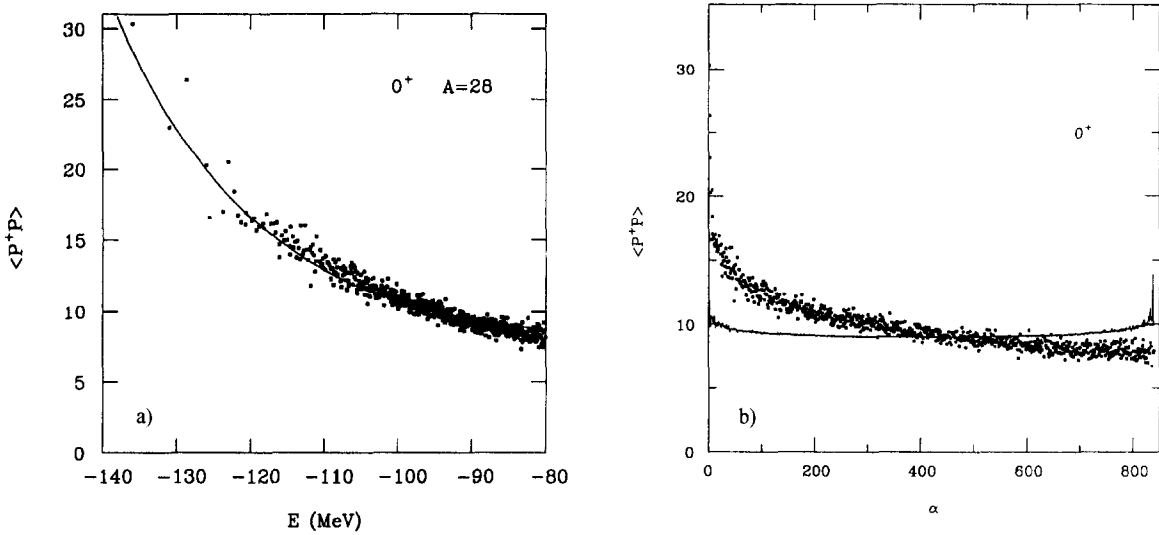


Fig. 59. (a) Comparison of the expectation values $\langle \mathcal{H}_p \rangle$ for the 0^+0 states (dots) and the Fermi-gas estimate (106) (solid line). (b) Comparison of the expectation values $\langle \mathcal{H}_p \rangle$ for the 0^+0 states of ^{28}Si , dots, and the Fermi-gas estimate (108), solid line.

calculated for the actual occupation numbers of Fig. 54(a) for the 0^+0 states of ^{28}Si . The pairing fluctuations of Eq. (108) are overestimated because they include unphysical fluctuations of the total particle number (as well as other integrals of motion J, M and T) which are present in the Fermi–Dirac distribution. An approximate estimate of the particle number fluctuation diminishes the quantity (108) by $(3/11) \sum_{l,jm} f_{l,jm}(1 - f_{l,jm}) \approx 0.8$.

8. Conclusions

We have reported the first results of the analysis of the eigenvalues and the eigenvectors of the nuclear shell model from the viewpoint of order, chaos, complexity and thermalization. We have tried to discuss the physical meaning of our findings in the corresponding sections and stressed their interplay and interrelationships. Certainly, many questions are only touched upon and they deserve further investigation. Below we briefly summarize our main conclusions with emphasis on the open problems.

(i) The nuclear shell model provides a realistic, exactly solvable example of a many-fermion system with strong interaction. The available dimensions are sufficiently high to allow for statistically reliable studies of the main features of the level statistics and structure of the wave functions.

(ii) The construction of the complete set of states with the given values of exact integrals of motion is an important prelude to the analysis. The role of this premixing and “geometrical chaoticity” is to be further studied.

(iii) The exponential distribution of the off-diagonal matrix elements of the residual interaction seems to be a generic feature of the realistic many-body systems. The origin of this distribution is not clear at this point and presents a theoretical challenge.

(iv) As excitation energy and level density increase, the local level statistics quickly reveal typical signatures of chaotic dynamics predicted by the GOE. This occurs even for a strength of the residual interaction much lower than its actual value.

(v) The interesting problem of the transitional nearest-level spacing distribution in the region of onset of chaos and the fractional power law for level repulsion remains to be solved.

(vi) The degree of complexity of stationary wave functions can be measured by the information entropy and the moments of the distribution function of the components. These measures depend on the representation which can be used to gain additional knowledge on the structure of the eigenvectors.

(vii) The mean field (spherical shell-model) basis appears to be the preferred representation which allows for the optimal separation of the local spectral properties from the global secular dynamics.

(viii) The structure of the wave functions presented in the mean field basis evolves in a very regular way along the spectrum. The measures of complexity can be considered as functions of the excitation energy; the accompanying fluctuations are small and decrease with the dimension of space increasing.

(ix) The distribution of the components of the eigenvectors in the shell model basis is close to Gaussian although the correlational analysis reveals deviations. The Gaussian variance (localization length, or number of principal components) increases along with excitation energy. However, the GOE limit of the complete delocalization can be reached by the majority of the eigenvectors only with an artificially suppressed stabilizing action of the mean field.

(x) The simple shell-model basis states are fragmented over the eigenstates with the strength function having a shape intermediate between the Breit–Wigner and Gaussian. The remote wings of the generic strength function display an exponential behavior characteristic for the localization. The actual value of the spreading width of basis states is larger than that given by the golden rule. As predicted by the theoretical arguments for the chaotic limit of dynamics, at smaller interaction strength, the validity of the standard model of the strength function is restored together with the golden rule and the Breit–Wigner shape.

(xi) The single-particle occupation numbers of the shell-model orbitals regularly evolve along the spectrum, being nearly the same for different classes of states. They can be described by the Fermi–Dirac distribution with effective energies close to the bare ones. The similarity of the wave functions and occupation numbers of the states close in energy can be interpreted in terms of statistical equilibrium.

(xii) In spite of the presence of strong interactions, the system behaves at high excitation energy as a heated Fermi gas of fermionic quasiparticles. This indicates the possibility of using the thermal ensemble for calculating matrix elements between the compound states. The apparent decoherence emerges here as a property of individual complicated wave functions in a closed mesoscopic system.

(xiii) Different definitions of temperature, related to the thermal microcanonical ensemble, single-particle occupancies, and information entropy, practically coincide for the mean field representation used in the last two cases, where the temperature scale is extracted for each individual eigenstate. It gives new arguments for understanding the foundations of quantum statistical mechanics and its relationship to quantum chaos.

(xiv) Collective correlations of the pairing type display a regular thermodynamic behavior with a smeared second-order phase transition into the normal phase. A long tail of pairing fluctuations is seen above the transition temperature. It would be interesting to study the matrix elements for the pair transfer between the individual states of the adjacent nuclides (the closest nuclear physics analog of the superconducting current).

(xv) The distributions of matrix elements of simple operators (primarily E2 and M1), rotational correlations and damping of rotational bands should be studied in the present framework. Here the exact fulfillment of the angular momentum conservation is very important.

(xvi) Another step of principal significance should be connected to the inclusion of continuum effects which can considerably modify all the conclusions. This will be of primary interest in application to unstable and loosely bound nuclei.

(xvii) An analysis along the same lines for different mass regions, different interactions and different truncation schemes will allow one to make fundamental conclusions concerning the onset of chaos and its interplay with thermalization and regular dynamics in nuclear matter. The extension to molecular systems, condensed matter and quantum field theory models seems very promising as well.

Acknowledgements

The authors acknowledge support from the NSF grant 94-03666. They are thankful to D. Kusnezov for help and cooperation in the problem of the correlations depending on parameters. The fruitful discussions at various stages of this work with A. Belič, G.F. Bertsch, G. Casati, P. Cvitanovic, V.F. Dmitriev, T. Døssing, V.V. Flambaum, Y.V. Fyodorov, M. Hjorth-Jensen, F.M. Izrailev, B. Lauritzen, B. Mottelson, W.E. Ormand, V.V. Sokolov, J. Wambach and S. Åberg are highly appreciated. V.Z. acknowledges support from the NSF grant 95-12831.

Appendix

Distributions of such type as (28) are typical for an ensemble of matrices with the factorizable elements. Let the matrix elements H'_{kl} of the residual interaction be modeled by a sum of separable terms

$$H'_{kl} = \sum_{\mu} (\pm)_{\mu} Q_k^{\mu} Q_l^{\mu} \quad (\text{A1})$$

similar to multipole–multipole forces. Here μ enumerates different “modes” of intermediate excitations. The additional factor $(\pm)_{\mu}$ in (A1) allows the diagonal terms H'_{kk} to be repulsive or attractive.

Among the actual multipoles there are those creating collective effects, first of all related to pairing (Section 7) and quadrupole deformation. Referring, as we did in Section 4.6, to the low statistical weight of collective states and the damping of collective modes in the stochastic region, we assume that the multipole matrix elements with different μ for the majority of states k and

l behave as random variables with zero mean and variance

$$\overline{Q_k^\mu Q_l^{\mu'}} = (1/\sqrt{N}) \delta^{\mu\mu'} \delta_{kl} h_k^\mu. \quad (\text{A2})$$

We use in (A2) the same normalization of the matrix elements, see Eq. (A6) below, which was discussed in connection to the Gaussian ensembles and the N -scaling, Eqs. (26) and (27). Due to the geometrical premixing in the basis states $|k\rangle$, we expect (A2) to be approximately valid after averaging over several states from the same partition. By the same reasoning the states $k \neq l$ supposedly give rise to uncorrelated multipoles.

The ansatz (A2) leads to the average matrix element of the hamiltonian (A1)

$$\overline{H'_{kl}} = (1/\sqrt{N}) \sum_{\mu} \tilde{h}_k^{\mu} \delta_{kl} \quad (\text{A3})$$

where the sign factors are included into $\tilde{h}_k^{\mu} = (\pm)_{\mu} h_k^{\mu}$. In this approximation, the off-diagonal matrix elements \tilde{H}_{kl} have zero mean. We assume that for the diagonal elements there is no abnormal cancellation between attractive and repulsive h_k^{μ} ; as seen from Table 1, the attractive diagonal elements prevail on the two-body level. It is convenient for the estimates to introduce the average magnitude \bar{h}_k and the effective number q of significant multipoles contributing to the sum over μ ,

$$\bar{h}_k \equiv (1/q) \sum_{\mu} \tilde{h}_k^{\mu}. \quad (\text{A4})$$

Then (A3) takes the form

$$\overline{H'_{kl}} = (q/\sqrt{N}) \bar{h}_k \delta_{kl}. \quad (\text{A5})$$

To estimate the matrix elements of the off-diagonal part \tilde{H} , we assume, according to the general philosophy of random matrices [7] that the main contribution comes from the pairwise contractions (A2) of the multipoles Q_k^{μ} . Then we arrive at the correlation function of the matrix elements

$$\overline{H'_{kl} H'_{k'l'}} = \frac{1}{N} \left\{ \delta_{kl} \delta_{k'l'} \sum_{\mu} \tilde{h}_k^{\mu} \sum_{\mu'} \tilde{h}_{k'}^{\mu'} + (\delta_{k'k} \delta_{l'l} + \delta_{k'l} \delta_{l'k}) \sum_{\mu} h_k^{\mu} h_l^{\mu} \right\}. \quad (\text{A6})$$

The fluctuations of the diagonal elements are statistically small,

$$\overline{(H'_{kk})^2} - (\overline{H'_{kk}})^2 = (2/N) \sum_{\mu} (h_k^{\mu})^2 \equiv (2q/N) \bar{h}^2. \quad (\text{A7})$$

The correlation of diagonal and off-diagonal matrix elements vanishes,

$$\overline{H'_{kk} \tilde{H}_{ll'}} = 0. \quad (\text{A8})$$

The correlator of the off-diagonal elements is of the same order as (A7). It can be written in the form analogous to that for the banded ensemble (48),

$$\overline{\tilde{H}_{kl} \tilde{H}_{k'l'}} = (1/N) (\delta_{k'k} \delta_{l'l} + \delta_{k'l} \delta_{l'k}) \sum_{\mu} h_k^{\mu} h_l^{\mu}. \quad (\text{A9})$$

The natural correspondence between the parameters of (A9) and the radius a and the form-factor $\eta_{kl} \approx \eta(|k - l|)$ of the BRM ensemble (48) can be established via identification

$$a^2 = 4q\bar{h}^2, \quad \eta_{kl} = \sum_{\mu} h_k^{\mu} h_l^{\mu} / q\bar{h}^2, \quad (\text{A10})$$

where we use the notation \bar{h}^2 defined in (A7). Eq. (A9) leads to a simple estimate for the average fragmentation width of Eq. (20),

$$\bar{\sigma}^2 = (2bq^2/N)\bar{h}^2. \quad (\text{A11})$$

The bandwidth $2b$ is defined as an average value of $\sum_l \eta(|k - l|)$. It gives $(q\bar{h}^2)^{1/2} \approx 28$ MeV for the 2^+0 states. From Eq. (113) we find the rms fluctuation of the diagonal elements equal to $(2q\bar{h}^2/N)^{1/2} \approx 0.7$ MeV. The mean value of 0.5 MeV of the diagonal elements of Eq. (111) gives $qh \approx qh_k \approx 28$ MeV. The corresponding value of the radius, Eq. (33), is $a \approx 56$ MeV.

The statistical ensemble defined by the multipole factorization (A2) is different from the GOE and banded GOE, although the lowest correlator of matrix elements (A9) has the same form. Similar distributions were discussed in [7]; they appear also in the context of the generalized random matrix theory for unstable states [32] where the antihermitian part of the effective hamiltonian expressed in terms of the decay amplitudes has a separable form as in (A1). Assuming the Gaussian distribution of the multipoles Q_k^{μ} , the probability density for the diagonal matrix elements is given by the chi-square law for q degrees of freedom,

$$P_d(x_k) = [\Gamma(q/2)2^{q/2}]^{-1} x_k^{q/2-1} e^{-x_k/2}. \quad (\text{A12})$$

Here the dimensionless variable $x_k = \sqrt{N}|H_{kk}/\bar{h}_k|$ is introduced with the mean value $\bar{x}_k = q$ and the variance $(\Delta x_k)^2 = 2q$. As q increases, this distribution rapidly goes into the Gaussian form,

$$P_d(x) = [2\sqrt{\pi q}]^{-1} e^{-(x-q)^2/4q}. \quad (\text{A13})$$

As for the off-diagonal elements $\tilde{H}_{kl} \equiv (\bar{h}^2 \eta_{kl}/N)^{1/2} x_{kl}$, a similar consideration leads to the distribution function

$$P_{o-d}(x_{kl}) = [\sqrt{\pi}\Gamma(q/2)]^{-1/2} (|x_{kl}|)^{(q-1)/2} K_{(q-1)/2}(|x_{kl}|). \quad (\text{A14})$$

Here K stands for the modified Bessel function. The distribution (A16) agrees with the variance $(\tilde{H}_{kl})^2 = (1/N)q\bar{h}^2\eta_{kl}$ given by (A9). All functions $K_{\nu}(x)$ have an asymptotic behavior $\sim \exp(-x)/\sqrt{x}$. Therefore Eq. (A14) is practically similar to the empirical fit (49). At small x , Eq. (A14) gives a constant or, for $q = 1$, a logarithmic singularity. However it is difficult to check the small x behavior with sufficient accuracy.

References

- [1] A.J. Lichtenberg and M.A. Lieberman, Regular and Stochastic Motion (Springer, New York, 1983).
- [2] H.G. Schuster, Deterministic Chaos (VCH Verlagsgesellschaft, Weinheim, 1989).
- [3] F. Haake, Quantum Signatures of Chaos (Springer, New York, 1991).
- [4] P.V. Elyutin, Usp. Fiz. Nauk 155 (1988) 397 [Sov. Phys. Usp. 31 (1988) 597].

- [5] F.M. Izrailev, *Phys. Rep.* 196 (1990) 299.
- [6] *Statistical Theories of Spectra: Fluctuations*, ed. C.E. Porter (Academic Press, New York, 1965).
- [7] T.A. Brody, J. Flores, J.B. French, P.A. Mello, A. Pandey and S.S.M. Wong, *Rev. Mod. Phys.* 53 (1981) 385.
- [8] R. Haq, A. Pandey and O. Bohigas, *Phys. Rev. Lett.* 48 (1982) 1986.
- [9] H.-J. Stöckmann and J. Stein, *Phys. Rev. Lett.* 64 (1990) 2215.
- [10] H.-D. Gräf, H.L. Harney, H. Lengeler, C.H. Lewenkopf, C. Rangacharyulu, A. Richter, P. Schardt and H.A. Weidenmüller, *Phys. Rev. Lett.* 69 (1992) 1296.
- [11] C. Ellegaard, T. Guhr, K. Lindemann, H.Q. Lorensen, J. Nygard and M. Oxborrow, *Phys. Rev. Lett.* 75 (1995) 1546.
- [12] R. Arvieu, F. Brut, J. Carbonell and J. Touchard, *Phys. Rev.* A35 (1987) 2389.
- [13] B. Milek, W. Nörenberg and P. Rozmej, *Z. Phys.* A334 (1989) 233.
- [14] W.D. Heiss, R.G. Nazmitdinov and S. Radu, *Phys. Rev. Lett.* 72 (1994) 2351.
- [15] L.P. Gor'kov and G.M. Eliashberg, *Zh. Eksp. Teor. Fiz.* 48 (1965) 1407 [*Sov. Phys. JETP* 21 (1965) 940].
- [16] C.M. Marcus et al., *Phys. Rev. Lett.* 69 (1992) 506.
- [17] Y. Alhassid and A. Novoselsky, *Phys. Rev.* C45 (1992) 1677.
- [18] V. Lopac, S. Brant and V. Paar, *Z. Phys.* A337 (1990) 131.
- [19] H. Frisk and R. Arvieu, *J. Phys.* A22 (1989) 1765.
- [20] I.I. Gurevich, *Zh. Eksp. Teor. Phys.* 9 (1939) 1283.
- [21] A. Bohr and B. Mottelson, *Nuclear Structure*, Vol. 1 (Benjamin, New York, 1969).
- [22] M. Berry and M. Robnik, *J. Phys.* A17 (1984) 2413; M. Berry, *Proc. R. Soc.* A400 (1985) 229.
- [23] J.B. French et al. *Phys. Rev. Lett.* 54 (1985) 2313; 58 (1987) 2400.
- [24] G.E. Mitchell et al., *Phys. Rev. Lett.* 61 (1988) 1473; J.F. Shriner, Jr. et al., *Z. Phys.* A335 (1990) 393.
- [25] S. Raman et al., *Phys. Rev.* C43 (1991) 521.
- [26] S. Drożdż, S. Nishizaki, J. Speth and J. Wambach, *Phys. Rev.* C49 (1994) 867.
- [27] J.D. Garrett et al., *Future Directions with 4 π Gamma Detection Systems of the New Generation*, ed. J. Dudek and B. Haas (AIP, 1991) p. 345.
- [28] R.J. Blin-Stoyle, *Phys. Rev.* 120 (1960) 181.
- [29] O.P. Sushkov and V.V. Flambaum, *Pis'ma Zh. Eksp. Teor. Fiz.* 32 (1980) 377 [*JETP Lett.* 32 (1980) 353]; *Usp. Fiz. Nauk* 136 (1982) 3 [*Sov. Phys. Usp.* 25 (1982) 1].
- [30] V.G. Zelevinsky, *Nucl. Phys.* A553 (1993) 125c; A570 (1994) 411c.
- [31] N. Bohr, *Nature* 137 (1936) 344.
- [32] V.V. Sokolov and V.G. Zelevinsky, *Phys. Lett.* B202 (1988) 10; *Nucl. Phys.* A504 (1989) 562; *Ann. Phys.* 216 (1992) 323.
- [33] G. Montambaux et al., *Phys. Rev. Lett.* 70 (1993) 497.
- [34] N. Rosenzweig and C.E. Porter, *Phys. Rev.* 120 (1960) 1698.
- [35] V.V. Flambaum, A.A. Gribakina, G.F. Gribakin and M.G. Kozlov, *Phys. Rev.* A50 (1994) 267.
- [36] I.C. Percival, *J. Phys.* B6 (1973) L229.
- [37] E.J. Heller, *Phys. Rev. Lett.* 53 (1984) 1515.
- [38] R. Aurich and F. Steiner, *Physica* D48 (1991) 445.
- [39] W. Bauer, D. McGrew, V. Zelevinsky and P. Schuck, *Phys. Rev. Lett.* 72 (1994) 3771; *Nucl. Phys.* A583 (1995) 93.
- [40] V.G. Zelevinsky, *Nucl. Phys.* A555 (1993) 109.
- [41] G. Mantzouranis and H.C. Pauli, *Z. Phys.* A278 (1976) 373.
- [42] V.G. Zelevinsky, P.F. Bortignon and R.A. Broglia, preprint NBI-93-45.
- [43] V.V. Flambaum and O.P. Sushkov, *Nucl. Phys.* A412 (1984) 13.
- [44] B. Lauritzen, P.F. Bortignon, R.A. Broglia and V.G. Zelevinsky, *Phys. Rev. Lett.* 74 (1995) 5190.
- [45] J.J. Gaardhøje, *Annu. Rev. Nucl. Part. Sci.* 42 (1992) 483.
- [46] H.L. Harney, A. Richter and H.A. Weidenmüller, *Rev. Mod. Phys.* 58 (1986) 607.
- [47] V.G. Zelevinsky and P. von Brentano, *Nucl. Phys.* A529 (1991) 141.
- [48] J. Reiter and H.L. Harney, *Z. Phys.* A337 (1990) 121.
- [49] D.C. Meredith, S.E. Koonin and M.R. Zirnbauer, *Phys. Rev.* A37 (1988) 3499.
- [50] D.C. Meredith, *Phys. Rev.* E47 (1993) 2405.

- [51] B.A. Brown and G. Bertsch, *Phys. Lett.* 148B (1984) 5.
- [52] W.E. Ormand and R.A. Broglia, *Phys. Rev.* C46 (1992) 1710.
- [53] J.B. French and K.F. Ratcliff, *Phys. Rev.* C3 (1971) 94; K.F. Ratcliff, *Phys. Rev.* C3 (1971) 117.
- [54] F.S. Chang and J.B. French, *Phys. Lett.* 44B (1973) 131.
- [55] J.P. Draayer, J.B. French and S.S.M. Wong, *Ann. Phys.* 106 (1977) 472, 503.
- [56] J.J.M. Verbaarschot and P.J. Brussard, *Phys. Lett.* 87B (1979) 155.
- [57] V.V. Flambaum, *Phys. Scr.* T46 (1993) 198.
- [58] C.A. Bertulani and V.G. Zelevinsky, *Nucl. Phys.* A568 (1994) 931.
- [59] C.H. Lewenkopf and V.G. Zelevinsky, *Nucl. Phys.* A569 (1994) 183.
- [60] B. Lauritzen, T. Døssing and R.A. Broglia, *Nucl. Phys.* A457 (1986) 61.
- [61] S. Åberg, *Prog. Part. Nucl. Phys.* 28 (1992) 11.
- [62] T. Ericson, *Adv. Phys.* 9 (1960) 425.
- [63] S.T. Belyaev and V.G. Zelevinsky, *Yad. Fiz.* 2 (1965) 615 [*Sov. J. Nucl. Phys.* 2 (1966) 442].
- [64] V.V. Samoïlov and M.H. Urin, *Nucl. Phys.* A567 (1994) 237.
- [65] B.A. Brown and B.H. Wildenthal, *Annu. Rev. Nucl. Part. Sci.* 38 (1988) 29.
- [66] B.A. Brown et al., OXBASH code, MSUNSCL Report 524 (1988).
- [67] W.E. Ormand and B.A. Brown, *Nucl. Phys.* A491 (1989) 1.
- [68] E.P. Wigner, *Ann. Math.* 62 (1955) 548.
- [69] M. Horoi, B.A. Brown and V. Zelevinsky, *Phys. Rev.* C50 (1994) R2274.
- [70] M. Feingold, D.M. Leitner and M. Wilkinson, *Phys. Rev. Lett.* 66 (1991) 986.
- [71] J. Casati et al., *Phys. Rev. Lett.* 64 (1990) 1; M. Kuś, M. Lewenstein and F. Haake, *Phys. Rev.* A44 (1991) 2800.
- [72] Y.V. Fyodorov and A.D. Mirlin, *Phys. Rev. Lett.* 67 (1991) 2405.
- [73] J. Wambach, private communication.
- [74] D. Kusnezov, private communication.
- [75] J.B. French and S.S.M. Wong, *Phys. Lett.* B35 (1971) 5; K.K. Mon and J.B. French, *Ann. Phys.* 95 (1975) 90.
- [76] I.I. Gurevich and M.I. Pevsner, *Nucl. Phys.* 2 (1957) 575.
- [77] T. Prosen and M. Robnik, *J. Phys.* A26 (1993) 2371.
- [78] S. Mizutori and V.G. Zelevinsky, *Z. Phys.* A346 (1993) 1.
- [79] L. Molinari and V.V. Sokolov, *J. Phys.* A22 (1989) L999.
- [80] A. Altland and D. Fuchs, *Phys. Rev. Lett.* 74 (1995) 4269.
- [81] O. Bohigas, M.J. Giannoni and C. Schmit, *Phys. Rev. Lett.* 52 (1984) 1.
- [82] M.V. Berry, *Proc. R. Soc. London, Ser. A* 400 (1985) 229.
- [83] D. Wintgen and H. Marxer, *Phys. Rev. Lett.* 60 (1988) 971.
- [84] P. Arve, *Phys. Rev.* A44 (1991) 6920.
- [85] B. Mottelson, unpublished.
- [86] P. Pechukas, *Phys. Rev. Lett.* 51 (1983) 943.
- [87] D.W. Noid, M.L. Koszykowski, M. Tabor and R.A. Marcus, *J. Chem. Phys.* 72 (1980) 6169.
- [88] M. Wilkinson, *J. Phys.* A22 (1989) 2795.
- [89] A. Szafer and B.L. Altshuler, *Phys. Rev. Lett.* 70 (1993) 587.
- [90] P. Gaspard, S.A. Rice, H.J. Mikeska and K. Nakamura, *Phys. Rev.* A42 (1990) 4015.
- [91] J. Zakrzewski and D. Delande, *Phys. Rev.* E47 (1993) 1650.
- [92] F. von Oppen, *Phys. Rev. Lett.* 73 (1994) 798.
- [93] D. Kusnezov, B.A. Brown and V. Zelevinsky, in preparation.
- [94] N. Ullah and C.E. Porter, *Phys. Lett.* 6 (1963) 301; N. Ullah, *Int. Nucl. Phys. Conf.*, ed. R.L. Becker (Academic, New York, 1967) p. 812.
- [95] M.V. Berry, *J. Phys.* A10 (1977) 2083.
- [96] V. Zelevinsky, M. Horoi and B.A. Brown, *Phys. Lett.* B350 (1995) 141.
- [97] F.J. Yonezawa, *Non-Cryst. Solids* 35 & 36 (1980) 29.
- [98] J. Reichl, *Europhys. Lett.* 6 (1988) 669.
- [99] E.K. Warburton and B.A. Brown, *Phys. Rev.* C46 (1992) 923.
- [100] J.P. Elliott, *Proc. R. Soc.* A245 (1958) 128, 562.

- [101] M. Feingold, A. Gioletta, F.M. Izrailev and L. Molinari, to be published.
- [102] M. Horoi, V. Zelevinsky and B.A. Brown, *Phys. Rev. Lett.* 74 (1995) 5194.
- [103] L.D. Landau and E.M. Lifshitz, *Statistical Physics* (Pergamon Press, Oxford, 1958).
- [104] D.J. Morrissey, W. Benenson and W.A. Friedman, *Annu. Rev. Nucl. Part. Sci.* 44 (1994) 27.
- [105] V.V. Flambaum and O.K. Vorov, *Phys. Rev. Lett.* 70 (1993) 4051.
- [106] J. Ford and G.H. Lunsford, *Phys. Rev. A*1 (1970) 59.
- [107] M.V. Berry, *Les Houches XXXVI, Chaotic Behavior of Deterministic Systems*, eds. G. Iooss, R.H.G. Helleman and R. Stora (North Holland, Amsterdam, 1983); *Les Houches LII, Chaos and Quantum Physics*, eds. M.-J. Giannoni, A. Voros and J. Zinn-Justin (North Holland, Amsterdam, 1991).
- [108] M. Srednicki, *Phys. Rev. E*50 (1994) 888.
- [109] Ya.G. Sinai, *Usp. Mat. Nauk* 25 (1970) 137 [*Russ. Math. Surv.* 25 (1970) 137].
- [110] L. van Hove, *Physica* 21 (1955) 517; 23 (1957) 441; 25 (1959) 268.
- [111] H.-T. Elze and P.A. Carruthers, preprint CERN-TH.7431/94.
- [112] T. Døssing et al., *Phys. Rev. Lett.* 75 (1995) 1276.
- [113] K.T. Hecht, *Phys. Rev.* 139 (1995) B794; J.P. Elliott and J.A. Evans, *Phys. Lett.* 31B (1970) 157.
- [114] G. Racah, *Phys. Rev.* 76 (1949) 1352.

Note added in proof

We have recently found that the results for the spectral rigidity $\Delta(L)$ at the large L , presented and discussed in Section 3.4, are very sensitive to the details of the unfolding procedure. In particular, we have found a new unfolding procedure for which the results for $L < 150$ (Fig. 26) are not changed, but the results for high L (Fig. 27) become in better agreement with the GOE prediction. We plan to present details of this new analysis elsewhere.